



저작자표시-비영리-변경금지 2.0 대한민국

이용자는 아래의 조건을 따르는 경우에 한하여 자유롭게

- 이 저작물을 복제, 배포, 전송, 전시, 공연 및 방송할 수 있습니다.

다음과 같은 조건을 따라야 합니다:



저작자표시. 귀하는 원저작자를 표시하여야 합니다.



비영리. 귀하는 이 저작물을 영리 목적으로 이용할 수 없습니다.



변경금지. 귀하는 이 저작물을 개작, 변형 또는 가공할 수 없습니다.

- 귀하는, 이 저작물의 재이용이나 배포의 경우, 이 저작물에 적용된 이용허락조건을 명확하게 나타내어야 합니다.
- 저작권자로부터 별도의 허가를 받으면 이러한 조건들은 적용되지 않습니다.

저작권법에 따른 이용자의 권리는 위의 내용에 의하여 영향을 받지 않습니다.

이것은 [이용허락규약\(Legal Code\)](#)을 이해하기 쉽게 요약한 것입니다.

[Disclaimer](#)

이학박사 학위논문

Development of Theranostics for
Viral Disease and Cancer based
on Carbon Nanomaterials

탄소나노물질을 활용한 바이러스성 질병 및
암 치료 시스템 개발

2018 년 02 월

서울대학교 대학원
화학부 생유기화학 전공
김 성 찬

탄소나노물질을 활용한 바이러스성 질병 및

암 치료 시스템 개발

Development of Theranostics for Viral Disease and Cancer
based on Carbon Nanomaterials

지도 교수 민 달 희

이 논문을 이학박사 학위논문으로 제출함

2018 년 02 월

서울대학교 대학원

화학부 생유기화학전공

김 성 찬

김성찬의 이학박사 학위논문을 인준함

2017 년 12 월

위 원 장 _____ 홍종인 _____ (인)

부위원장 _____ 민달희 _____ (인)

위 원 _____ 박충모 _____ (인)

위 원 _____ 홍병희 _____ (인)

위 원 _____ 장홍제 _____ (인)

A Ph.D. Dissertation

Development of Theranostics for Viral Disease
and Cancer based on Carbon Nanomaterials

Supervisor : Professor Dal-Hee Min

Major : Bio-Organic Chemistry

By Seongchan Kim

Department of Chemistry

Graduate School of Seoul National University

2018. 02

Abstract

Development of Theranostics for Viral Disease and Cancer based on Carbon Nanomaterials

Seongchan Kim
Department of Chemistry
(Major: Bio–Organic Chemistry)
The Graduate School Seoul National University

Many recalcitrant diseases have its origin in the undesirable biological processes at molecular levels such as gene mutation, protein dysfunction, and viral infection. The field of nanomedicine approaches to apply the chemical/physical characteristics of nanomaterials for the diagnosis and treatment of viral diseases and cancer at the molecular level.

Among the various type of nanomaterials, herein, we focus on the carbon nanomaterials possessing unique physicochemical properties, giving rise to the great potential for the diagnosis and therapy of viral disease or cancer. Carbon nanomaterials exhibit several characteristics including high specific surface areas and sp^2/sp^3 hybridized carbon atoms. Therefore, they have simple relationships with

biomolecules through novel strategies of surface modification. This approach enables chemical or physical interaction with biomolecules facilitating improved biocompatibility and controlling their properties in biological systems. In this study, we reported four therapeutic systems including biological imaging, drug/gene delivery, and photodynamic therapy that are classified into two categories according to carbon allotrope; graphene oxide (GO) and carbon nanodot (CD).

First, we developed multifunctional DNAzyme (Dz) delivery system based on nano-sized graphene oxide (nGO) for simultaneous detection and knockdown of the target gene. The Dz/nGO complex system allowed convenient monitoring of hepatitis C virus (HCV) mRNA in living cells and silencing of the HCV gene expression by Dz-mediated catalytic cleavage concurrently.

Second, we design a dual action of the antibiotic drug and synthetic RNA based on the functionalized GO mediated co-delivery system and demonstrate its synergistic effect in vitro

and in liver cancer cell xenograft mouse model representing HCV infection. We find that our strategy successfully improves the therapeutic efficacy by suppressing the tumor growth through enhancing intracellular accumulation of antibiotic drug with one-tenth of conventional dosage and inhibiting replication of viral RNA at the molecular level through small interfering RNA (siRNA)-mediated sequence-specific messenger RNA (mRNA) cleavage.

Third, we describe a novel design of highly biocompatible, fluorescent, folic acid (FA) and PEG-functionalized CD as carriers for zinc phthalocyanine (ZnPc) PS to achieve simultaneous biological imaging and targeted photodynamic therapy. CD-PEG-FA/ZnPc exhibits excellent targeted delivery of the PS, leading to simultaneous imaging and significant targeted photodynamic therapy after irradiation in vitro and in vivo.

Finally, we report a strategy for therapeutic RNA interference (RNAi) based on the highly biocompatible and

fluorescent CD in which siRNAs are protected from RNase mediated degradation and have a longer half-life in vivo. Our strategy allows simultaneous bioimaging and efficient down-regulation of gene expression, showing high potential for gene therapy in vitro and in vivo.

We believe that these studies can provide a strong foundation for basic research in the field of nanomedicine and the long-term technical progress of nanotechnology into an effective clinical application.

Keyword : Carbon nanomaterials, theranostics, graphene oxide, carbon nanodot, bioimaging, drug delivery, gene delivery, photodynamic therapy,

Student Number : 2012-20267

Table of Contents

Abstract	1
Table of Contents	5
List of Figures	8
Chapter 1. Introduction.....	34
1.1. Nanotechnology and carbon nanomaterials	
1.2. Graphene oxide	
1.3. Carbon nanodot	
1.4. Description of Researches	
1.4.1. Deoxyribozyme-loaded nano-graphene oxide for simultaneous sensing and silencing of hepatitis C virus gene in liver cells	
1.4.2. Enhancing intracellular accumulation of antibiotic drug and combinational treatment of hepatitis C virus related hepatocellular carcinoma via functionalized graphene oxide in vitro and in vivo	
1.4.3. Highly biocompatible carbon nanodots for simultaneous bioimaging and targeted photodynamic therapy in vitro and in vivo	
1.4.4. Highly efficient gene silencing and bioimaging based on fluorescent carbon dot in vitro and in vivo	

Chapter 2. Therapeutic application of graphene oxide..... 48

2.1. Deoxyribozyme-loaded nano-graphene oxide for simultaneous sensing and silencing of hepatitis C virus gene in liver cells

2.1.1. Introduction

2.1.2. Materials and methods

2.1.3. Results and discussion

2.1.4. Conclusions

2.1.5. References

2.2. Enhancing intracellular accumulation of antibiotic drug and combinational treatment of hepatitis C virus related hepatocellular carcinoma via functionalized graphene oxide in vitro and in vivo

2.2.1. Introduction

2.2.2. Materials and methods

2.2.3. Results and discussion

2.2.4. Conclusions

2.2.5. References

Chapter 3. Therapeutic application of carbon nanodot..... 137

3.1. Highly biocompatible carbon nanodots for simultaneous bioimaging and targeted photodynamic therapy in vitro and in vivo

- 3.1.1. Introduction
- 3.1.2. Materials and methods
- 3.1.3. Results and discussion
- 3.1.4. Conclusions
- 3.1.5. References

3.2. Highly efficient gene silencing and bioimaging based on fluorescent carbon dot in vitro and in vivo

- 3.2.1. Introduction
- 3.2.2. Materials and methods
- 3.2.3. Results and discussion
- 3.2.4. Conclusions
- 3.2.5. References

Abstract in Korean 245

List of Figures

1. Introduction

Scheme 1.1. Strategy of detection and knockdown of target gene in mammalian cells based on Dz and nGO. nGO allows efficient intracellular delivery of Dz and serves as a fluorescence quencher..... **39**

Scheme 1.2. The strategy of GO mediated combinational therapy. a) NGO was the functionalized with PAA through simple synthetic process of epoxy–ring opening reaction and NGO–PAA was utilized as a co–carrier of high concentration of antibiotic drug possessing hydrophobic structure by $\pi - \pi$ interaction and hydrogen bonding interaction as well as siRNA having negatively charged phosphate backbone by electrostatic interaction. b) The DOX/siRNA loaded NGO–PAA enabled sequence–specific knockdown of target gene expression of HCV nonstructural gene 3 (NS3) as well as inhibition of replicating DNA via intercalation of antibiotics in human liver cells. **41**

Scheme 1.3. Schematic illustration of the preparation of

carbon nanodots (CD) from α -cyclodextrin and targeted photodynamic therapy with folic acid functionalized carbon nanodots loaded with zinc phthalocyanine (CD-PEG-FA/ZnPc)..... 42

Scheme 1.4. Strategy of CD-PEI mediated siRNA delivery and bioimaging. Complex of CD-PEI and siRNA is formed by electrostatic interaction between CD-PEI and siRNA. After cellular uptake of the siRNA/CD-PEI complex, siRNA is released from CD-PEI and the target gene knockdown is achieved by siRNA-RISC complex. Fluorescence of CD-PEI itself enabled fluorescent image based monitoring of cellular uptake of siRNA/CD-PEI complex and intracellular localization of CD-PEI in living cells..... 44

2. Therapeutic application of graphene oxide

Scheme 2.1. Strategy of detection and knockdown of target gene in mammalian cells based on Dz and nGO. nGO allows efficient intracellular delivery of Dz and serves as a fluorescence quencher..... 51

Figure 2.1. Characterization of nGO. a) AFM image and line profile of nGO showed width and height of nGO as approximately 0~300 nm and 0.97 nm, respectively. b) Raman spectrum of nGO showed D peak at 1354 cm^{-1} , G peak at 1594 cm^{-1} , respectively, giving $I_D/I_G = 0.90$. c) UV-vis spectrum of nGO. d) Elemental analysis to estimate the content of each element of nGO. e) Cell viability of Huh-7-rep cells incubated with different concentration of nGO as mean values from triplicate. **63**

Figure 2.2. Information of DNzyme and fluorescence quenching and recovery test. a) The structure of “10-23” DNzyme. N, any nucleotide. Y and R are pyrimidine and purine nucleotide. The black arrow indicates the cleavage site. b) The sequences of designed HCV DNzyme (Dz) and HCV scrambled-sequence DNzyme (scDz). c), d) Fluorescence of FAM was quenched when the FAM-Dz and FAM-scDz were adsorbed on the surface of nGO in a concentration dependent manner. **65**

Figure 2.3. The fluorescence intensity of FAM-Dz. a), b) The

quenched fluorescence of FAM-Dz by nGO was recovered increasingly upon the addition of the complementary mRNA in a concentration-dependent manner (0.02 – 1 μ M). c) The quenched fluorescence of FAM-Dz by nGO was stably maintained even after incubation with scRNA in the presence of serum for 1 h. d) The quenched fluorescence of FAM-Dz by nGO in the presence of serum was significantly recovered with addition of target mRNA but FAM-scDz/nGO did not show significant fluorescence increase with addition of mRNA.

..... 66

Figure 2.4. DNase protection assay. a) PAGE gel retardation assay for Dz incubated with different amounts of DNase (1.25, 2.5, 5.0, 10 units) in the presence or in the absence of nGO. Without nGO, Dz was completely degraded by DNase I whereas the Dz adsorbed to nGO was resistant to the DNase I-mediated cleavage. b) Fluorescence spectra of FAM-Dz after treated with DNase I, with or without nGO. Degradation of Dz by DNase I was inhibited by nGO, showing much less decrease of the fluorescence intensity upon treatment of DNase I in the presence of nGO compared to that of the Dz

treated with DNase I in the absence of nGO, followed by addition of nGO..... 69

Figure 2.5. Fluorescence images of Huh-7-rep cells that were treated with FAM-Dz/nGO and FAM-scDz/nGO (1.0 μ M) for 12 h. Fluorescence of FAM was turned on only when the Dz complementary to target HCV NS3 RNA was used. Blue: nucleus stained with Hoechst 33342, green: FAM. Scale bar is 100 μ m..... 71

Figure 2.6. Fluorescence recovery in Huh-7-rep cell was observed over time after treatment with 1 μ M of FAM-Dz/nGO. The fluorescence of FAM-Dz gradually increased as time went by (0 – 12 h) in cytoplasm. Blue: nucleus stained with Hoechst 33342, Green: FAM..... 71

Figure 2.7. Expression levels of NS3 and GAPDH of Huh-7-rep cells were measured after incubation with Dz/nGO and scDz/nGO for 48 h. Gene expression levels were evaluated by a) semi-quantitative RT-PCR and b) Western blotting. c) and d) Normalized band intensities in a) and b) obtained by using Image J software. 74

Scheme 2.2. The strategy of GO mediated combinational therapy. a) NGO was the functionalized with PAA through simple synthetic process of epoxy–ring opening reaction and NGO–PAA was utilized as a co–carrier of high concentration of antibiotic drug possessing hydrophobic structure by $\pi - \pi$ interaction and hydrogen bonding interaction as well as siRNA having negatively charged phosphate backbone by electrostatic interaction. b) The DOX/siRNA loaded NGO–PAA enabled sequence–specific knockdown of target gene expression of HCV nonstructural gene 3 (NS3) as well as inhibition of replicating DNA via intercalation of antibiotics in human liver cells. 84

Figure 2.8. AFM study of morphological image and line–profile for thickness (inset) of a) NGO and b) NGO–PAA. The increase of width and height in NGO–PAA showed as approximately ~ 200 nm and 8.35 nm, respectively. c) UV–vis–NIR absorption spectrum showed red–shift of absorbance at $\pi - \pi$ transition of aromatic carbon bond of NGO–PAA by partial restoration of sp^2 carbon structure domain. d) FT–IR

spectrum showed the change of transmittance in NGO-PAA by reduction and functionalization e) Raman spectrum of NGO-PAA indicated the increase of relative I_D/I_G ratio from 0.912 to 0.954..... **97**

Figure 2.9. Size distribution and zeta potential value of NGO derivatives. a-d) The size was measured by dynamic light scattering method in buffered solution (pH 7.4). The size distribution was gradually increased according to modify the surface functionality and to form the complex condensed with DOX and siRNA. e) The surface charge of NGO derivatives was changed after surface modification with PAA and subsequent loading DOX and siRNA. **98**

Figure 2.10. Poly acrylamide gel electrophoresis analysis for siRNA/NGO-PAA complexation. a) The band intensity of siRNA decrease in accordance with amount of NGO-PAA. b) Heparin polyanion competitive assay for siRNA release from NGO-PAA. c) siRNA protection ability of NGO-PAA by nuclease-mediated degradation in the presence of RNase. **100**

Figure 2.11. Dox loading and release profile. a) UV-vis-NIR

absorption spectrum of DOX, NGO–PAA, and DOX/NGO–PAA. The characteristic peak of DOX at 490 nm revealed in DOX and DOX/NGO–PAA. b) Real–time monitoring of fluorescence of DOX ($\lambda_{em}=590$ nm) corresponding to cumulative release at various conditions. The released DOX from the NGO–PAA recovered fluorescence gradually in acidic condition and reductive condition. 104

Figure 2.12. Fluorescence quenching test. The fluorescence of DOX at 590 nm ($\lambda_{ex}=547$ nm) was quenched by NGO–PAA through $\pi - \pi$ interaction. 106

Figure 2.13. UV–vis–NIR spectrum for stability test of NGO–PAA in a buffered solution with serum over time..... 108

Figure 2.14. The biocompatibility of NGO–PAA was confirmed by using CCK–8 cell proliferation assay kit. NGO–PAA shows high cell viability over 90% after incubation with Huh7–rep cells for 12 h. The experiment was carried out in three times. 109

Figure 2.15. Intrecellular uptake study of DOX. a)

Fluorescence image of Huh7–rep cells treated with DOX and DOX/NGO–PAA over time. Blue fluorescence signals from nucleus stained with Hoechst 33342 were observed at 461 nm ($\lambda_{ex}=365$ nm) and red fluorescence of DOX appeared at 590 nm ($\lambda_{ex}=547$ nm) in the cells. Red fluorescence of DOX were strongly intensified in nucleus and whole celled treated with DOX/NGA–PAA compared to that treated with DOX itself. Scale bar is 50 μ m. b) Cell population histogram correlated with fluorescence intensity of DOX uptaken to the cells over time by flow cytometric analysis. c) Bar–graph with relative fluorescence intensity corresponding to histogram of each cell treated with DOX and DOX/NGO–PAA. 112

Figure 2.16. Intracellular uptake study of DOX and siRNA. Bright field and fluorescence images of Huh7–rep cells treated with siRNA, DOX, and those complex form with NGO–PAA. Blue fluorescence signals from nucleus stained with Hoechst 33342 were observed at 461 nm ($\lambda_{ex}=365$ nm) in whole cells but green fluorescence signal from siRNA at 497 nm ($\lambda_{ex}=520$ nm) and red fluorescence of DOX at 547 nm ($\lambda_{ex}=590$ nm) was strongly appeared in NGO–PAA mediated

siRNA, DOX-treated cells. Scale bar is 50 μm 115

Figure 2.17. Quantitative evaluation of therapeutic efficacy of NGO-PAA based siRNA and DOX delivery in Huh7-rep cell line. a) Band images at mRNA expression level of HCV NS3 and β -actin by RT-PCR and the bar-graph of HCV NS3 normalized to β -actin by using Image J software. b) Relative cell viabilities corresponding to synergistic therapeutic efficacy. NGO-PAA mediated siRNA/DOX combination delivery shows remarkably enhanced therapeutic efficiency. c) Relative viabilities of Huh7-rep cells treated with various concentration of DOX measured by using CCK-8 cell viability assay kit. Inset table shows IC_{50} value (μM) of DOX for therapeutic efficiency treated with DOX itself (0.97), DOX/NGO-PAA (0.61) and DOX/siRNA/NGO-PAA (0.26), respectively..... 119

Figure 2.18. Anti-HCV therapeutic efficacy of NGO-PAA based siRNA and DOX co-delivery in a mouse model producing HCV replication. a) Immunostaining for GAPDH and HCV NS3 proteins in the xenograft at 6 weeks post Huh7-rep

implanting. Blue: Nucleus, Red: GAPDH, Green: HCV NS3. Scale bar is 100 μm . b) Relative tumor volumes measured over 16 days after the Huh7–rep tumor–bearing mice were treated with PBS, NGO–PAA, free siRNA, free DOX, DOX/NGO–PAA, and DOX/siRNA/NGO–PAA by intratumoral injection three times (0, 5, and 10 days). P–value was calculated by Student’s t–test, * for $p < 0.05$, $n = 3$ **123**

Figure 2.19. Immunostaining for HCV NS3 proteins in the xenograft treated with NGO–PAA, siRNA, DOX, DOX/siRNA/NGO–PAA (Complex), and PBS at 6 weeks post Huh7–rep implanting Blue: Nucleus, Green: HCV NS3. Scale bar is 100 μm **125**

Figure 2.20. Hematoxylin and eosin (H&E) stained images of major organs excised from the mouse after treatment of PBS and DOX/siRNA/NGO–PAA complex. No notable systemic toxicity from major organs in case of DOX/siRNA/NGO–PAA was observed compared to those of PBS as a control at 16 days post treatment... .. **125**

3. Therapeutic application of carbon nanodot

Scheme 3.1. Schematic illustration of the preparation of carbon nanodots (CD) from α -cyclodextrin and targeted photodynamic therapy with folic acid functionalized carbon nanodots loaded with zinc phthalocyanine (CD-PEG-FA/ZnPc)..... 141

Figure 3.1. Characterization of CDs. a) UV-vis absorbance spectra of CD, CD-PEG, and CD-PEG-FA. Inset shows the CD-PEG-FA suspension (left) under room light and (right) UV illumination at 365 nm. b) Three-dimensional fluorescence spectra of CD-PEG-FA under varying excitation wavelengths from 300 to 600 nm with 10-nm increments. c) FT-IR spectra of CD, CD-PEG, and CD-PEG-FA. d) TEM images of CD-PEG-FA with a corresponding size distribution histogram. e) Representative height-mode AFM topography image of CD-PEG-FA with a line scan profile in the inset..... 153

Figure 3.2. Fluorescence spectra of free FA, CD-PEG, and CD-PEG-FA. The QY increase after the FA conjugation is

resulted from the successful surface passivation of CD with a small molecule like FA. 154

Figure 3.3. Optical characteristic of CDs. a) Time-resolved PL signal measured by time-correlated single photon counting (TCSPC) and b) exciton lifetime of CD, CD-PEG and CD-PEG-FA. 155

Figure 3.4. Photoluminescence spectra of a) CD, b) CD-PEG, c) CD-PEG-FA, and d) CD-PEG-FA/ZnPc. Inset images represent the optical images of the respective CDs under (left) ambient light and (right) UV light at 365 nm. 156

Figure 3.5. Deconvoluted high-resolution XPS C 1s peak of a) CD, b) CD-PEG, and c) CD-PEG-FA. CD has sp^3 carbon (284.94 eV), sp^2 carbon (285.40 eV), C-O groups (286.8 eV), C=O groups (288.2 eV) and COOH groups (289.08 eV), indicating that CDs are rich in hydroxyl, carbonyl and carboxylic acid groups on the surfaces. After passivation with amine-terminated PEG, the intensity of C-O peak is increased at 286.28 eV due to C-O groups in PEG. Further, the amount of carbonyl group is decreased from 6.06% to

0.50% with a concomitant appearance of the new peak of C–N group is observed at 287.43 eV, which indicates carbonyl group in CD and amine group in PEG is successfully reacted to amide groups. In addition, the intensities of C–N, C=O and COOH groups are increased in CD–PEG–FA, which also confirms the formation of more amide groups between the free amine–terminated PEG and FA after passivation with FA.
 158

Figure 3.6. Height–mode AFM images of a) CD, b) CD–PEG and c) CD–PEG–FA with corresponding line scan profiles. The scale bar is 1 μm 159

Figure 3.7. ZnPc loading study. a) UV–vis absorbance spectra of (red) CD–PEG–FA, (black) CD–PEG–FA/ZnPc and (blue) free ZnPc. b) Fluorescence spectra of (solid line) free ZnPc, (dotted line) CD–PEG–FA/ZnPc with an excitation wavelength of 650 nm..... 161

Figure 3.8. Size distribution of CDs. a, b) AFM and c, d) Dynamic light scattering (DLS) of a, c) CD–PEG–FA and b, d) CD–PEG–FA/ZnPc. 162

Figure 3.9. CCK-8 based cell viability assays with HeLa cells with different concentration of CD, CD-PEG and CD-PEG-FA..... 165

Figure 3.10. CCK-8 based cell viability assays with HeLa cells with different concentration of CD-PEG-FA/ZnPc.. 165

Figure 3.11. Intracellular uptake study. a-d) Bright-field and fluorescence images of HeLa cells treated with CD derivatives (50 mg/ml) for 12 h. a) CD-PEG, b) CD-PEG-FA, c) CD-PEG-FA/ZnPc and d) CD-PEG-FA/ZnPc pretreated with folic acid. Fluorescence signals of (blue) CDs and (red) ZnPc were observed at 461 nm ($\lambda_{ex} = 358$ nm) and 665 nm ($\lambda_{ex} = 647$ nm), respectively. Scale bar is 20 μ m..... 166

Figure 3.12. Bright field and fluorescence images of HeLa cells treated with CD-PEG-FA/ZnPc (50 μ g/ml) for 12 h. Fluorescence signals of (blue) CDs and (red) ZnPc were observed by using Deltavision high-resolution microscopy. Scale bar is 20 μ m..... 167

Figure 3.13. Fluorescence of CD-PEG/ZnPc was measured in

folate receptor (FR) overexpressed cell (MDA-MB-231 cells) and FR deficient cell (A549 cells) by In-cell analyzer 2000 after 12 h incubation. No significant fluorescence of CD and ZnPc were observed in A549 cells and CD-PEG/ZnPc treated MDA-MB-231 cells. Scale bar is 20 μm168

Figure 3.14. Photodynamic study in vitro. a-d) (top panel) Bright-field and fluorescence images of HeLa cells treated with CD derivatives (50 mg/ml) for 12 h, followed by irradiation for 10 min with a 660 nm laser (30 mW/cm^2), and (bottom panels) live and dead cells colored green and red, respectively, by live/dead assay. a) CD-PEG, b) CD-PEG-FA, c) CD-PEG-FA/ZnPc, and d) CD-PEG-FA/ZnPc with pretreatment of excess free FA. Scale bar is 100 μm . e, f) Quantitative evaluation of photodynamic effect. e) Singlet oxygen detection test using a singlet oxygen sensor green (SOSG) reagent. Time-dependent fluorescent intensity ($\lambda_{\text{ex}}/\lambda_{\text{em}} = 504/530 \text{ nm}$) with irradiation by using a 660 nm laser (30 mW/cm^2). Concentrations of ZnPc and SOSG used are 3.8 and 2.5 μM , respectively. Note that the addition of cell lysate (1 mL) in CD-PEG-FA/ZnPc did not change the effective

concentrations of ZnPc and SOSG. f) Cell viability assay depending on the concentration of ZnPc loaded CD-PEG-FA and ZnPc with and without irradiation for 10 min. All experiments were carried out in triplicate; the error bars represent the standard deviation.....172

Figure 3.15. Fluorescence image of HeLa cells which were treated with CD-PEG-FA/ZnPc (50 µg/ml) for 12 h followed by irradiation with a 660-nm laser (30 mW/cm²) for 10 min. Live and dead cells were colored green and red, respectively by live/dead assay. Scale bar is 100 µm.174

Figure 3.16. Bioimaging and photodynamic study in vivo. a) Fluorescence of ZnPc (excited at 660 nm) in tumor was imaged after 12 h injection of CD-PEG-FA/ZnPc, CD-PEG/ZnPc, and CD-PEG-FA (0.5 mg of ZnPc/kg mouse). b) CD-PEG-FA/ZnPc suspensions were injected into tail veins of tumor-bearing mice and the fluorescent signals were obtained at various time points (1, 2, 6, 12, 24, and 48 h). c) Ex vivo fluorescence images of major organs of mice. The fluorescent signals corresponding to ZnPc (excited at 660 nm) from major organs, tumor, and skin were obtained after

12 h of i.v. injection of CD-PEG-FA/ZnPc and CD-PEG/ZnPc into tumor-bearing mice. FA-conjugated CD delivered and released ZnPc to tumor effectively, in contrast with the CD lacking FA. d,e) Relative tumor volumes measured over time after the tumor-bearing mice were treated with various CD derivatives. Tumor-bearing mice were separated into 6 groups: (i) PBS control; (ii) CD-PEG-FA without irradiation; (iii) CD-PEG-FA with irradiation; (iv) CD-PEG/ZnPc without irradiation; (v) CD-PEG/ZnPc with irradiation; (vi) CD-PEG-FA/ZnPc without irradiation; (vii) CD-PEG-FA/ZnPc with irradiation (n=4 for each group). Irradiation was performed using a 660-nm laser at 0.3 W/cm². Tumor volumes were measured over 10 days. It is notable that no significant increase in tumor volume was observed for 8 days in mice treated with CD-PEG-FA/ZnPc with irradiation. P-values were calculated by Student's t-test: * for p < 0.05, n=4.....177

Scheme 3.2. Strategy of CD-PEI mediated siRNA delivery and bioimaging. Complex of CD-PEI and siRNA is formed by electrostatic interaction between CD-PEI and siRNA. After

cellular uptake of the siRNA/CD-PEI complex, siRNA is released from CD-PEI and the target gene knockdown is achieved by siRNA-RISC complex. Fluorescence of CD-PEI itself enabled fluorescent image based monitoring of cellular uptake of siRNA/CD-PEI complex and intracellular localization of CD-PEI in living cells..... 189

Figure 3.17. Characterization of CD-PEI. a) UV-vis absorption spectrum of CD-PEI. Inset shows a photo of the CD-PEI suspension (left) under ambient room light and (right) UV illumination at 360 nm. b) Three-dimensional fluorescence spectra of CD-PEI under varying excitation wavelength from 300 to 800 nm with 10 nm increments. c) FT-IR spectrum of CD-PEI. d) Deconvoluted high-resolution XPS C 1s peak of CD-PEI with the survey XPS spectra of CD-PEI in the inset. e) TEM image of CD-PEI. Inset shows a representative image of single CD-PEI with lattice spacing of 0.21 nm. f) An AFM topography image of CD-PEI obtained under constant height contact scanning mode is shown with a line scan profile in the inset..... 204

Figure 3.18. Characterization of CD-PEI. a) Photoluminescence spectra of CD-PEI. The excitation wavelength ranged from 320 to 410 nm with 10 nm increments as indicated. b) Time-resolved PL signal measured by time-correlated single photon counting (TCSPC) and exciton life time of CD-PEI. c) The size distribution histogram of CD-PEI d) XRD pattern of CD-PEI. 206

Figure 3.19. PAGE analysis to investigate siRNA loading to CD-PEI. a) Mixed solutions of CD-PEI with siGFP and Cy5-siGFP at various concentrations were prepared and loaded for PAGE. Gel image suggested that maximum siRNA loading could be achieved using ~150 and ~100 pmol of siGFP and Cy5-siGFP, respectively, towards 1 μ g of CD-PEI. b) PAGE analysis was performed after heparin was added to mixtures of CD-PEI/siRNA. Polyanion competition assay revealed that the loaded siRNA to CD-PEI could be released from CD-PEI upon treatment of polyanionic heparin. c) Gel image showed that RNase-mediated siRNA degradation was inhibited in the presence of CD-PEI. In contrast, free siRNA without CD-PEI

was completely degraded upon addition of RNase.....**211**

Figure 3.20. PAGE analysis was carried out to measure a) loading capacity of siVEGF to CD-PEI and b) RNase protection assay. Similar to siGFP, siVEGF was also protected from RNase mediated degradation in the presence of CD-PEI. c) DLS analysis for size distribution of siRNA/CD-PEI complex in pH 7.0 buffered condition.....**212**

Figure 3.21. Viability of GFP-HeLa and MDA-MB-231 cells were measured after treatment of a) CD-PEI and b) free PEI at different concentrations for 12 h by CCK-8 assay.....**214**

Figure 3.22. Optical properties of Cy5-siRNA/CD-PEI. a,b) The Quantum yield of CD-PEI (18.8%) and Cy5-siRNA/CD-PEI (19.5%) were measured at 360 nm excitation wavelength. a) Absorbance corresponding to CD-PEI concentration with and without Cy5-siRNA. b) Area of fluorescence versus absorbance value for measuring the quantum yield of CD-PEI. c) Three-dimension fluorescence spectra of Cy5-siRNA/CD-PEI under varying excitation wavelength from 300 to 700 nm with 10-nm increments. Inset spectra is

fluorescence spectra of Cy5-siRNA/CD-PEI under varying excitation wavelength from 600 to 700 nm with 10-nm increments. d) Absorption spectrum of Cy5-siRNA/CD-PEI. Inset image show the PL of CD-PEI with UV light. e) Photoluminescence spectra of Cy5-siRNA/CD-PEI. The excitation wavelength ranged from 320 to 410 nm with 10 nm increments as indicated. 217

Figure 3.23. Intracellular uptake study. a) Fluorescent images of GFP-HeLa cells treated with Cy5-siGFP/CD-PEI (blue: CD-PEI, green: GFP, and red: Cy5-siGFP). b) TEM images of GFP-HeLa cells treated with CD-PEI showed the presence of the internalized CD-PEI in cytoplasm. c), d) Fluorescence signals of Cy5-siGFP and CD-PEI in the cytoplasm of GFP-HeLa cells treated with Cy5-siGFP/CD-PEI. Fluorescence intensities were measured along with line scan profile in living cells. After 12 h incubation of the GFP-HeLa cells treated with siGFP/CD-PEI, fluorescence corresponding to Cy5-siGFP was hardly co-localized with blue fluorescence corresponding to CD-PEI d) whereas Cy5-siGFP fluorescence was mostly overlapped with CD-PEI

fluorescence at 2 h post-incubation c), implying that Cy5-siGFP become released from its delivery carrier, CD-PEI, overtime in cytoplasm..... **218**

Figure 3.24. Fluorescent images of GFP-HeLa cells treated with CD-PEI (blue: CD-PEI, green: GFP, and red: Cy5-siGFP)..... **219**

Figure 3.25. TEM image and DLS data of CD-PEI in buffered solution a), c) pH 7.0 and b), d) pH 5.0..... **219**

Figure 3.26. Fluorescent images of GFP-HeLa cells treated with Cy5-siRNA/CD-PEI complex were obtained at different time points after incubation. a) Each fluorescence signal of Cy5-siRNA and CD-PEI was gradually separated from each other over time (0 - 12 h) in cytoplasm. (blue: CD-PEI, red: Cy5-siRNA) b) Left image was obtained under GFP fluorescence channel and right image is the corresponding bright field image. Images in b) show the almost completely down-regulated GFP expression due to the siRNA-mediated target gene suppression..... **221**

Figure 3.27. Down-regulation of GFP gene expression by using siGFP/CD-PEI complex. a) Fluorescence microscope images of GFP-HeLa cells treated with siGFP/CD-PEI were obtained at 12 h post-incubation. b) Mean fluorescence of GFP expression in the GFP-HeLa cells were quantitatively measured by flow cytometry. M1 and M2 indicate two populations of cells expressing GFP at different degree due to significant suppression of GFP expression (M1) and little or no down-regulation of GFP expression (M2). c) Relative GFP fluorescence level and d) relative GFP gene down-regulation observed from flow cytometry measurement in b) were presented in bar graphs. Scale bar is 100 μ m. P-values were calculated by Student's t-test: ** for $p < 0.01$, $n = 3$ **224**

Figure 3.28. Images of control GFP-HeLa cells treated with Lipo only and PEI only. Without siGFP, only Lipo or PEI cannot silence GFP gene expression..... **225**

Figure 3.29. Fluorescence images of MDA-MB-231 cells treated with CD-PEI (50 μ g/mL). a) Blue fluorescence of CD-PEI was observed in perinuclear region of MDA-MB-

231 cells. b) Bright field image was merged with fluorescent image of CD-PEI in the cells..... 228

Figure 3.30. Expression level of VEGF and GAPDH of MDA-MB-231 cells. Gene expression levels were evaluated by semi-quantitative RT-PCR and gel electrophoresis. P-values were calculated by Student's t-test: ** for $p < 0.01$ ($n = 3$). 229

Figure 3.31. Band images for assessment of the immunostimulatory properties of CD-PEI in GFP-HeLa cells. No induced production of TLR3 and activation of $INF-\beta$ was observed in CD-PEI and siRNA/CD-PEI treated cells. Poly I:C was treated as positive control (P/C)..... 231

Figure 3.32 GFP knockdown and tumor growth inhibition in vivo. a) Green fluorescence was monitored from tumors in GFP-HeLa xenograft bearing mouse. Significant decrease of GFP fluorescence was observed in the siGFP/CD-PEI treated tumor compared to those treated with siGFP/PEI and free siGFP. b) Red fluorescence originated from cy5-siGFP was observed from tumors. The Cy5 fluorescence from free Cy5-

siGFP treated tumor was totally disappeared because of degradation and removal of Cy5-siGFP whereas the corresponding signal from the Cy5-siGFP/CD-PEI treated tumor was notably high. c) Relative tumor volumes measured over 14 days after the MDA-MB-231 tumor-bearing mouse were treated with PBS, CD-PEI, free siVEGF, and siVEGF/CD-PEI intravenously three times (0, 5, and 10 days). P-values were calculated by student's t-test, ** for $p < 0.01$, $n = 4$ **235**

Figure 3.33. Bioimaging in vivo. a) Bright field and fluorescence image ($\lambda_{ex} = 490$ nm) of HeLa tumor-bearing xenograft mice were obtained after 24 h of IV injection of CD-PEI (left) and PBS (right). b) Ex vivo fluorescence images of major organs of mice. The fluorescent signals corresponding to CD-PEI ($\lambda_{ex} = 490$ nm) from major organs, tumor, and skin were observed after 24 h of IV injection of CD-PEI (left). No fluorescence signals were observed in organs and tumor of PBS introduced mice (right). **236**

Chapter 1. *Introduction*

1.1. Nanotechnology and carbon nanomaterials

Nanotechnology stands for the “intentional design, characterization, production, and applications of materials, structures, devices, and systems by controlling their size and shape in the nanoscale range (1–100 nm).”¹ Since nanomaterials have similar scale compared to various biomolecules and biological systems, the nanotechnology has a great potential for medical applications, which generate an area of nanomedicine.

Over the past several decades, various strategies have been developed to synthesize nanomaterials and to control their unique, size–dependent properties. Contrary to macro materials, the nanomaterials possess not only a high ratio of surface area to volume but tunable optical and biological properties with different sizes, shapes, structures and surface modifications. With an understanding of these fundamental properties, the use of nanomaterials in medical applications can be successfully optimized. Nanomaterials are currently

being engineered as vehicles of the therapeutic agent or a platform of diagnostics through the comprehension of nanomaterials–biomolecule interaction and nano–bio interface system. And some of the materials are in the proof–of–concept stage in research laboratories for clinical application and have shown the possibility for the theranostics in humans by authorization of Food and Drug Administration (FDA).^{2,3}

Among the various types of nanomaterials, carbon nanomaterials that are carbon nanodot, fullerenes (0D), carbon nanotube (1D), graphene (2D), and mesoporous carbon nanomaterials (3D), have been extensively investigated for cancer diagnostics and treatment due to their unique physicochemical properties. Carbon nanomaterials exhibit several characteristics including high specific surface areas and sp^2/sp^3 hybridized carbon atoms. Therefore, they have simple relationships with biomolecules through novel strategies of surface modification. This approach enables chemical or physical interaction with biomolecules facilitating improved biocompatibility and controlling their properties in biological systems.

1.2. Graphene oxide

Graphene is a 2D monolayer sheet possessing a sp^2 -hybridized carbon and a honeycomb lattice structure. Due to the structural features, it exhibits remarkable physicochemical properties such as significant thermal and electrical conductivity and specific optical characteristics.⁴

Graphene oxide (GO), an oxidized form of graphene, possess the functional groups (hydroxyl, carboxylic, epoxy), which facilitate its surface modification. High specific surface area of GO offers a great capability to immobilize various types of biomolecules such as DNA, protein and drugs through chemical and physical interactions; major binding sources are $\pi-\pi$ stacking and hydrogen bonding. An important feature of GO via electron/energy transfer between the GO and chemical species or structures enable the development of sensing platform based on fluorescence probe. Exploiting these unique characteristics, GO have been widely used for the development of cancer imaging probes, drug/gene delivery systems, hyperthermia, photodynamic therapy for cancer theranostics.⁵⁻¹⁰

1.3. Carbon nanodot

Carbon nanodot (CD), a new class of carbon based nanomaterial, has received significant attention due to its low cytotoxicity, simple preparation, high chemical stability and unique optical properties like semiconducting quantum dots.^{11–14} CD are generally composed of a mixed phase of sp^2 - and sp^3 -hybridized carbon nanostructures in the form of conjugated carbon clusters functionalized with oxygen-bearing functional groups.¹⁵ Aside the strong fluorescence of CDs, their unique chemical structure allows the integration of active therapeutic molecules into the sp^2 carbon frame, and their surface functional groups enable further conjugation with other molecules such as biological affinity ligands. Taking advantages of their excellent optical and chemical properties, CDs have been employed in a number of biological applications, including plasmid DNA/drug delivery, bioimaging, biosensing, and photo-induced cancer therapy.^{16–20}

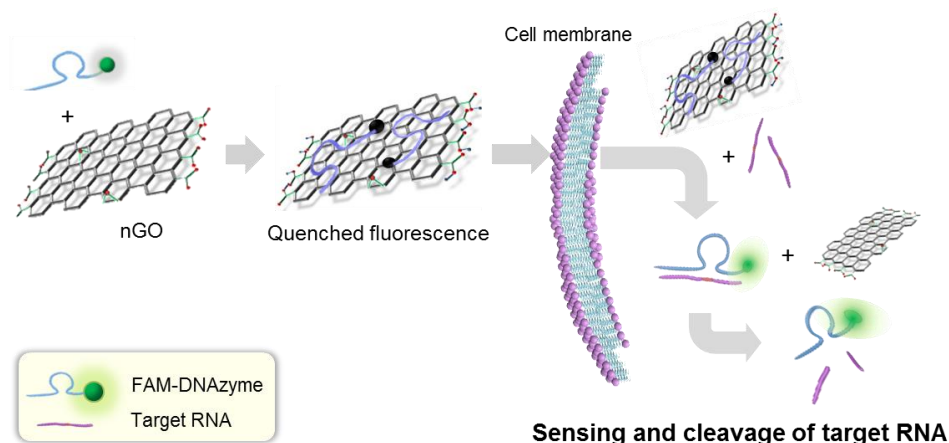
Although the carbon nanomaterials including GO and CD provide high potentials for therapeutic application, a challenge remains for in vivo therapeutic system. Here we report

improved therapeutic systems including biological imaging, drug/gene delivery, and photodynamic therapy of viral disease and cancer.

1.4. Description of researches

1.4.1. Deoxyribozyme-loaded nano-graphene oxide for simultaneous sensing and silencing of hepatitis C virus gene in liver cells

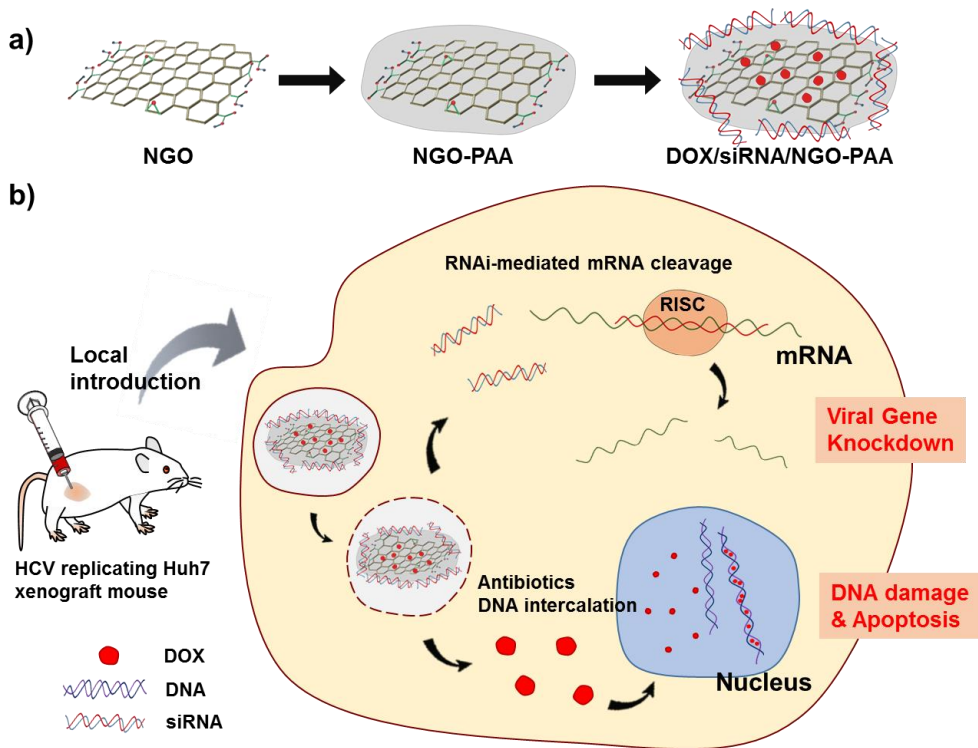
We developed multifunctional DNAzyme (Dz) delivery system based on nano-sized graphene oxide (nGO) for simultaneous detection and knockdown of the target gene. The Dz/nGO complex allowed convenient monitoring of hepatitis C virus (HCV) mRNA in living cells and silencing of the HCV gene expression by Dz-mediated catalytic cleavage concurrently.



Scheme 1.1. Strategy of detection and knockdown of target gene in mammalian cells based on Dz and nGO. nGO allows efficient intracellular delivery of Dz and serves as a fluorescence quencher.

1.4.2. Enhancing intracellular accumulation of antibiotic drug and combinational treatment of hepatitis C virus related hepatocellular carcinoma via functionalized graphene oxide in vitro and in vivo

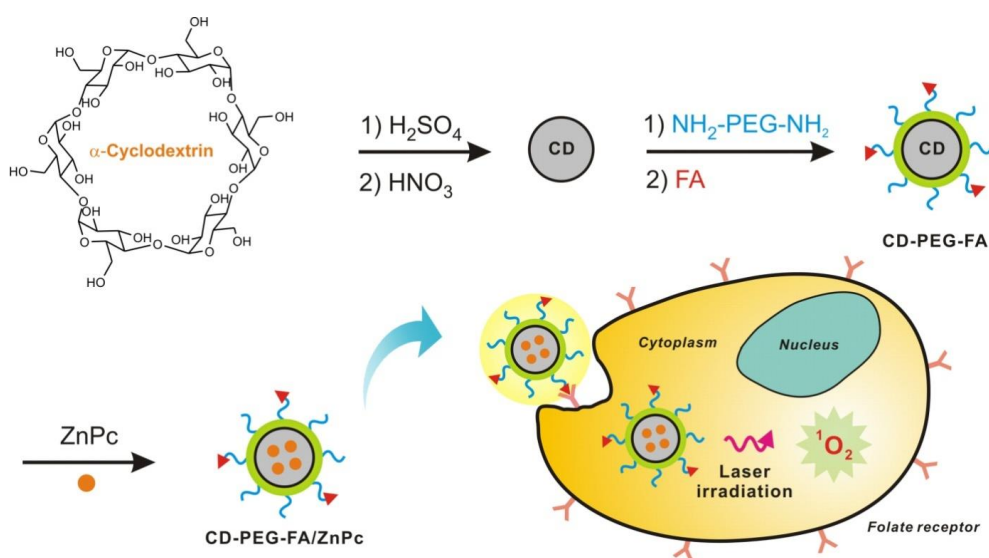
We design a dual action of the antibiotic drug and synthetic RNA based on the functionalized graphene oxide (GO) mediated co-delivery system and demonstrate its synergistic effect in vitro and in liver cancer cell xenograft mouse model representing HCV infection. We find that our strategy successfully improves the therapeutic efficacy by suppressing the tumor growth through enhancing intracellular accumulation of antibiotic drug with one-tenth of conventional dosage and inhibiting replication of viral RNA at the molecular level through small interfering RNA (siRNA)-mediated sequence-specific messenger RNA (mRNA) cleavage.



Scheme 1.2. The strategy of GO mediated combinational therapy. a) NGO was the functionalized with PAA through simple synthetic process of epoxy–ring opening reaction and NGO–PAA was utilized as a co–carrier of high concentration of antibiotic drug possessing hydrophobic structure by $\pi - \pi$ interaction and hydrogen bonding interaction as well as siRNA having negatively charged phosphate backbone by electrostatic interaction. b) The DOX/siRNA loaded NGO–PAA enabled sequence–specific knockdown of target gene expression of HCV nonstructural gene 3 (NS3) as well as inhibition of replicating DNA via intercalation of antibiotics in human liver cells.

1.4.3. Highly biocompatible carbon nanodots for simultaneous bioimaging and targeted photodynamic therapy in vitro and in vivo

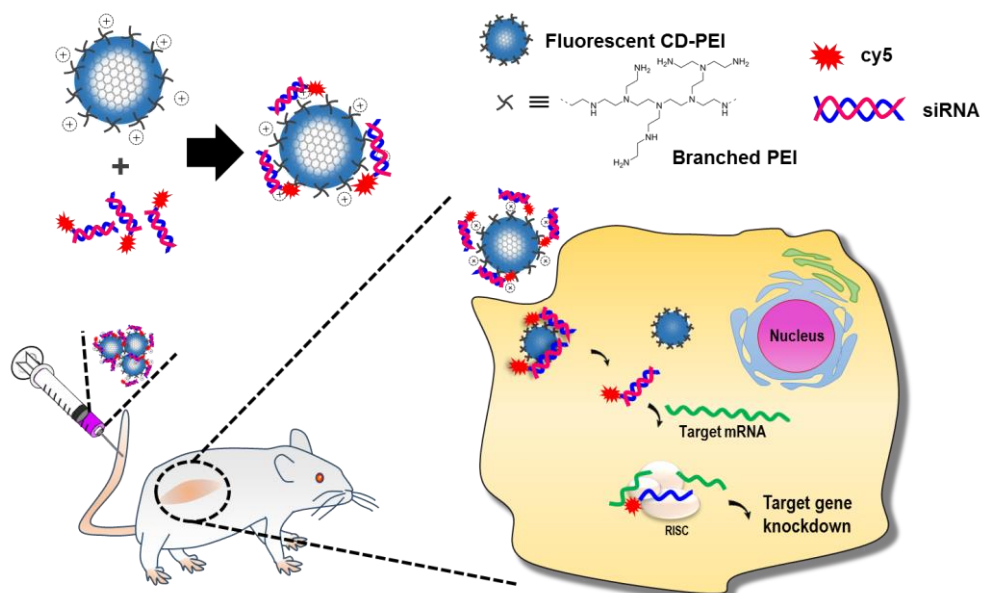
We describe a novel design of highly biocompatible, fluorescent, folic acid (FA) and PEG-functionalized carbon nanodots (CDs) as carriers for zinc phthalocyanine (ZnPc) PS to achieve simultaneous biological imaging and targeted photodynamic therapy. CD-PEG-FA/ZnPc exhibits excellent targeted delivery of the PS, leading to simultaneous imaging and significant targeted photodynamic therapy after irradiation in vitro and in vivo.



Scheme 1.3. Schematic illustration of the preparation of CD from α -cyclodextrin and targeted photodynamic therapy with folic acid functionalized CD loaded with zinc phthalocyanine (CD-PEG-FA/ZnPc).

1.4.4. Highly efficient gene silencing and bioimaging based on fluorescent carbon dot in vitro and in vivo

We report a strategy for therapeutic RNA interference (RNAi) based on the highly biocompatible and fluorescent CD in which siRNAs are protected from RNase mediated degradation and have a longer half-life in vivo. Our strategy allows simultaneous bioimaging and efficient down-regulation of gene expression, showing high potential for gene therapy in vitro and in vivo.



Scheme 1.4. Strategy of CD-PEI mediated siRNA delivery and

bioimaging. Complex of CD-PEI and siRNA is formed by electrostatic interaction between CD-PEI and siRNA. After cellular uptake of the siRNA/CD-PEI complex, siRNA is released from CD-PEI and the target gene knockdown is achieved by siRNA-RISC complex. Fluorescence of CD-PEI itself enabled fluorescent image based monitoring of cellular uptake of siRNA/CD-PEI complex and intracellular localization of CD-PEI in living cells.

1.5. References

1. Terminology for nanomaterials. Publicly available specification 136. London: British Standards Institute, 2007. ([http:// www.nanointeract.net/x/file/PAS%20136.pdf](http://www.nanointeract.net/x/file/PAS%20136.pdf)).
2. Xia, Y.; Xiong, Y. J.; Lim, B.; Skrabalak, S. E. *Angew. Chem. Int. Ed.* **2009**, 48, 60.
3. Peer, D.; Karp, J. M.; Hong, S.; Farokhzad, O. C.; Margalit, R.; Langer, R. *Nat. Nanotechnol.* **2007**, 29, 205.
4. Wang, Y.; Li, Z.; Wang, J.; Li, J.; Lin, Y. *Trends Biotechnol.* **2011**, 29, 205.
5. Loh, K. P.; Bao, Q.; Eda, G.; Chhowalla, M. *Nat. Chem.* **2010**, 2, 1015.
6. Shen, He.; Zhang, L.; Liu, M.; Zhang, Z. *Theranostics* **2012**, 2, 283.
7. Morales–Narváez, E.; Merkoçi, A. *Adv. Mater.* **2012**, 24, 3298.
8. Chung, C.; Kim, Y. K.; Shin, D.; Ryoo, S. R.; Hong, B. H.; Min, D. H. *Acc. Chem. Res.* **2013**, 46, 2211.
9. Kim, J.; Park, S. J.; Min, D. H. *Anal. Chem.* **2017**, 89, 232.
10. Lee, J.; Kim, J.; Kim, S.; Min, D. H. *Adv. Drug Deliv. Rev.* **2016**, 105, 275.
11. Yang, S. T.; Cao, L.; Luo, P. G.; Lu, F.; Wang, X.; Wang, H.; Mezziani, M. J.; Liu, Y.; Qi, G.; Sun, Y. P. *J. Am. Chem. Soc.* **2009**, 131, 11308
12. Baker, S. N.; Baker, G. A. *Angew. Chem. Int. Ed.* **2010**, 49, 6726.

13. Zheng, X. T.; Ananthanarayanan, A.; Luo, K. Q.; Chen, P. *Small* **2015**, 11, 1620.
14. Zhang, T.; Liu, X.; Fan, Y.; Guo, X.; Zhou, L.; Lv, Y.; Lin, J. *Nanoscale* **2016**, 8, 15281.
15. Ray, S. C.; Saha, A.; Jana, N. R.; Sarkar, R.; *J. Phys. Chem. C* **2009**, 113, 18546.
16. Tang, J.; Kong, B.; Wu, H.; Xu, M.; Wang, Y.; Wang, Y.; Zhao, D.; Zheng, G. *Adv. Mater.* **2013**, 25, 6569.
17. Zhu, S.; Meng, Q.; Wang, L.; Zhang, J.; Song, Y.; Jin, H.; Zhang, K.; Sun, H.; Wang, H.; Yang, B. *Angew. Chem. Int. Ed.* **2013**, 52, 3953.
18. Zhu, A.; Qu, Q.; Shao, X.; Kong, B.; Tian, Y. *Angew. Chem. Int. Ed.* **2012**, 51, 7185.
19. Huang, P.; Lin, J.; Wang, X.; Wang, Z.; Zhang, C.; He, M. *Adv. Mater.* **2012**, 24, 5104.
20. Hola, K.; Zhang, Y.; Wang, Y.; Giannelis, E. P.; Zboril, R.; Rogach, A. L. *Nanotoday* **2014**, 9, 590.

Chapter 2. *Therapeutic application of graphene oxide*

2.1. Deoxyribozyme-loaded nano-graphene oxide for simultaneous sensing and silencing of hepatitis C virus gene in liver cells

2.1.1. Introduction

DNAzyme (deoxyribozyme, Dz) is a RNA-cleaving antisense oligodeoxyribozyme which mediates catalytic hydrolysis of target mRNA in a sequence-specific manner.¹ Dz has been used in wide research areas as a therapeutic candidate of diseases associated with abnormal gene expression² and sensitive detection of metal ions.^{3,4} The most popular DNAzyme is the “10–23” DNAzyme, consisting of a catalytic core of 15 bases and flanking sequences of 6–12 bases, respectively, responsible for catalytic RNA cleavage and sequence specific recognition of target RNA.⁵ Among oligonucleotides which induce gene down-regulation including ribozyme, short interfering RNA (siRNA) and antisense oligonucleotide, Dz is especially attractive due to advantages

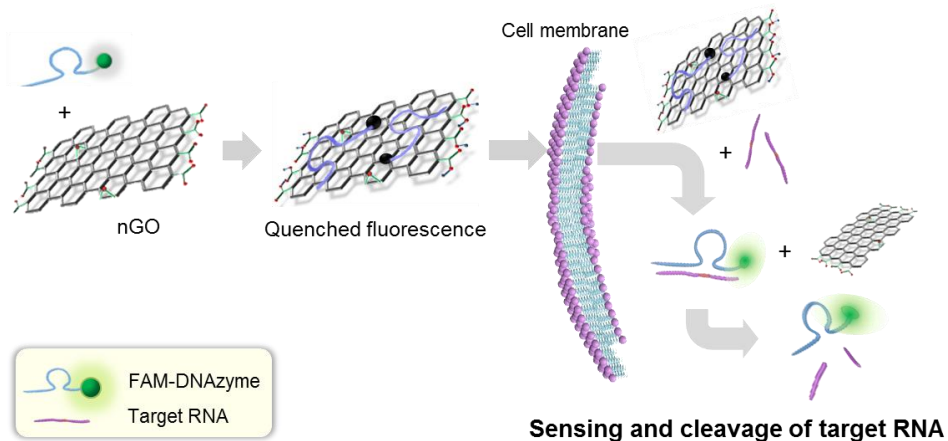
such as cost effectiveness and relatively high chemical stability in serum compared to RNA.⁶ In addition, the catalytic activity of Dz is independent of any cellular machinery unlike siRNA which requires the RNA-induced silencing complex (RISC) for target RNA degradation, the process referred to as RNA interference (RNAi).⁷ Therefore, Dz offers flexible therapeutic modality for suppression of target gene expression in various diseases including cancer and viral infection. However, clinical and practical applications of Dz necessitate the development of a safe and efficient intracellular Dz delivery system.

Hepatitis C virus (HCV), a positive sense single-stranded RNA virus, infects more than 180 million people around the world and is one of the major causes of chronic liver damage and hepatocellular carcinoma.⁸ In spite of its seriousness, no vaccine or effective therapy is currently available for hepatitis C. The current standard therapy for HCV infection involves interferon- α (immune booster) and ribavirin (general inhibitor of virus replication) that are known to have limited efficacy and produce serious side effects including cough, anemia,

muscle ache, and depression.⁸ Among various approaches to develop a directacting anti-HCV agent for effective treatment of hepatitis C, Dz is an attractive potential therapeutic agent to cleave HCV gene and subsequently prevent viral replication in human host cells.⁹

Here, we report a nano-sized graphene oxide (nGO)-based system for the intracellular delivery of Dz that targets mRNA of HCV nonstructural gene 3 (NS3) in human liver cells to treat hepatitis C by directly prohibiting HCV gene replication (Scheme 2.1). The N-terminal one-third of the NS3 proteins plays a role as serine protease and the remainder has RNA helicase activity, which are essential for HCV replication in human liver cells.¹⁰ Therefore, direct inhibition of HCV NS3 protein expression leads to prevention of HCV replication. To date, GO has been employed in diverse biosensors and drug delivery systems.¹¹ It was reported that nGO facilitated intracellular delivery of oligonucleotides.¹² In the present study, nucleobases of Dz effectively binds to the surface of nGO and subsequently, fluorescence from the dye conjugated to the 5'-end of Dz is quenched. Then, the

detachment of the Dz from nGO is induced by its double helix formation in the presence of a complementary target sequence with recovery of the fluorescence due to loss of proximity with nGO, followed by catalytic cleavage of the target sequence which is HCV NS3 mRNA in this study. Therefore, the Dz/nGO complex serves as a sensor to monitor the presence and location of the HCV gene in live mammalian cells and as a potential therapeutic agent to down-regulate HCV NS3 expression by sequence specific mRNA cleavage to inhibit HCV replication in host cells simultaneously.



Scheme 2.1. Strategy of detection and knockdown of target gene in mammalian cells based on Dz and nGO. nGO allows efficient intracellular delivery of Dz and serves as a fluorescence quencher.

2.1.2. Materials and methods

Materials. MTT (3-(4,5-dimethylthiazol-2-yl)-2,5-diphenyl tetrazolium bromide) was purchased from Sigma, U.S.A. 10X PBS (Phosphate Buffered Saline), DMEM (Dulbecco's Modified Eagle's Medium), and FBS (Fetal Bovine Serum) were purchased from WELGENE, Korea. SYBR® Gold nucleic acid gel stain was purchased from Life technologies, USA. DNase I was purchased from New England Biolabs, USA. All Dz derivatives and siRNA were purchased from Genotech and Bioneer, Korea.

Preparation of nGO. GO was synthesized from graphite following a modified Hummers method. The dried GO was dispersed in distilled water (3 mg/mL) and the dispersion was placed under bath-sonication for 6 h maintaining the temperature not to excess 40 °C by adding ice to the water bath to obtain nGO. The resulting dark brown solution was filtered through a Büchner funnel and washed with copious amount of distilled water. The yield of the prepared nGO was roughly estimated as ~30–50% based on the weight of obtained nGO per the weight of graphite. The dried filter cake

was re-dispersed in distilled water to make the final concentration of 1 mg/ml. The zeta potential of synthesized nGO was measured as -18.2 ± 0.53 mV in PBS (pH 7.4) by a Zetasizer Nano ZS (Malvern instruments, U.K.).

Characterization of nGO. The atomic force microscopy (AFM) analysis was carried out to determine the thickness and lateral size of nGO sheets by XE-100 (Park System, Korea) with backside gold-coated silicon SPM probes (M to N, Korea). UV-vis spectrum of nGO was obtained with a UV-2550 (Shimadzu, Japan). Raman spectrum of nGO was obtained by LabRAM HR UV-vis-NIR (Horiba Jobin Yvon, France) using a 20 mW Ar ion CW laser (514.5 nm) as an excitation source focused through a BXFM confocal microscope equipped with an objective (50X, numerical aperture=0.50). Elemental analysis was carried out by EA1110-FSIONS for carbon and Flash EA 1112 for oxygen.

Loading capacity test. To estimate the loading capacity of Dz to nGO, the fluorescence emission spectra of FAM-Dz and FAM-labelled scrambled-sequence DNzyme (FAM-scDz) were obtained at excitation wavelength 492 nm with or

without nGO in PBS by using a fluorometer (BioTek, USA). Loading capacity was calculated from the degree of FAM fluorescence quenching by binding of DNAzyme to nGO.

Fluorescence recovery test in buffer solution. Recovery of fluorescence intensity of Dz/nGO upon addition of target HCV NS3 RNA was measured to elucidate the sequence selectivity of the Dz/nGO for target RNA sensing. FAM–Dz and FAM–scDz (5 pmol) were first mixed with nGO in 50 μ l PBS for 10 min, followed by incubation with different molar ratios of target HCV NS3 RNA (1:1, 1:2, 1:4) for 30 min at room temperature in triplicate. The fluorescence emission spectra of FAM were obtained at emission wavelength 520 nm by using a fluorometer (BioTek, USA). To measure the limit of detection (LOD), 50 pmol of FAM–Dz was first mixed with nGO, resulting in 95% fluorescence quenching. A total of 25 μ l of FAM–Dz/nGO solution was mixed with 25 μ l of target mRNA in a 96–well plate, followed by addition of various concentrations of mRNA (0.02–1 μ M). The fluorescence emission spectra of FAM were obtained at emission wavelength 520 nm by using a fluorometer (BioTek, USA). All

the samples were prepared in triplicate. We calculated the LOD of FAM-Dz/nGO system by using the equation of “LOD = 3.3(standard deviation/slope of the calibration curve)”. We measured the quantum yields and extinction coefficients of FAM-Dz/nGO with and without target mRNA, where 50 pmol of FAM-Dz and 6 ug of nGO in 300 ul constituted a stock solution and 50 pmol of target mRNA was added if applicable.

DNase protection assay. Polyacrylamide gel electrophoresis (PAGE) retardation assay was carried out to estimate the DNase protection ability of FAM-Dz/nGO complex. Various concentrations of DNase I (1.25–10 units) were first incubated with FAM-Dz or FAM-Dz/nGO in 50 μ l PBS for 30 min, followed by gel electrophoresis and SYBR gold staining. For the fluorescence detection, the fluorescence emission spectra of FAM-Dz were obtained at emission wavelength 520 nm by using a fluorometer (BioTek, USA).

Cell culture. Human hepatoma cell line Huh-7 (Naïve Huh7) was grown in DMEM containing 4.5 g/L D-glucose containing 10% FBS, 1% penicillin and streptomycin at 5% CO₂, 37 °C. To maintain Huh-7 cells carrying a subgenomic HCV replicon

(genotype 1b) and a luciferase reporter gene (abbreviated as Huh-7-rep), 500 µg/ml of G418 (A.G. Scientific, Inc. USA) was added to the above media.

Cell viability test of nGO. Huh-7-rep cells were seeded in a 96-well plate with a density of 1.0×10^4 cells/well in triplicate for 24 h and then incubated with different concentrations of nGO for 12 h. Next, the nGO treated cells were rinsed with 1X PBS and 200 µl of serum-free media and 20 µl of MTT reagent were added to each well. After 3 h, the MTT solution was removed and each well was rinsed, followed by addition of 200 µl of DMSO to dissolve insoluble purple formazan product. The absorbance was then measured at 560 nm using a microplate reader (Molecular Devices, Inc., USA). For the CCK-8 cell viability assay, we prepared Huh-7-rep cells (1×10^4 cells/well) in a 96-well plate for 24 h, followed by incubation with various concentrations of nGO with serum free medium. After 12 h incubation, the medium was replaced with fresh serum containing medium. The cells were then carefully washed with 1X PBS, then CCK-8 assay solution was added for 1 h, followed by measuring absorbance at 450 and 670 nm

using a microplate reader (Molecular Devices, Inc., USA).

Cellular uptake study. Huh-7-rep cells were seeded in a 12-well plate with a density of 1.2×10^5 cells/well. After 24 h incubation for 70–80 % cell confluency, FAM-Dz and FAM-scDz (500 pmol) loaded nGO complex were added to each well in serum-free media for 12 h at 5% CO₂, 37 °C (final volume was 500 µL). Then, cell media was changed to serum-containing fresh media and incubated for 2 h at 5% CO₂, 37 °C. After washing with 1X PBS, cell nuclei were stained with Hoechst 33342 via manufacturer's protocol at room temperature in dark to protect from light at least 5 min. Then, the cells were rinsed and the media was replaced with fresh media. Cell images were obtained using a Ti inverted fluorescence microscope with a 10X (1.4 numerical aperture) objective (Olympus, Japan).

Semi-quantitative RT-PCR and Western blot. When the cell confluency reached to 70–80% in a 12 well plate (1.2×10^5 cells/well), the cells were treated with Dz and scDz in serum-free media in complex with nGO. For lipofectamine (lipo)-mediated transfection, cells were incubated with Dz or scDz in

the presence of lipo for 4 h, the media was removed and the cells were rinsed with 1X PBS. Next, after addition of serum-containing media, the cells were further incubated for 44 h. For the treatment of Dz/nGO complex, 250 pmol and 500 pmol of Dz derivatives were prepared in 1XPBS containing nGO and then added to each well (final volume is 500 μ L). And the media was replaced with fresh serum-containing media after 12 h of incubation of cells with Dz/nGO complex, and then the cells were further incubated for 36 h before microscopic and functional evaluation. For the semi-quantitative RT-PCR (Reverse Transcription Polymerase Chain Reaction), total RNA was collected by using Trizol reagent (Invitrogen) based on manufacturer's protocol. Quantity and quality of the collected total RNA was estimated based on absorbance at 260 nm (A_{260}) and RNA/protein ratio (A_{260}/A_{280}) was measured by using a UV-Vis spectrophotometer (Nanodrop Take3 or fluorometer (BioTek, USA)). 1,000 ng of total RNA was used for reverse transcription by using Superscript II reverse transcriptase (Invitrogen) based on the manufacturer's protocol. The product cDNA was amplified by

PCR (BioRad, USA) using following primer pairs:

(1) HCV NS3 forward primer: 5'–CCT ACT GGT AGC GGC
AAG AG–3'

(2) HCV NS3 reverse primer: 5'–CTG AGT CGA AAT CGC
CGG TA–3'

(3) GAPDH forward primer: 5'–TTG TTG CCA TCA ATG
ACC CCT TCA TTG ACC–3'

(4) GAPDH reverse primer: 5'–CTT CCC GTT CTC AGC
CTT GAC GGT G–3'

The PCR reaction for HCV NS3 was performed as follows: 2 min at 95 °C, (60 s at 95 °C, 60 s at 62 °C, 30 s at 72 °C) × 35 cycles. The PCR reaction for GAPDH, used as housekeeping gene, was performed as follows: 5 min at 94 °C, (30 s at 94 °C, 30 s at 60 °C, 30 s at 72 °C) × 26 cycles. The product of PCR was separated by 1.2% TAE agarose gel and then analyzed by a Gel Doc (ATTO, Korea). Relative band intensities were quantified by using Image J software and NS3 gene expression level was normalized relative to GAPDH expression level. For Western blotting, the cell lysates were separated on SDS–PAGE, and transferred onto Immobilon–P

membranes (Millipore). The membranes were blocked with 5% skim milk and probed with primary antibody, anti-HCV NS3 (Virostat, USA) and anti-GAPDH antibody (ABFrontier). The membrane was then incubated with horseradish-peroxidase-conjugated secondary antibody (Sigma) and visualized by a Luminescent Image Analyzer (GE Healthcare, Sweden).

Flow cytometry. Huh-7-rep cells were seeded in a 12-well plate with a density of 1.2×10^5 cells/well. After 24 h incubation for 70–80% cell confluency, FAM-Dz (500 pmol) loaded nGO complex in serum-free media was added to each well and incubated for 12 h at 5% CO₂, 37 °C (final volume was 500 µl). Then, cell media was changed to serum-containing fresh media and incubated for 2 h at 5% CO₂, 37 °C. After washing with 1X PBS, trypsin-EDTA was added to cells for 3 min and then 10% FBS was added to cells, followed by centrifugation (5,000 rpm, 3 min). The cells then were washed with 1X PBS. The fluorescence intensity of the cells was measured by a flow cytofluorometer (Beckton Dickinson).

Time-dependent recovery of fluorescence. Huh-7-rep cells

were seeded in a 96-well plate with a density of 1.5×10^4 cells/well. After 24 h incubation, a solution of FAM-Dz (50 pmol) loaded nGO complex in serum-free media was added to each well for 12 h at 5% CO₂, 37 °C (final volume was 50 μl). The recovery of fluorescence in the cells was observed by using an IN CELL Analyzer 2000 (GE Healthcare Life Sciences, USA) at different time points.

2.1.3. Results and Discussion

GO was synthesized by oxidation of natural graphite based on a modified Hummers method.¹³ The synthesized GO sheets were cut into nano-sized sheets by sonication. Fig. 2.1a shows the AFM image and line profile with the size distribution of the synthesized nGO sheets (0–300 nm) and thickness corresponding to a single layer of nGO (0.97 nm). Typical D- and G-peaks in the Raman spectrum were observed at 1,354 and 1,594 cm^{-1} which originated from the disordered sp^3 - and ordered sp^2 -hybridized structures, respectively (Fig. 2.1b). UV-vis spectroscopy revealed the presence of an absorption peak at 232 nm from π - π^* transition of the aromatic C-C bond (Fig. 2.1c).¹⁴ The C/O ratio of nGO was 1.26 (Fig. 2.1d).

The cytotoxicity of nGO to Huh-7 cells carrying a subgenomic HCV replicon (Huh-7-rep) was first evaluated by MTT and CCK-8 cell viability assays (Fig. 2.1e). The relative cell viability of Huh-7-rep was measured to be above 90% after incubation with nGO up to a concentration of 450 mg/ml. The nGO showed little cytotoxicity at the

concentrations we use in the present study (the highest concentration of nGO used for Dz delivery in this study = 50 mg/ml).

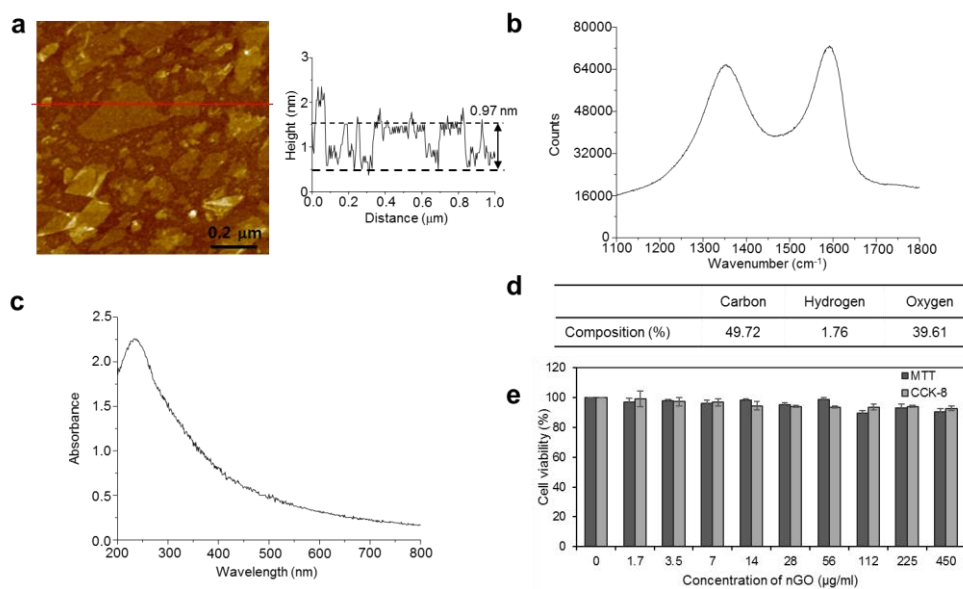


Figure 2.1. Characterization of nGO. a) AFM image and line profile of nGO showed width and height of nGO as approximately 0~300 nm and 0.97 nm, respectively. b) Raman spectrum of nGO showed D peak at $1,354\text{ cm}^{-1}$, G peak at $1,594\text{ cm}^{-1}$, respectively, giving $I_D/I_G = 0.90$. c) UV-vis spectrum of nGO. d) Elemental analysis to estimate the content of each element of nGO. e) Cell viability of Huh-7-rep cells incubated with different concentration of nGO as mean values from triplicate.

To demonstrate our strategy for Dz delivery and HCV gene knockdown, we used Dz that contained a complementary sequence for mRNA of the HCV NS3 gene (Fig. 2.2a). Sequences of Dz to target HCV NS3 gene and scrambled sequence Dz (scDz) as a control were designed to investigate the sequence specificity of target NS3 RNA sensing and cleavage (Fig. 2.2b). FAM-labelled Dz at the 5'-end was prepared and their loading capacity on nGO was evaluated by fluorescence quenching of FAM upon addition of nGO. Fig. 2.2c shows that the fluorescence intensity of FAM-Dz decreased upon addition of nGO in a concentration-dependent manner. 0.5 mg of nGO was sufficient to quench 95% of fluorescence of 10 pmol FAM-Dz in 50 ml buffer (PBS). The quenched fluorescence of FAM-Dz was recovered upon addition of HCV NS3 RNA in PBS in a concentration dependent and sequence specific manner (Fig. 2.2d and Fig. 2.3).

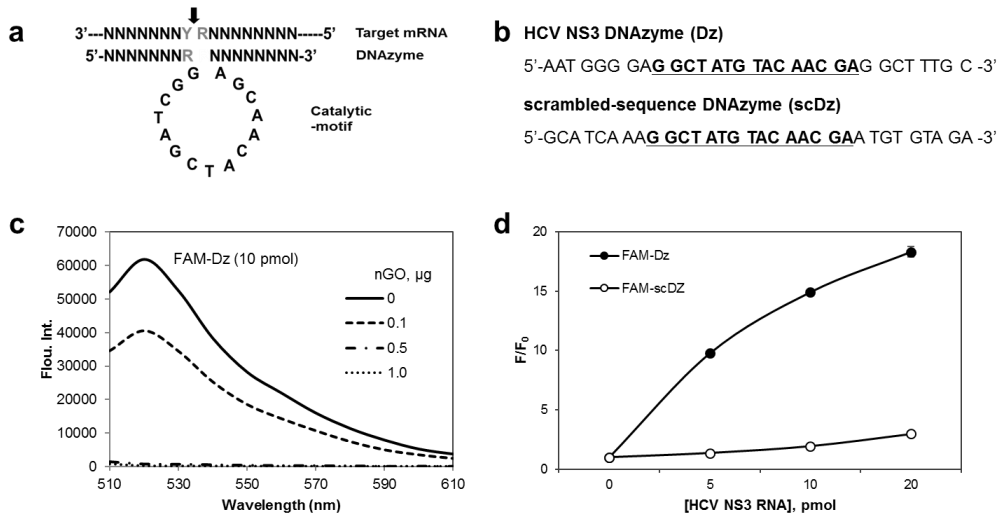


Figure 2.2. a) The structure of “10–23” DNAzyme. N, any nucleotide. Y and R are pyrimidine and purine nucleotide. The black arrow indicates the cleavage site. b) The sequences of designed HCV DNAzyme (Dz) and HCV scrambled–sequence DNAzyme (scDz). c), d) Fluorescence of FAM was quenched when the FAM–Dz and FAM–scDz were adsorbed on the surface of nGO in a concentration dependent manner.

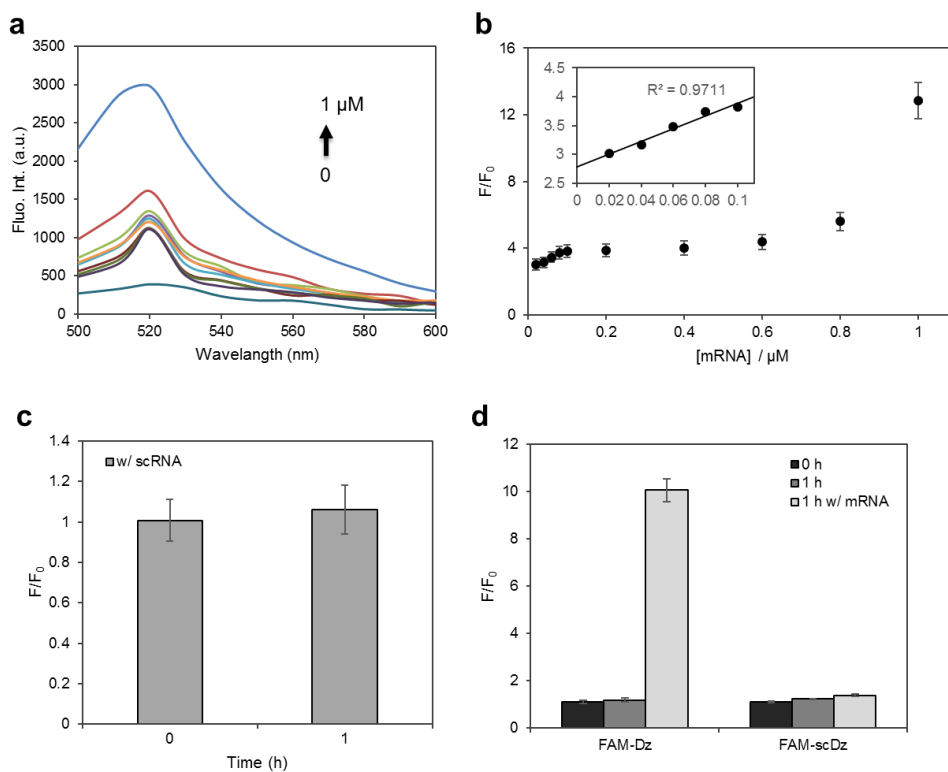


Figure 2.3. The fluorescence intensity of FAM–Dz. a),b) The quenched fluorescence of FAM–Dz by nGO was recovered increasingly upon the addition of the complementary mRNA in a concentration–dependent manner (0.02 – 1 μ M). c) The quenched fluorescence of FAM–Dz by nGO was stably maintained even after incubation with scRNA in the presence of serum for 1 h. d) The quenched fluorescence of FAM–Dz by nGO in the presence of serum was significantly recovered with addition of target mRNA but FAM–scDz/nGO did not show significant fluorescence increase with addition of mRNA.

Next, we investigated the protective effect of nGO against enzymatic cleavage of the adsorbed Dz by DNase I. It is important to maintain the chemical stability of Dz in a complex biological environment to carry out its function efficiently.¹⁵ Gel retardation assay was performed to estimate the degree of degradation of Dz in the presence of nGO after incubation with varying amounts of DNase I (1.25–10 units) in 50 ml PBS (Fig. 2.4a).¹⁶ In the presence of nGO, the degradation of Dz was hardly observed, an intense Dz band was seen even after treatment with 10 units of DNase I. However, Dz was completely degraded by DNase I without nGO, indicating that nGO protected the Dz from enzymatic cleavage by DNase I. The protective effect of nGO was further confirmed by fluorescence measurement of mixed solutions of the Dz and DNase I with or without nGO at the time of DNase I addition (Fig. 2.4b). As expected, the quenched FAM fluorescence only slightly recovered when DNase I was added to the FAM–Dz solution in the presence of nGO, indicating that Dz maintained its structure without significant degradation allowing continued tight interaction with the nGO surface.

However, FAM fluorescence of the Dz solution was highly intensified when DNase I was treated in the absence of nGO and then, nGO was added because the degraded FAM-Dz could not efficiently bind to nGO to induce fluorescence quenching. Collectively, DNase I-mediated cleavage of FAM-Dz was significantly inhibited by nGO.

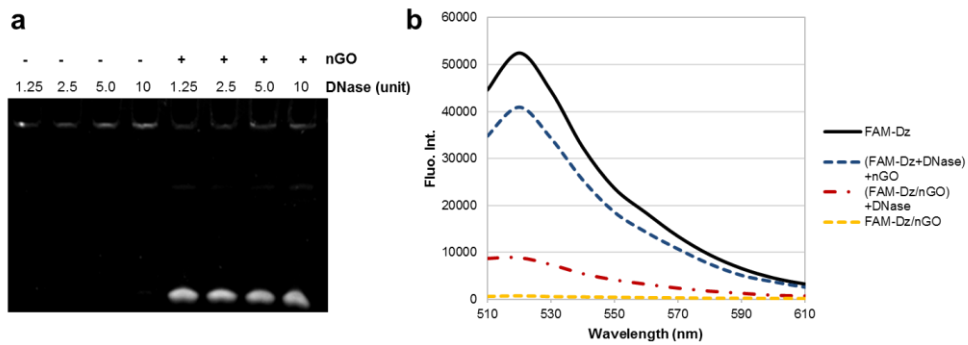


Figure 2.4. DNase protection assay. a) PAGE gel retardation assay for Dz incubated with different amounts of DNase (1.25, 2.5, 5.0, 10 units) in the presence or in the absence of nGO. Without nGO, Dz was completely degraded by DNase I whereas the Dz adsorbed to nGO was resistant to the DNase I-mediated cleavage. b) Fluorescence spectra of FAM-Dz after treated with DNase I, with or without nGO. Degradation of Dz by DNase I was inhibited by nGO, showing much less decrease of the fluorescence intensity upon treatment of DNase I in the presence of nGO compared to that of the Dz treated with DNase I in the absence of nGO, followed by addition of nGO.

We next investigated the cellular uptake of the FAM-Dz/nGO complex and sequence specific sensing of target RNA using fluorescence microscopy and flow cytometry. Huh-7 cells were cultured in a 12-well plate and treated with the FAM-Dz/nGO and FAM-scDz/nGO complex (50 mg/ml) for

12 h and each well was observed by using a fluorescence microscope (Fig. 2.5) and a flow cytometer (Fig. 2.6). The cell images showed that the green fluorescence corresponding to FAM was intense mostly at the perinuclear region in the FAM-Dz/nGO treated cells, suggesting that fluorescence of FAM was recovered by hybridization of FAM-Dz with target HCV NS3 mRNA and released from the nGO. However, FAM fluorescence was hardly observed in the FAM-scDz/nGO treated cells, which suggests that FAM-scDz remained in complex with nGO inside cells without desorption from the nGO surface. Collectively, the data indicated that the FAM-Dz/nGO complex readily passed through the cell membrane without assistance of a transfection reagent and the recognition of HCV NS3 mRNA by FAM-Dz and subsequent fluorescence recovery was sequence specific. The FAM-Dz/nGO complex successfully served as a turn-on sensor for HCV NS3 RNA in live human liver cells, which enabled real-time monitoring of the HCV gene at the mRNA level in living cells.

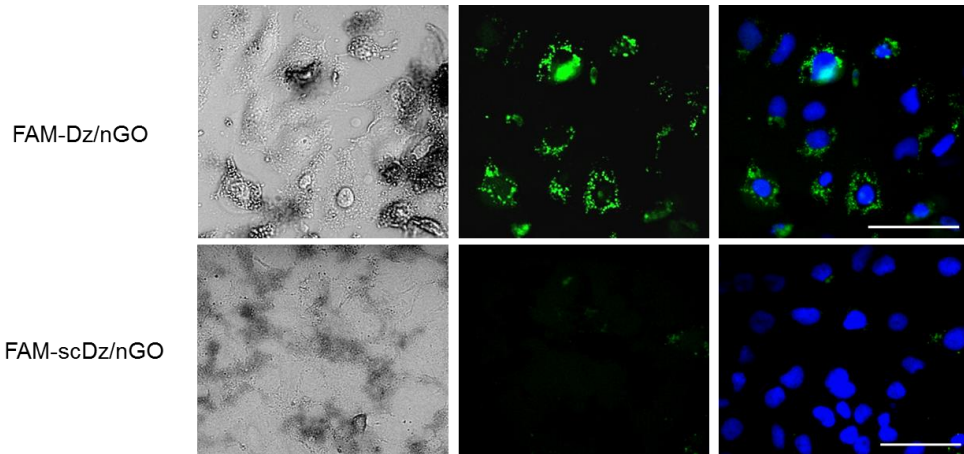


Figure 2.5. Fluorescence images of Huh-7-rep cells that were treated with FAM-Dz/nGO and FAM-scDz/nGO (1.0 μ M) for 12 h. Fluorescence of FAM was turned on only when the Dz complementary to target HCV NS3 RNA was used. Blue: nucleus stained with Hoechst 33342, green: FAM. Scale bar is 100 μ m.

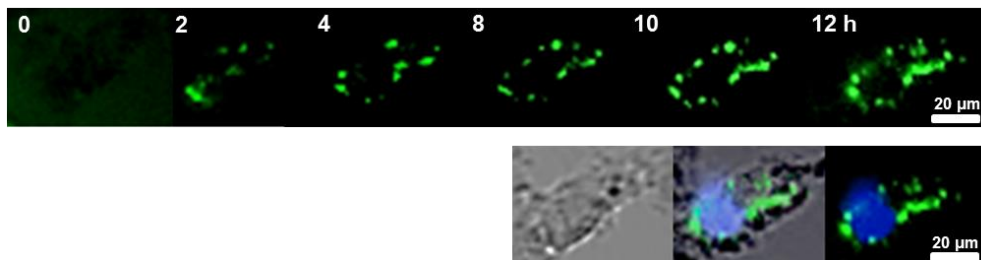


Figure 2.6. Fluorescence recovery in Huh-7-rep cell was observed over time after treatment with 1 μ M of FAM-Dz/nGO. The fluorescence of FAM-Dz gradually increased as time went by (0 – 12 h) in cytoplasm. Blue: nucleus stained with Hoechst 33342, Green: FAM.

Next, we evaluated the down-regulation of NS3 gene expression induced by FAM-Dz/nGO at both mRNA and protein levels. The NS3 proteins have functions as a serine protease and helicase which are essential for HCV replication in human liver cells¹⁰ and thus, silencing of NS3 gene expression has been considered as one of the therapeutic options to treat HCV infection. Huh-7-rep cells were first incubated with different concentrations of FAM-Dz loaded on nGO for 12 h. As a control, lipofectamine 2000 (lipo) was used in place of nGO. After 48 h post-transfection, cell media was removed and replaced with fresh serum-containing media. Then, the NS3 gene expression level was estimated by semi-quantitative RT-PCR and Western blotting. As a positive control for NS3 gene knockdown, siRNA targeting the IRES (Internal Ribosome Entry Sites, siIRES) that are located in the 5'-UTR and allow translation of the HCV RNA was used. Band intensities of HCV NS3 were normalized with respect to a housekeeping gene, GAPDH, both in gel electrophoresis of the RT-PCR product and Western blot. Lipo-mediated transfection of siIRES (denoted as 'positive (+) control') to

the Huh-7-rep cells induced significant downregulation of NS3 gene expression as expected both in RT-PCR and Western blotting, down to 23.6 and 53.6%, respectively (Fig. 2.7). RT-PCR and Western blot results showed efficient gene silencing of the NS3 gene via nGO-mediated transfection down to 32.6 and 26.0%, respectively, showing more effective knockdown of the NS3 gene than lipo-mediated Dz transfection which resulted in 57.3 and 30.2% of NS3 expression with the same concentration of Dz (1.0 μ M), respectively. scDz induced little knockdown of NS3, indicating that down-regulation of HCV NS3 by Dz was sequence specific. The data indicated that the Dz/nGO complex induced more efficient knockdown of HCV NS3, resulting in stronger gene suppression compared to the Dz-lipo complex both at mRNA and protein levels.

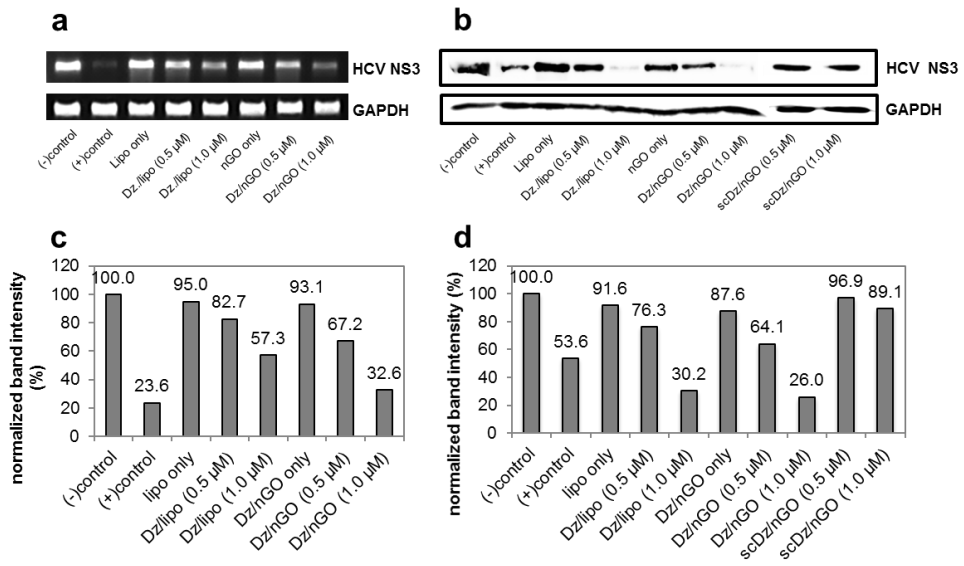


Figure 2.7. Expression levels of NS3 and GAPDH of Huh-7-rep cells were measured after incubation with Dz/nGO and scDz/nGO for 48 h. Gene expression levels were evaluated by a) semi-quantitative RT-PCR and b) Western blotting. c) and d) Normalized band intensities in a) and b) obtained by using Image J software.

2.1.4. Conclusion

In conclusion, we developed a Dz delivery system based on nGO and demonstrated that the FAM–Dz/nGO complex was successfully employed to knockdown HCV NS3 gene expression to potentially inhibit HCV replication in human cells as well as to monitor the presence of NS3 mRNA in living cells by fluorescence recovery of FAM–Dz by detachment from nGO and hybridization of target mRNA. The present system possesses many advantages as a potential theranostic nanomedicine to treat viral infection. First, the whole nanocomplex is relatively cost effective; Dz is more economical than siRNA and ribozyme, and nGO can be easily prepared from graphite with low cost compared to other nanomaterials like noble metal nanomaterials and carbon nanotubes. Second, Dz itself possesses a highly sequence specific and efficient catalytic function which is independent of RNAi requiring RISC. Also, Dz is chemically more stable than RNA. Third, for its loading and intracellular delivery, Dz does not require any chemical modification. Other systems such as gold nanoparticle–mediated delivery require functionalization

of DNA with a thiol moiety for DNA loading onto the surface of the nanoparticle, where modification at an inappropriate position (5' or 3'-end) often impedes its function.¹⁷ Our system simply utilizes $\pi - \pi$ stacking interaction between nucleobases of Dz and the surface of nGO. Further, this simple strategy allows convenient nanocomplex preparation—just mixing two solutions of nGO and Dz in PBS. Most importantly, the Dz/nGO complex allows simultaneous monitoring of the HCV gene in the infected host cells and sequence specific silencing of the target HCV gene expression, prohibiting viral replication. We expect that the Dz/nGO complex will be one of the promising theranostic tools for HCV infection and further, applicable to other types of viral diseases in the future.

2.1.5. References

1. Michell, A.; Dass, C. R.; Sun, L. Q.; Chesterman C. N. and Khachigian, L. M. *Nucleic Acids Res.* **2004**, 32, 3065.
2. Dash, B. C. and Banerjea, A. C. *Oligonucleotides* **2004**, 14, 41.
3. Pelossof, G.; Tel-Vered, R. and Willner, I. *Anal. Chem.* **2012**, 84, 3703.
4. Yin, B.-C.; Ye, B.-C.; Tan, W.; Wang, H. and Xie, C.-C. *J. Am. Chem. Soc.* **2009**, 131, 14624.
5. Lee, B.; Kim, B. K.; Oh, S.; Choi, J. S.; Park, J.-S.; Min, D.-H. and Kim, D.-E. *Oligonucleotides* **2010**, 20, 285.
6. Appaiahgari, M. B.; and Vрати, S. *Mol. Ther.* **2007**, 15, 1593.
7. Fire, A.; Xu, S.; Montgomery, M. K.; Kostas, S. A.; Driver, S. E. and Mello, C. C. *Nature* **1998**, 391, 806.
8. Brody, H. *Nature* **2011**, 474(7350), S1.
9. Ryoo, S.-R.; Jang, H.; Kim, K.-S.; Lee, B.; Kim, B. K.; Kim, Y.-K.; and Min, D.-H. *Biomaterials* **2012**, 33, 2754.
10. Jang, H.; Ryoo, S.-R.; Kim, Y.-K.; Yoon, S.; Kim, H.; Han, S.W.; Choi, B.-S.; Kim, D.-E. and Min, D.-H. *Angew. Chem., Int. Ed.* **2013**, 52, 2340.
11. a) Chung, C.; Kim, Y.-K.; Shin, D.; Ryoo, S.-R.; Hong, B. H. and Min, D.-H. *Acc. Chem. Res.* **2013**, 46, 2211. b) Yang, X.; Niu, G.; Cao, X.; Wen, Y.; Xiang, R.; Duan, H. and Chen, Y. *J. Mater. Chem.* **2012**, 22, 6649. c) Liu, Z.; Robinson, J. T.; Sun, X.; and Dai, H. *J. Am. Chem. Soc.* **2008**, 130, 10876. d) Zhang, L.; Xia, J.; Zhao, Q.; Liu, L.

- and Zhang, Z. *Small* **2010**, 6, 537. e) Mohanty, N. and Berry, V. *Nano Lett.* **2008**, 8, 4469. f) Balapanuru, J.; Yang, J. X.; Xiao, S.; Bao, Q.; Jahan, M.; Polavarapu, L.; Wei, J.; Xu, Q. H. and Loh, K. P. *Angew. Chem. Int. Ed.* **2010**, 49, 6549. g) Tang, L. A.; Wang, J. and Loh, K. P. *J. Am. Chem. Soc.* **2010**, 132, 10976. h) Lu, C. H.; Yang, H. H.; Zhu, C. L.; Chen, X. and Chen, G. N. *Angew. Chem. Int. Ed.* **2009**, 48, 4785. i) He, S.; Song, B.; Li, D.; Zhu, C.; Qi, W.; Wen, Y.; Wang, L.; Song, S.; Fang, H. and Fan, C. *Adv. Funct. Mater.* **2010**, 20, 453. j) Cui, L.; Lin, X.; Lin, N.; Song, Y.; Zhu, Z.; Chen, X. and Yang, C. J. *Chem. Commun.* **2012**, 48, 194. Kang, J.; Kim, H.; Kim, K. S.; Lee, S. K.; Bae, S.; Ahn, J. H.; Kim, Y. J.; Choi, J. B.; Hong, B. H. *Nano Lett.* **2011**, 11, 5154.
12. Wang, Y.; Li, Z.; Hu, D.; Lin, C. T.; Li, J. and Lin, Y. *J. Am. Chem. Soc.* **2010**, 132, 9274.
13. Hummers, W. S. and Offeman, R. E. *J. Am. Chem. Soc.* **1958**, 80, 1339.
14. Kim, Y.-K. and Min, D.-H. *Langmuir* **2012**, 28, 4453.
15. Schubert, S.; Gul, D. C.; Grunert, H.-P.; Zeichhardt, H.; Erdmann, V. A. and Kurreck, J. *Nucleic Acids Res.* **2003**, 31, 5982.
16. Lu, C.-H.; Zhu, C.-L.; Li, J.-J.; Chen, X. and Yang, H.-H. *Chem. Commun.* **2010**, 46, 3116.
17. Yehl, K.; Joshi, J. P.; Greene, B. L.; Dyer, R. B.; Nahta, R. and Salaita, K. *ACS Nano* **2012**, 6, 9150.

2.2. Enhancing intracellular accumulation of antibiotic drug and combinational treatment of hepatitis C virus related hepatocellular carcinoma via functionalized graphene oxide in vitro and in vivo

2.2.1. Introduction

Chemotherapy is the most effective and widely applied treatment in various type of cancer and viral disease through inhibition of cancer cell growth and viral replication as a function of neo-adjuvant chemotherapy of pre-surgery to contract the tumor volume to be excised and adjuvant chemotherapy of post-surgery to remove the left tumor cells, respectively.^{1,2} Nevertheless, it is well known that chemo effect also damages to the normal cells and thus, the dose-dependent side effect of the medication is unfortunately triggered such as mouth sores, nausea, and hair loss.^{3,4} Moreover, the decrease of cellular uptake and increase of energy-dependent effluent from the cells have emerged because of the hydrophobic structure of antibiotic drugs,

which render the resistance of cancer cells against the uptaken drug.⁵⁻⁸

With undesired results including dosages, resistances, and other reason affecting treatment, a number of combinational therapy has been invented over several decades in which more than one therapeutic method is administered to treat disease. Such genetic molecular approach including protein and nucleic acid has been discovered to provide an attractive solution for overcoming conventional limit regarding the small molecules.⁹⁻¹² Especially, small interfering RNA (siRNA) is an attractive therapeutic candidate for cancer and viral disease treatment through down-regulating target gene expression through RNA interference (RNAi) mediated cleavage of specific messenger RNA (mRNA).¹³⁻¹⁹ By combining the individual advantage for the mechanism of antibiotic drug-mediated apoptosis and RNAi-modulated gene expression knockdown, a desirable combinational therapy can be accomplished as a novel therapeutic candidate for the treatment of serious diseases.

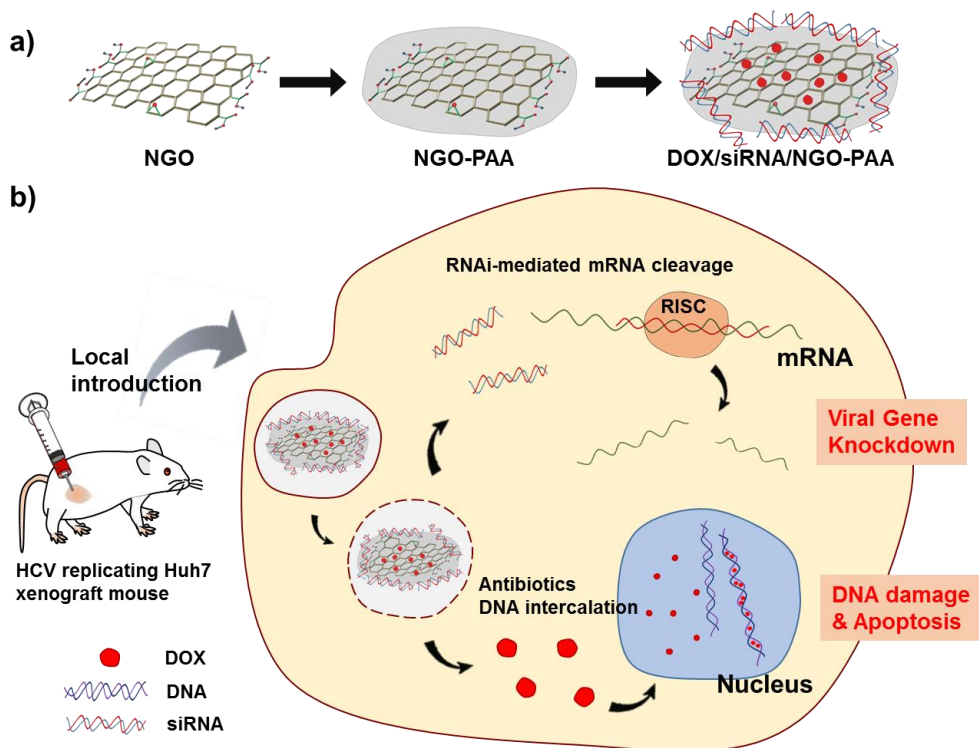
Hepatitis C is an infectious liver disease caused by the

Hepatitis C virus (HCV) which a small, enveloped and positive-sense single-stranded RNA virus. More than 180 million people around the world are infected and the post-viral infection leads to chronic liver damage including hepatocellular cirrhosis and carcinoma.²⁰⁻²⁴ Peginterferon (PEG-IFN- α , immune booster) and ribavirin (a general inhibitor of virus replication) combinations are the representative treatment of HCV infection so far, and several inhibitors of HCV as a protease inhibitor (boceprevir, simeprevir, and telaprevir) and nucleotide analog inhibitor (sofosbuvir) targeting HCV nonstructural protein are currently approved. However, both standard and newer treatment still remain challenges of cost-ineffectiveness, undesired immune response and serious side effects such as fatigue, headache, nausea, insomnia, depression, and etc.²⁵⁻³⁰ Infectious virus generally depends on the metabolism of its host cells and viral replication can only take place inside the cells. Moreover, the overexpression of HCV proteins has an oncogenic potential by activating oncogenic molecular pathways in mouse model, indicating that chronic HCV

infection is regarded to be a prominent disease factor for development hepatocellular carcinoma (HCC) through indirect pathways such as chronic inflammation, transformation, and cellular proliferation.³¹⁻³⁵ Therefore, there is an urgent need to investigate the effective therapeutic system for treatment of HCV infection.

Here, we developed a novel combinational therapeutic system to treat HCV-related HCC based on graphene oxide (GO) to be used for delivery of antibiotic drug and siRNA simultaneously in an aqueous formulation. To date, GO has been applied in diverse biosensors and drug delivery systems due to the unique physical/chemical characteristics.³⁶⁻⁵² In this strategy, GO was covalently functionalized with polyallylamine (PAA) which is a cationic biocompatible polymer and has been widely applied for drug delivery area⁵³ through the simple synthetic process of epoxy-ring opening reaction. To investigate the potential for clinical application of designed nanoparticle, the functionalized GO was utilized as a co-carrier of high concentration of antibiotic drug possessing hydrophobic structure by π - π interaction and hydrogen

bonding interaction as well as siRNA having negatively charged phosphate backbone by electrostatic interaction. The both drug and gene loaded GO was successfully employed for sequence-specific knockdown of target gene expression of HCV nonstructural gene 3 (NS3) possessing serine protease and the remainder of RNA helicase activity which are essential for HCV replication as well as induced apoptosis by inhibition of replicating DNA via intercalation in human liver cells without systemic toxicity, supporting the synergistic efficacy through individual pharmacological effect to treat HCV-infected liver cells in vitro and in vivo. (Scheme 2.2)



Scheme 2.2. The strategy of GO mediated combinational therapy. a) NGO was the functionalized with PAA through simple synthetic process of epoxy–ring opening reaction and NGO–PAA was utilized as a co–carrier of high concentration of antibiotic drug possessing hydrophobic structure by $\pi - \pi$ interaction and hydrogen bonding interaction as well as siRNA having negatively charged phosphate backbone by electrostatic interaction. b) The DOX/siRNA loaded NGO–PAA enabled sequence–specific knockdown of target gene expression of HCV nonstructural gene 3 (NS3) as well as inhibition of replicating DNA via intercalation of antibiotics in human liver cells.

2.2.2. Materials and methods

Materials. Doxorubicin hydrochloride and poly(allylamine hydro-chloride) were purchased from Sigma-Aldrich, Korea. Graphite (FP 99.95% pure) was purchased from Graphite Kropfmühl AG, Germany. Sodium nitrate, sodium sulfate, potassium hydroxide, and hydrogen peroxide (30% in water) were purchased from Junsei, Japan. Nitric acid and sulfuric acid were purchased from Samchun, Korea. CCK-8 assay kit was purchased from Dojindo Molecular Technologies, Inc, USA. 10x PBS (Phosphate buffered saline), DMEM (Dulbecco's modified eagle's medium), FBS (Fetal bovine serum), and P/S (penicillin and streptomycin, 100x) were purchased from WELGENE, Korea. SYBR® Gold nucleic acid gel staining solution and Trizol for total RNA isolation, and Superscript II reverse transcriptase were purchased from Life technologies, USA. RNase was purchased from New England Biolabs, USA. All primer and siRNA were purchased from Genotech and Bioneer, Korea.

Preparation of NGO and NGO-PAA. GO was synthesized from graphite based on modified Hummers method and further

bath-sonication at 4 °C for 6 h produced NGO (< 200 nm). To prepare NGO-PAA, PAA was conjugated to NGO basal surface by epoxy-ring opening reaction following a little modification. In briefly, 100 mg of KOH and 80 mg of PAAH were dissolved in 100 mL of water and 20 mg of NGO powder was dissolved sequentially in solution. The suspension was bath-sonicated at 4 °C for 1 h, followed by vigorous stirring at 70 °C for 24 h. After cooling to room temperature, NGO-PAA was collected by dialysis for 48 h.

Characterization. The study of morphological image and thickness was carried out by using atomic force microscopy (XE-100, Park System) with 30 nm thick aluminum backside re-flex coated probe (non-contact cantilever). UV-vis-NIR spectrum of NGO and NGO-PAA was obtained with a UV-2550 (Shimadzu, Japan). Raman spectrum of NGO was obtained by LabRAM HR UV/vis/NIR (Horiba Jobin Yvon, France) using a 20 mW Ar ion CW laser (514.5 nm) as an excitation source focused through a BXFM confocal microscope equipped with an objective (50x, numerical aperture=0.50). FT-IR spectrum was characterized Nicolet

iSTM 10 FT-IR spectrometer (Thermo Fisher Scientific, USA) using the KBr pellet. Hydrodynamic radius and zeta potential were measured by zetasizer NS90 (Malvern, UK).

siRNA Loading to NGO-PAA and heparin polyanion competition assay. The polyacrylamide gel electrophoresis (PAGE) analysis was performed to measure the loading capacity and heparin polyanion competition assay of siRNA/NGO-PAA complex. Fifty pmol of siRNA was incubated with various concentrations (0–2 μg) of NGO-PAA in 20 μL 1x PBS. After 1 h incubation, the gel was stained with SYBR gold staining reagent. For heparin polyanion competition assay, heparin (0–50 μg) were added to the siRNA/NGO-PAA mixture prior to gel electrophoresis to induce the release of siRNA from NGO-PAA.

DOX loading and Release test. DOX was incubated with NGO-PAA in the buffered solution (pH 8.0) for 2 days. To quantify the loading capacity of DOX, filtration and washing were carried out 7 times by using 100 kDa filter (Amicon, Ultra Centrifugal Filter, Merk Millipore), followed by measuring absorbance (@490 nm) and fluorescence (@590 nm) of the

supernatant. For DOX release test, the fluorescence of DOX was measured in DOX/NGO–PAA mixture in buffered solution (pH 5.0 and pH 7.4) and GSH (5 mM) treated solution (1x PBS).

RNase protection study. PAGE retardation assay was carried out to estimate the RNase protection ability of siRNA/NGO–PAA complex. Twenty–five microgram of RNase was incubated with siRNA/NGO–PAA in 20 μ L of PBS at RT for 30 min, followed by further incubation with heparin for 30 at RT for 30 min. Each band was monitored after SYBR gold staining by using a Gel Doc (ATTO, Korea).

Cell culture. Human hepatoma cell line Huh–7 carrying subgenomic HCV replicon (genotype 1b) and a luciferase reporter gene (abbreviated as Huh7–rep, adopted from prof. Bartenschlager) was grown in DMEM containing 4.5 g/L D–glucose containing 10% FBS, 1% penicillin and streptomycin, 500 μ g/mL of G418 (A.G. Scientific, Inc. USA) at 5% CO₂, 37 °C.

Cell viability assay. To measure the biocompatibility of NGO–PAA for bio–logical application, Huh7–rep cells (1×10^4

cells/well) were prepared in a 96-well plate in triplicate for 24 h, followed by incubation with various concentrations of NGO-PAA with complete medium. After 12 h incubation, the cells were then carefully washed with 1x PBS, then CCK-8 assay solution was added for 1 h with serum-free medium, followed by measuring absorbance at 450 and 670 nm with reduction calculation by using a microplate reader (Molecular Devices, Inc., USA). To calculate IC₅₀ for combinational therapy, the cells treated with DOX/siRNA/NGO-PAA were refreshed with complete medium, and CCK-8 assay was carried out for relative cell viability.

Cellular uptake study and flow cytometry. Huh7-rep cells were seeded in a 96-well plate at a density of 1.0×10^4 cells/well. After 24 h incubation for 70–80 % cell confluency, siRNA (50 nM), DOX (0.5 μ M), and NGO mixed complex were added to each well in serum-free media for 12 h (final volume was 100 μ L). Then, cell media was changed to serum-containing fresh media and incubated for 2 h. After washing with 1x PBS, cell nuclei were stained with Hoechst33342 via manufacturer's protocol. Then, the cells were rinsed and the

media was replaced with fresh complete medium. Fluorescence image of cells was obtained by using IN Cell Analyzer 2000 (GE Healthcare, USA). To investigate the time-dependent fluorescence distribution, the incubation time was controlled in 4, 12, and 24 h, followed by nucleus staining and monitoring the fluorescence in live cells by using IN Cell Analyzer 2000. For flow cytometry analysis, Huh7-rep incubated in different times were collected and rinsed with centrifugation (1,200 rpm, 3 min), then the 10,000 cells were measured by flow cytofluorometer (Beckton Dickinson, USA).

RT-PCR and agarose gel analysis. Total RNA from the siRNA/NGO-PAA and siRNA/LF-treated cells (final volume = 500 μ L, [siRNA] = 50 nM) was collected after 48 h of incubations by using Trizol reagent based on the manufacturer's protocol. Quantity and quality of the collected total RNA were estimated based on absorbance at 260 nm (A_{260}) and RNA/protein ratio (A_{260}/A_{280}) was measured by using a UV-Vis spectrophotometer (Nanodrop Take3 and the fluorometer (BioTek, USA.)). 500 ng of total RNA was used for reverse transcription by using Superscript II reverse

transcriptase based on the manufacturer's protocol. The product cDNA was amplified by semi qRT-PCR (BioRad, USA) using following primer pairs:

(1) HCV NS3 forward primer: 5'-CCT ACT GGT AGC GGC AAG AG-3'

(2) HCV NS3 reverse primer: 5'-CTG AGT CGA AAT CGC CGG TA-3'

(3) β -actin forward primer: 5'-GCT CGT CGT CGA CAA CGG CTC-3'

(4) β -actin reverse primer: 5'-CAA ACA TGA TCT GGG TCA TCT TCT-3'

The PCR reaction for HCV NS3 was performed as follows: 2 min at 95 °C, (60 s at 95 °C, 60 s at 62 °C, 30 s at 72 °C) \times 30 cycles. The PCR reaction for β -actin, used as the housekeeping gene, was performed as follows: 5 min at 94 °C, (30 s at 94 °C, 30 s at 60 °C, 30 s at 72 °C) \times 26 cycles. The product of PCR was separated by 1.2% TAE agarose gel and then analyzed by a Gel Doc. Relative band intensities were quantified by using Image J soft-ware and NS3 gene expression level was normalized relative to β -actin

expression level

Anti-HCV efficacy in HCV replicated mouse model. All animal experiments were carried out in compliance with the Institutional Animal Care and Use Committees (IACUC) of Seoul National University. HCV mice model was prepared by implanting 1×10^6 of Huh7-rep cells to Balb/c nude male mouse with subcutaneous injection after one-week breeding. The validation of HCV replicon in tumors was carried out by immunohistochemistry with the monoclonal antibody against NS3 (Virostat, USA) and alexa488 conjugated antibody against mouse (Abcam, UK) after excising tumors and cryosection. Fluorescence images from stained tissue were obtained by using IX71 with 10x objective lens (Olympus, Japan). Anti-tumor efficacy was evaluated by measuring the change of tumor volume before/after injection of NGO-PAA, free DOX, free siRNA, DOX/NGO-PAA, DOX/siRNA/NGO-PAA (1 mg DOX/kg, 0.8 mg siRNA/kg, 100 μ L), and 1x PBS for 16 days (n=3). The tumor volumes were calculated by using following equation:

$$\text{Tumor volume} = \text{Length} \times (\text{width})^2 \times \frac{1}{2}$$

where the length and width are the longest and shortest diameters (mm) of the tumor, respectively. The tumor volumes were calculated relative to the initial volumes (100 mm³)

Histological Evaluation. Histological specimens were obtained by sacrificing mice at 16 days of injection. Samples from the heart, liver, spleen, lung, kidney, and tumor were obtained and placed in 4% polyformaldehyde (PFA) solution. The specimens were embedded in optimal cutting temperature (OCT) compound with sucrose infiltration, sectioned, and processed by using H&E staining (BBC Bio-chemical, Mt Vernon, WA, USA). The stained sections were observed under a BX71 microscope with 10x objective lens (Olympus, Japan)

Statistical analysis. P-values, referring to the statistical significance of at least three independent experiments, were determined based on the Student's t-test using GraphPad Software.

2.2.3. Results and Discussion

GO was successfully prepared followed by modified Hummers method and further bath sonication was carried out to exfoliate and decrease the size of GO thus, nano-sized GO (NGO) was synthesized.⁵⁴ Then polyallylamine (PAA) functionalized NGO (NGO-PAA) was prepared through epoxy-ring opening reaction at alkaline pH values toward hydrolysis of the epoxy group, creating secondary amine bond.^{55,56} The size and topological study of the NGO and NGO-PAA were observed by atomic force microscopy (AFM). The line-profile image showed that the diameters and thickness of NGO were ~150 nm and 1.5 nm, respectively, indicating the typical features of a single layer of NGO. In contrast, NGO-PAA showed approximately 200 nm size and increased the thickness of 8.35 nm respectively, corresponding to stepwise functionalization with PAA of NGO. (Fig. 2.8a and 2.8b). Ultraviolet-visible-near-infrared (UV-vis-NIR) absorption spectrum of NGO and NGO-PAA were shown in Fig. 2.8c. A typical absorption peak of GO at 230 cm^{-1} was observed by the π - π transition of aromatic carbon

bond and those of NGO-PAA showed the red-shift and increase in broad optical absorbance in visible and NIR range, supporting the partial restoration of sp^2 carbon structure domain. And Fourier transform infrared (FT-IR) spectroscopy indicated the change of functional groups. The characteristic peaks in NGO-PAA at C=O stretching ($1,730\text{ cm}^{-1}$) and O-H vibration ($3,423\text{ cm}^{-1}$) decreased slightly which was typically originated by GO chemical synthesis. In contrast, a new C-N stretching ($1,317\text{ cm}^{-1}$) appeared and an aliphatic C-H stretching ($2,920\text{ cm}^{-1}$) increased compared to those of NGO (Fig. 2.8d). Finally, the structure configurations of NGO and NGO-PAA were confirmed by Raman spectroscopy as shown in Figure 2.8e. Most of the graphite-derived carbon materials, i.e., graphene, GO, shows two major bands in the Raman spectra as the G mode arising from the first-order scattering of the E_{2g} phonon of C sp^2 atoms and the D mode arising from a breathing mode of κ -point photons of A_{1g} symmetry. The D band and G band were located at $1,352\text{ cm}^{-1}$ and $1,590\text{ cm}^{-1}$, respectively, which were the typical features of GO.⁵⁷⁻⁵⁹ The increased of relative D/G ratio

from 0.912 to 0.954 was observed in NGO–PAA, indicating the partial restoration of sp^2 domains generated from removal of oxygen groups upon the chemical functionalization and reduction. Dynamic light scattering (DLS) analysis showed the increase hydrodynamic diameter from NGO (98.2 ± 9.2 nm) to NGO–PAA (186.5 ± 9.8 nm), respectively. (Fig. 2.9a and 2.9b) The increase of diameters might be due to conjugation of PAA to NGO, which facilitate the maintenance of sheet of NGO–PAA strongly consistent with AFM result. Taken together, NGO–PAA was successfully prepared by PAA functionalization to NGO with the simple synthetic process. Moreover, the results indicated a promising opportunity to combinational therapy through the delivery of hydrophobic drug and negatively charged functional gene via the basal surface of NGO–PAA and PAA functionalization with the positive charge, respectively.

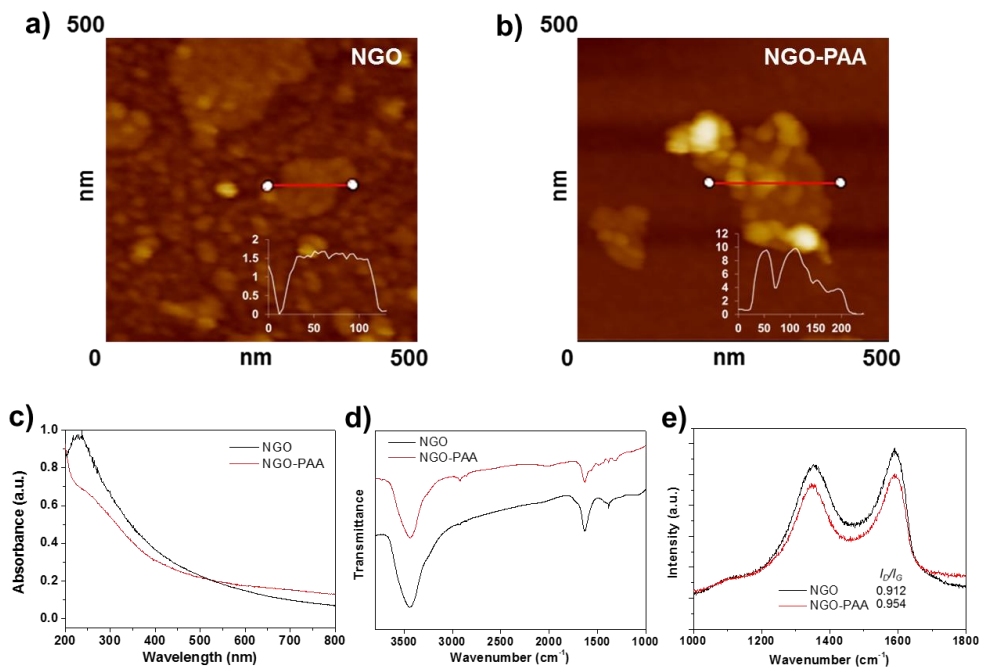


Figure 2.8. AFM study of morphological image and line-profile for thickness (inset) of a) NGO and b) NGO-PAA. The increase of width and height in NGO-PAA showed as approximately ~ 200 nm and 8.35 nm, respectively. c) UV-vis-NIR absorption spectrum showed red-shift of absorbance at $\pi-\pi$ transition of aromatic carbon bond of NGO-PAA by partial restoration of sp^2 carbon structure domain. d) FT-IR spectrum showed the change of transmittance in NGO-PAA by reduction and functionalization e) Raman spectrum of NGO-PAA indicated the increase of relative I_D/I_G ratio from 0.912 to 0.954.

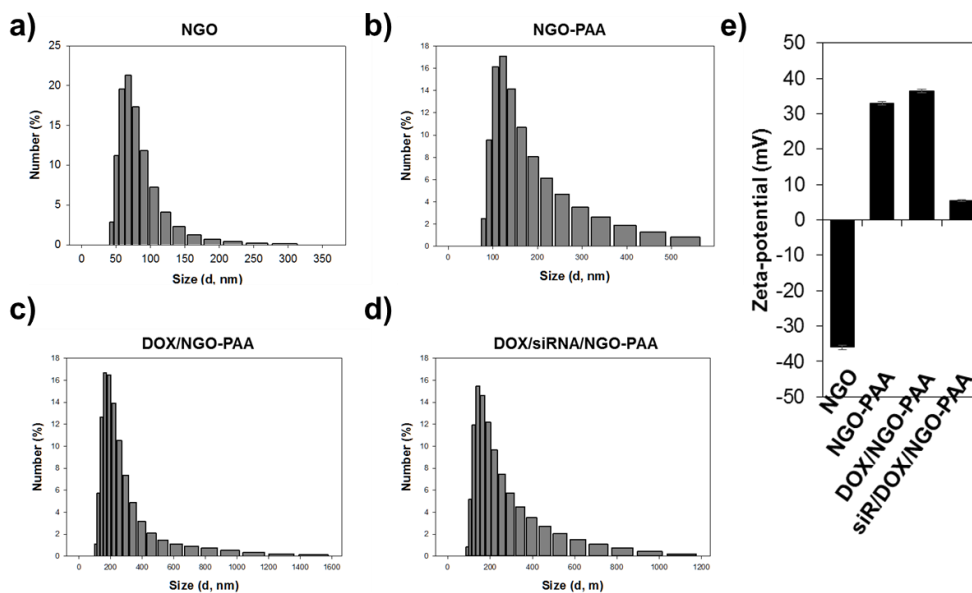


Figure 2.9. Size distribution and zeta potential value of NGO derivatives. a–d) The size was measured by dynamic light scattering method in buffered solution (pH 7.4). The size distribution was gradually increased according to modify the surface functionality and to form the complex condensed with DOX and siRNA. e) The surface charge of NGO derivatives was changed after surface modification with PAA and subsequent loading DOX and siRNA.

To demonstrate the capability of NGO–PAA as a delivery carrier of gene and small molecules, we used a siRNA which has an antisense complementary sequence for mRNA of HCV NS3 gene and a Doxorubicin (DOX) for medication of

chemotherapy. The N-terminal one-third of the NS3 proteins serves as a serine protease and a remainder has RNA helicase activity thus, NS3 is requisite for HCV replication in human liver cells.⁶⁰⁻⁶² Therefore, direct inhibition of HCV NS3 protein expression through mRNA degradation leads to prevention of HCV replication. siRNA loading capacity of NGO-PAA was evaluated by polyacrylamide gel electrophoresis (PAGE) analysis upon addition of NGO-PAA. siRNA/NGO-PAA complex was formed by electrostatic interaction between positive charge of NGO-PAA surface originated from amine functional groups and negative charge of siRNA derived from phosphate backbone, which facilitate the preparation of siRNA/NGO-PAA complex by simply mixing siRNA and NGO-PAA in phosphate buffered solution (PBS) for 1 h at room temperature. As shown in Figure 2.10a, the band intensity of siRNA decreased in accordance with the amount of NGO-PAA because of decrease of negative charge and increase of size thus, the migration of siRNA was inhibited at the electric field by successful complexation of siRNA/NGO-PAA. In this result, 1 μ g of NGO-PAA was

sufficient for estimating 50 pmol of siRNA loading capacity.

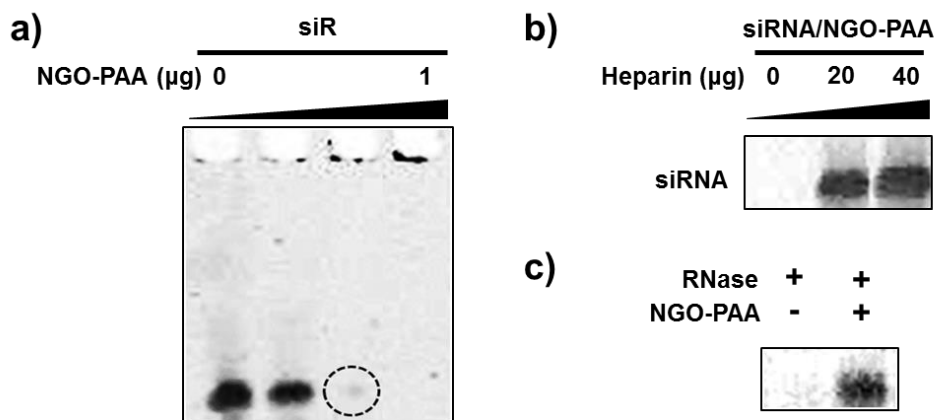


Figure 2.10. Poly acrylamide gel electrophoresis analysis for siRNA/NGO-PAA complexation. a) The band intensity of siRNA decrease in accordance with amount of NGO-PAA. b) Heparin polyanion competitive assay for siRNA release from NGO-PAA. c) siRNA protection ability of NGO-PAA by nuclease-mediated degradation in the presence of RNase.

To investigate successful mRNA cleavage and degradation by RNA interference (RNAi) in cells, maintenance of chemical stability of siRNA as well as the conditional release of siRNA should be secured in physiological conditions. Therefore, we

carried out heparin competitive assay to confirm the siRNA release from the NGO-PAA and ribonuclease (RNase) protection assay in vitro. Heparin, an anticoagulant, has been applied in the medical area and used as a reagent for facilitating the release of the anionic oligonucleotide from the cationic polymer.⁶³ As shown in Fig. 2.10b, the band intensity of siRNA increased in accordance with the amount of heparin (0 ~ 40 μg), harnessing the release of siRNA from the NGO-PAA in vitro. Furthermore, PAGE analysis after stepwise incubating RNase and heparin with siRNA/NGO-PAA complex showed intense siRNA band, supporting protection of siRNA from RNase-mediated degradation in the presence of NGO-PAA. In contrast, free siRNA was completely degraded by RNase and thus no tangible siRNA band was observed (Fig. 2.10c). Steric hindrance and low electrostatic interaction provided by NGO-PAA might contribute to the barrier for nuclease accessibility to siRNA/NGO-PAA complex thus, successful protection of siRNA was achieved. This result indicated the NGO-PAA serve as an efficient siRNA delivery carrier because it effectively condenses with siRNA and

protects the complexed siRNA from enzymatic cleavage mediated by RNase.

DOX, an anthracycline antibiotic, has been widely applied in cancer and leukemia treatment through inhibition of replicating DNA via intercalation into supercoiled DNA thus, inhibiting the progression of the enzyme topoisomerase II and the synthesis of nucleic acids within cells.^{64,65} However, DOX possessing aromatic structure cause low solubility in aqueous solution. We hypothesized that NGO–PAA is a suitable carrier for DOX because of the large surface area with aromatic carbon structure of NGO–PAA which attribute to the strong π – π interaction between the aromatic structure of DOX and basal sp^2 carbon domain of NGO–PAA as well as hydrogen bonding between their functional groups.^{66–68} We next prepared the DOX and NGO–PAA complex (DOX/NGO–PAA) by incubating DOX with NGO–PAA in a buffered solution (pH 8.0) for 2 days and further filtration. The successful loading of DOX on NGO–PAA was demonstrated by the UV–vis–NIR absorbance spectra of the samples (Fig. 2.11a). After loading DOX, DOX/NGO–PAA displayed characteristic DOX

absorption peaks at 490 nm but the NGO–PAA themselves did not show the characteristic absorption peaks and the shift of the characteristic peak from 491 nm in DOX to 508 nm in DOX/NGO–PAA. Moreover, the fluorescence of DOX was completely quenched in the presence of NGO–PAA at 590 nm wavelength ($\lambda_{\text{ex}}=547$ nm) due to the close proximity of fluorescence drug and NGO–PAA by comparing the fluorescence spectra at the same concentration of DOX (Fig. 2.12), suggesting that DOX molecules were successfully adsorbed on the surface of NGO–PAA. These optical characteristics suggested that DOX was successfully loaded to NGO–PAA and quantitative measurement showed ~82.5 wt% highly loading capacity of NGO–PAA for DOX molecule compared to other nanocarriers including carbon nanomaterials.^{67,69–71}

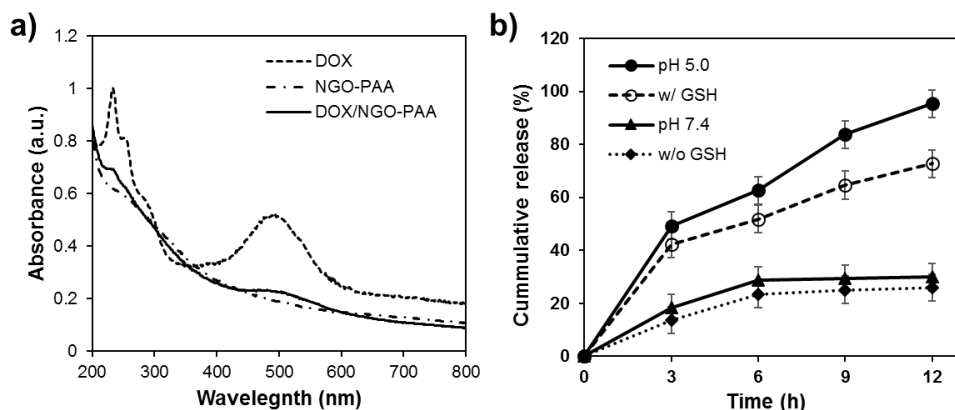


Figure 2.11. a) UV-vis-NIR absorption spectrum of DOX, NGO-PAA, and DOX/NGO-PAA. The characteristic peak of DOX at 490 nm revealed in DOX and DOX/NGO-PAA. b) Real-time monitoring of fluorescence of DOX ($\lambda_{em}=590$ nm) corresponding to cumulative release at various conditions. The released DOX from the NGO-PAA recovered fluorescence gradually in acidic condition and reductive condition.

Next, the release behavior of DOX was researched by monitoring the fluorescence of DOX at 590 nm wavelength ($\lambda_{ex}=547$ nm) at the pH value of 7.4 and 5.0 as well as reductive conditions over time. As shown in Fig. 2.11b, release of DOX upon GSH (10 mM) and acidic condition (pH 5.0) indicated 72.6% and 95.2% for 12 h respectively. It was

found that GSH, a reducing agent in the cell cytoplasm, induced release of absorbed DOX by the disruption of non-covalent hydrophobic interactions and π - π stacking of the aromatic regions of both DOX and GO sheet.^{72,73} And the protonation of NH_2 groups of DOX which become hydrophilic thus contributed to release itself due to the decrease of the interaction between DOX and the functional groups of nanoparticles such as hydrogen bonding interaction at the low pH condition.^{74,75} Therefore, it was expected that drug release in cells could be induced by a combination of multiple stimuli such as acidic pH and the presence of GSH environment.

Based on the performance of NGO-PAA as a drug and gene carrier in vitro, we sequentially prepared DOX/siRNA/NGO-PAA complex for combinational therapy following the mentioned method. DLS measurement indicated the increase hydrodynamic diameter from NGO-PAA (186.5 ± 9.8 nm) to DOX/NGO-PAA (212.1 ± 7.4 nm) and DOX/siRNA/NGO-PAA (245.8 ± 9.1 nm), respectively. (Fig. 2.9c and 2.9d) Moreover, Zeta-potential of NGO-PAA, DOX/NGO-PAA, and DOX/siRNA/NGO-PAA showed $33.5 \pm$

5.4 mV, 37.8 ± 6.1 mV, and 8.3 ± 4.8 mV, respectively (Fig. 2.9e). The increase in diameter and decrease in zeta potential after DOX and siRNA condensing to NGO-PAA suggested the successful formation of DOX/siRNA/NGO-PAA complex and the resulting positively charge of the complex implied the possibility of favorable interaction with the negatively charged cell surface to promote its cellular uptake process.

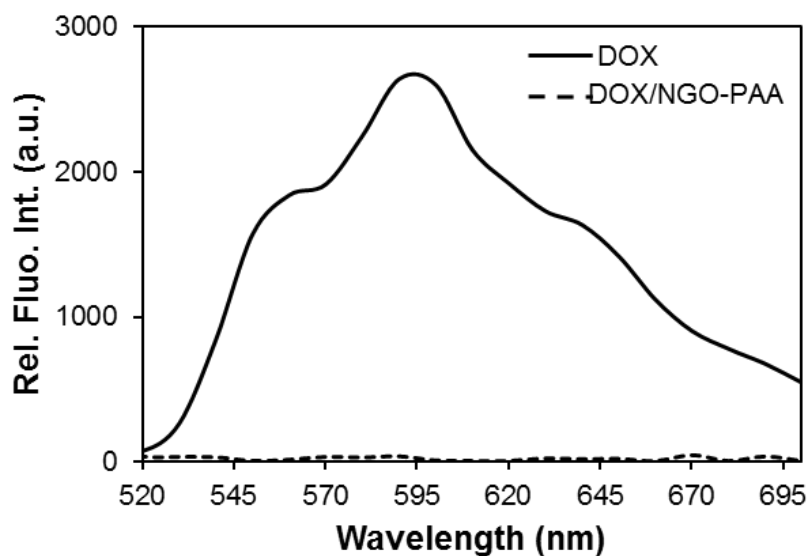


Figure 2.12. Fluorescence quenching test. The fluorescence of DOX at 590 nm ($\lambda_{\text{ex}}=547$ nm) was quenched by NGO-PAA through $\pi - \pi$ interaction.

Prior to investigating intracellular study, we estimated colloidal stability and cytotoxicity of NGO-PAA in physiological conditions and mammalian cell line, Huh7 cells possessing replicating HCV subgenomic RNA (Huh7-rep), respectively.⁷⁶ Several approaches have been introduced stabilized polymer such as polyethylene glycol to improve the stability of two-dimension materials including GO because those dispersed in deionized water that causes aggregation, precipitation, and cell toxicity.⁷⁷⁻⁷⁹ In addition, it is well known that cationic polymer used in drug delivery carrier induced cytotoxicity due to cell damage from disruption of the cell membrane, thus the application of those nanoparticles in the medical field have been restricted.⁸⁰ In this study, Fig. 2.13 showed that highly stability of NGO-PAA maintained for 24 h in saline and serum condition without noticeable aggregation. Moreover, more than 85% of cells were viable under the concentration ranges of NGO-PAA (0 ~ 50 $\mu\text{g/mL}$) (Fig. 2.14). NGO-PAA need no further polymer conjugation to improve stability and cell viability probably due to the density and degree of freedom of amine groups of PAA in

NGO–PAA might attribute to reduce cytotoxicity through the decrease of exposing amine groups to cell membrane directly.^{81,82} We used maximum concentration of NGO–PAA of 50 $\mu\text{g}/\text{mL}$ throughout the present study, which ensures more than 85% of cell viability.

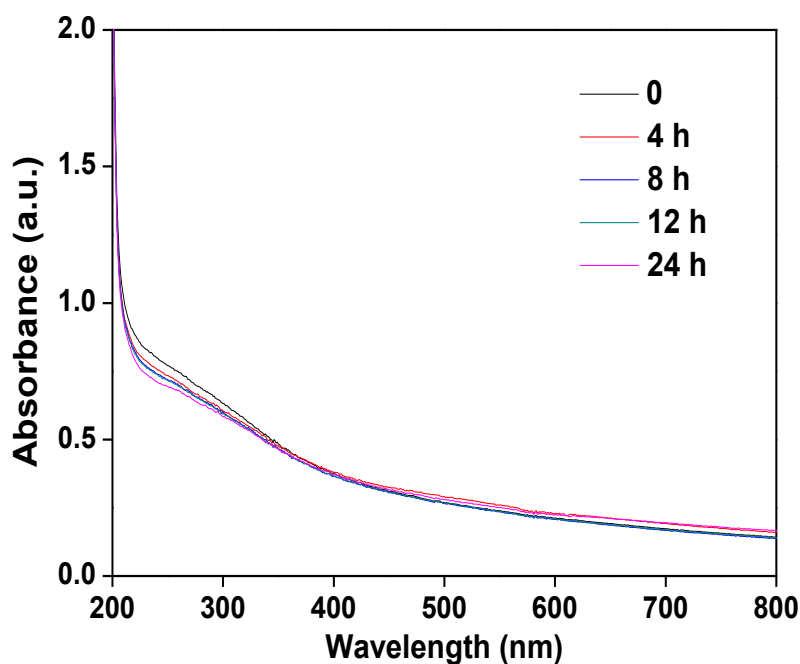


Figure 2.13. UV–vis–NIR spectrum for stability test of NGO–PAA in a buffered solution with serum over time.

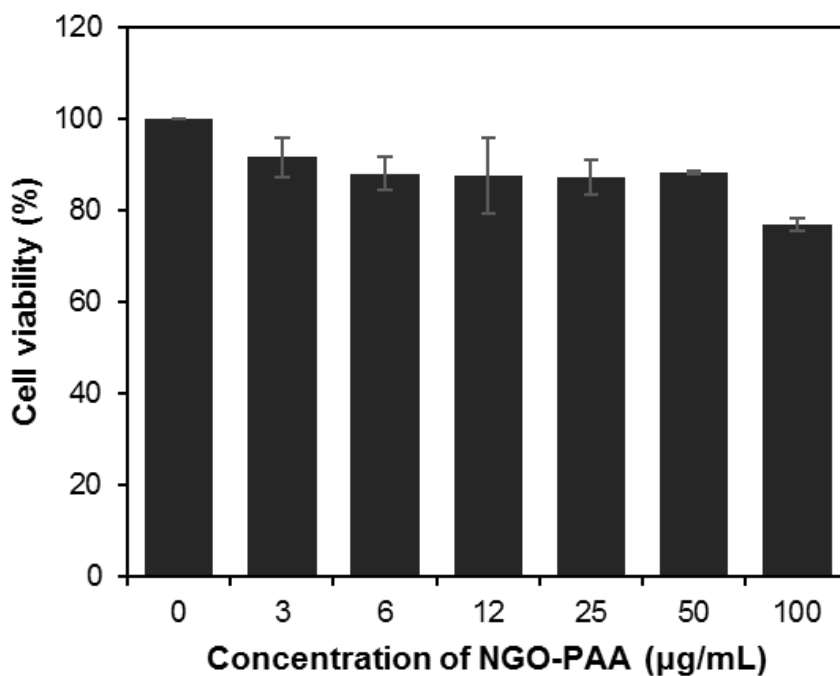


Figure 2.14. The biocompatibility of NGO–PAA was confirmed by using CCK–8 cell proliferation assay kit. NGO–PAA shows high cell viability over 90% after incubation with Huh7–rep cells for 12 h. The experiment was carried out in three times.

Encouraged by highly colloidal stability and cell viability of NGO–PAA, we next investigated the cellular uptake and the intracellular localization of DOX and siRNA using NGO–PAA carrier. To evaluate the carrier–mediated enhancing intracellular accumulation of antibiotic drug, cellular

internalization of DOX/NGO–PAA was first examined by using fluorescence microscopy in parallel with free DOX using Huh7–rep cells. The cells were incubated with both materials for 24 h to get high internalization degree. Fig. 2.15a showed the fluorescence image of Huh7–rep cells over time up to 24 h. Both cells treated with free DOX and DOX/NGO–PAA presented red fluorescence of DOX in the cytoplasm. In the case of DOX/NGO–PAA treated cells, however, the intense red fluorescence of DOX was accumulated in cytoplasm and nucleus area in 4 h. Although the morphology of the cells was affected for a longer time of incubation up to 24 h, the fluorescence intensity increased further in the nucleus and whole cells confirms the enhanced nuclear penetration of DOX through NGO–PAA mediated cellular internalization. To investigate more precise enhancing the effect of cellular uptake and the amount of released DOX, we carried out flow cytometric analysis using whole cells uptaken particles and reflected red fluorescence of DOX. Fig. 2.15b showed the significant shift of the cell population histogram correlated with fluorescence signal at various times compared to

untreated control cells. Moreover, as shown in Fig. 2.15c, bar-graph which present mean fluorescence intensity of DOX corresponding histogram result showed significant increase 4.5-fold in DOX/NGO-PAA treated cells compared to free DOX-treated one. These result revealed that without a longer incubation time, DOX could penetrate the cell nucleus, which enhances the antibiotic effect with the little medication. Taken together, it is indicated that the cellular uptake of DOX for Huh7-rep cell incubated with DOX/NGO-PAA is remarkably higher than those with free DOX.

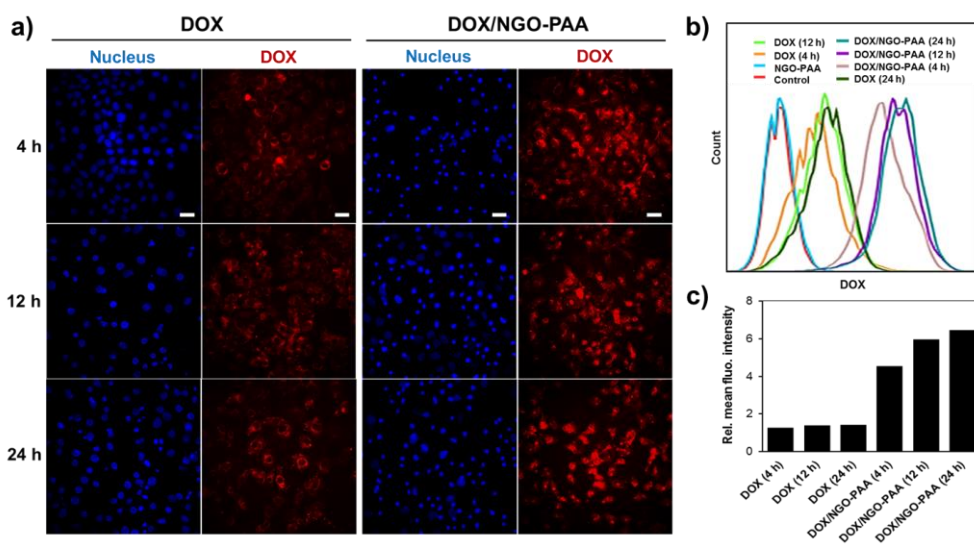


Figure 2.15. a) Fluorescence image of Huh7–rep cells treated with DOX and DOX/NGO–PAA over time. Blue fluorescence signals from nucleus stained with Hoechst 33342 were observed at 461 nm ($\lambda_{ex}=365$ nm) and red fluorescence of DOX appeared at 590 nm ($\lambda_{ex}=547$ nm) in the cells. Red fluorescence of DOX were strongly intensified in nucleus and whole celled treated with DOX/NGA–PAA compared to that treated with DOX itself. Scale bar is 50 μ m. b) Cell population histogram correlated with fluorescence intensity of DOX uptaken to the cells over time by flow cytometric analysis. c) Bar–graph with relative fluorescence intensity corresponding to histogram of each cell treated with DOX and DOX/NGO–PAA.

We next further investigated the intracellular localization of DOX and siRNA from NGO-PAA after treatment of DOX/siRNA/NGO-PAA complex to Huh7-rep cells. Not only the pinkish purple fluorescence that merged from DOX (red) and Hoechst (blue) was observed in nucleus but the noticeable green fluorescence of siRNA was monitored in the cytoplasm of NGO-PAA mediated both cargoes delivered cells (Fig. 2.16). It was reported by several research groups that modified GO sheets enter cells through the endocytosis mechanism such as clathrin-mediated endocytosis and phagocytosis.⁸³⁻⁸⁴ However, increasing lateral size of GO sheet with functionalization was unfavorable to cellular uptake. Thus, less than 10 nm-sized carbon materials have been applied in nuclear-targeting drug delivery system through caveolae-mediated endocytosis.^{85,86} But it remains high cytotoxicity due to reactive oxygen species generation and thus, induces systemic apoptosis signal pathway after intracellular uptake process.^{87,88} In this study, it is likely that NGO-PAA was internalized to cells through PEI-mediated endocytosis which is one of the pathways that polysaccharide

possessing dense amine functional groups mediates the introduction to the cytoplasm.⁸⁹⁻⁹¹ Thus, the limitation of delivering of DOX with insoluble property could be improved and the release of siRNA was successfully accomplished by using NGO-PAA as a smart carrier of the higher amount of DOX as well as siRNA in the cytoplasm via its endocytosis mechanism, which facilitates the enhanced cytotoxicity of DOX and RNAi process.

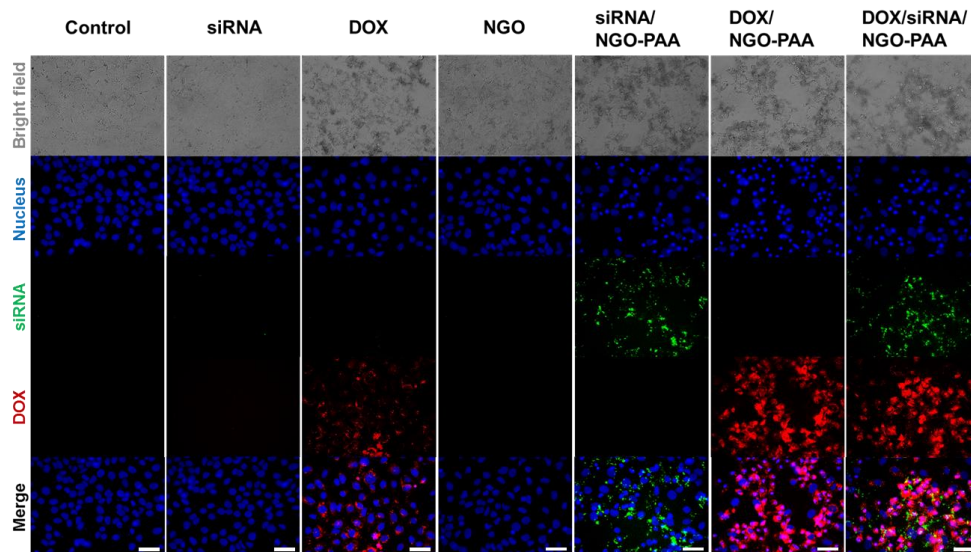


Figure 2.16. Intracellular uptake study. Bright field and fluorescence images of Huh7-rep cells treated with siRNA, DOX, and those complex form with NGO-PAA. Blue fluorescence signals from nucleus stained with Hoechst 33342 were observed at 461 nm ($\lambda_{ex}=365$ nm) in whole cells but green fluorescence signal from siRNA at 497 nm ($\lambda_{ex}=520$ nm) and red fluorescence of DOX at 547 nm ($\lambda_{ex}=590$ nm) was strongly appeared in NGO-PAA mediated siRNA, DOX-treated cells. Scale bar is 50 μ m.

Next, we evaluated down-regulation of HCV NS3 gene expression induced by siRNA targeting NS3 in vitro. HCV NS3 is requisite for HCV replication in human liver cells thus, direct inhibition of HCV NS3 protein expression through

mRNA degradation is a desirable approach as one of the strategies to treat HCV infection. Huh7-rep cells were incubated with 50 nM siRNA/NGO-PAA complex for 12 h, followed by removing media and further incubating with fresh serum-containing media for 48 h. The NS3 gene expression level was estimated by semi-quantitative RT-PCR. Band intensities of NS3 gene in gel electrophoresis were normalized with respect to the housekeeping gene, β -actin. As shown in Fig. 2.17a, RT-PCR results showed similarly efficient gene silencing of the NS3 gene by siRNA/NGO-PAA complexes down to 23.4% and by siRNA/Lipofectamine (LF) down to 42.1%. Moreover, LF itself induced critical cytotoxicity to NS3 expression down to 72.2%. Collectively, this data indicated that the siRNA/NGO-PAA complex induced more effective knockdown of HCV NS3 compared to the siRNA/LF at mRNA levels.

With the therapeutic effect of siRNA, the combined therapeutic cytotoxicity of DOX/siRNA/NGO-PAA (0.75 μ M of DOX, 50 nM of siRNA) was also investigated in Huh7-rep cells. The synergistic effect of DOX and siRNA was evaluated

by CCK-8 assay after 12 h of incubation. As shown in Fig. 2.17b, NGO-PAA based delivery of Dox and siRNA reduced cell viabilities down to 33.2% and 32.8% compared to the cells treated with free Dox and siRNA without NGO-PAA showed the cell viability to 59.5% and 102.1%, respectively. The NGO-PAA, which had no cytotoxicity itself (103.3%), exhibited the notable decrease cell viability under DOX/siRNA delivery (10.9%), indicating that NGO-PAA mediated both DOX and siRNA combination delivery shows enhanced therapeutic efficiency.

We further precisely investigated whether the simultaneous delivery of DOX and siRNA synergistic action can enhance the cytotoxicity and antibiotic chemotherapy. As shown in Fig. 2.17c, increasing the concentration of DOX reduced cell viability. However, the data showed that compared with free DOX or DOX/NGO, DOX-loaded siRNA/NGO-PAA complex exhibited enhanced cytotoxicity under same experimental concentration range. It was found that the IC_{50} (the concentration of drugs which kills 50% of the cells) value of the DOX/siRNA/NGO-PAA complex was

decreased 3.8-fold to 0.26 μM from 0.97 μM of free DOX. The results confirmed that antibiotic therapeutic effect of DOX can be significantly enhanced through synergistic RNAi-based efficient suppressing HCV NS3 expression and possibly detouring the effluent pump or exocytosis of the small drug due to the different intracellular uptake mechanism in comparison to free DOX. These results demonstrated that the NGO-PAA based co-delivery of DOX and siRNA was a promising strategy for treatment of HCV-related liver cancer cells.

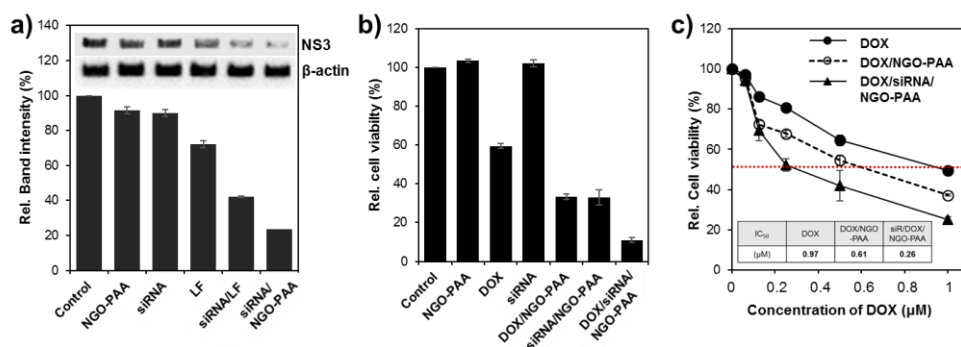


Figure 2.17. Quantitative evaluation of therapeutic efficacy of NGO-PAA based siRNA and DOX delivery in Huh7-rep cell line. a) Band images at mRNA expression level of HCV NS3 and β -actin by RT-PCR and the bar-graph of HCV NS3 normalized to β -actin by using Image J software. b) Relative cell viabilities corresponding to synergistic therapeutic efficacy. NGO-PAA mediated siRNA/DOX combination delivery shows remarkably enhanced therapeutic efficiency. c) Relative viabilities of Huh7-rep cells treated with various concentration of DOX measured by using CCK-8 cell viability assay kit. Inset table shows IC_{50} value (μ M) of DOX for therapeutic efficiency treated with DOX itself (0.97), DOX/NGO-PAA (0.61) and DOX/siRNA/NGO-PAA (0.26), respectively.

On the basis of the IC₅₀ values in vitro, we next investigated combinational therapeutic efficacy in vivo. Due to difficulties in developing the HCV hosted or infected animal model, several researchers have tried to develop HCV mouse model and validated viral RNA replication as well as the phenomena of tumor growth of severe combined immunodeficient syndrome (SCID) mouse implanted with Huh7 or Huh7.5 cells harboring subgenomic HCV replicon.⁹²⁻⁹⁴ In this study, we prepared Huh7-rep xenograft mouse model using Balb/c nude mice with subcutaneous injection of 1×10⁶ Huh7-rep cells possessing epithelial-like tumorigenic ability followed by post-breeding for 6 weeks to make a tumor growth (~100 mm³). Prior to treatment of drugs to tumors, the replication of HCV RNA replicon in tumors of xenograft mice was validated by immunostaining an HCV NS3 with the monoclonal antibody against NS3. The tumor tissue was excised from each mouse and immunohistochemical and morphological analysis were conducted. As shown in Fig. 2.18a, the significant expression of viral protein NS3 was detected with green fluorescent signal and consistent

expression of the housekeeping gene, Glyceraldehyde 3-phosphate dehydrogenase (GAPDH), was also strongly observed with the red fluorescent signal in experimental mice, suggesting that producing HCV replication in xenograft was successfully developed.

To bypass the undesirable side effects such as cardiotoxicity drawn by systemically administration of drugs, the encapsulated drugs that consist of DOX and nanocarrier was locally introduced into the tumor site for good biocompatibility.⁹⁵ To evaluate the enhanced anti-tumor efficiency of drugs to HCV replicating tumor, the grown up tumors were treated with NGO-PAA, free DOX, free siRNA, DOX/NGO-PAA, DOX/siRNA/NGO-PAA (1 mg DOX/kg, 0.8 mg siRNA/kg, 100 μ L), and PBS by intratumoral injection three times (0, 5, and 10 days). The change of tumor volume was monitored for 16 days and measured by comparing to the initial tumor volume (Fig. 2.18b). With a statistically significant difference, the mice treated with DOX/siRNA/NGO-PAA presented remarkable suppression of tumor compared to those of other groups. However, the mice

treated with DOX/NGO-PAA showed slight inhibition of tumor growth in short-term of 10 days treatment and it have possessed the inadequacy to suppress the tumorigenic environment with viral RNA replication due to probably lack of anti-tumor effect with low dose of DOX (1 mg/kg) compared to conventional antibiotic drug dose (10 mg/kg) and drug resistance of cancer cells. RNAi-mediated HCV gene knockdown could trigger the decrease the production of a viral protein which promotes cellular proliferation and induces the hepatocellular carcinoma, suggesting the synergistic anti-tumor efficacy due to the individual pharmacological effect of DOX and siRNA.

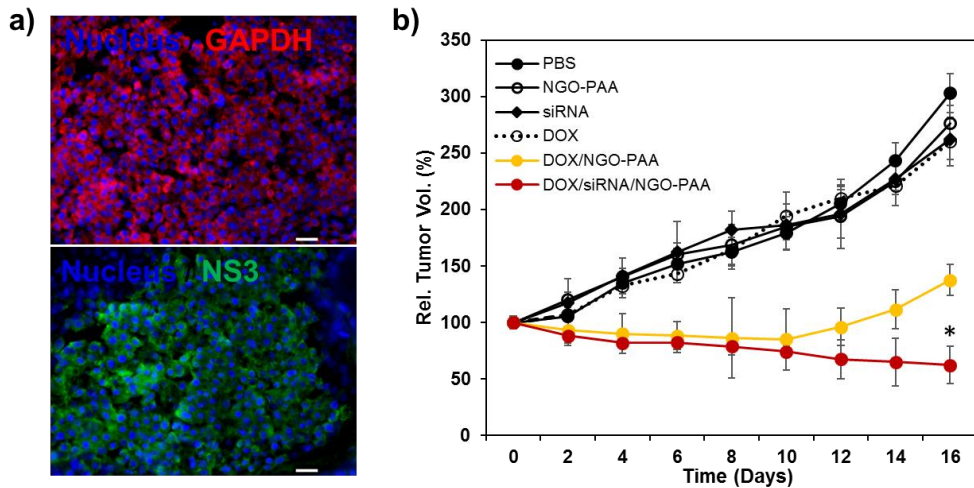


Figure 2.18. Anti-HCV therapeutic efficacy of NGO-PAA based siRNA and DOX co-delivery in a mouse model producing HCV replication. a) Immunostaining for GAPDH and HCV NS3 proteins in the xenograft at 6 weeks post Huh7-rep implanting. Blue: Nucleus, Red: GAPDH, Green: HCV NS3. Scale bar is 100 μ m. b) Relative tumor volumes measured over 16 days after the Huh7-rep tumor-bearing mice were treated with PBS, NGO-PAA, free siRNA, free DOX, DOX/NGO-PAA, and DOX/siRNA/NGO-PAA by intratumoral injection three times (0, 5, and 10 days). P-value was calculated by Student's t-test, * for $p < 0.05$, $n = 3$.

To investigate inhibition of HCV NS3 expression induced by RNAi, the sectioned tissue excised from each mouse was evaluated with visualization by using fluorescence

conjugated-antibody applied immunohistochemistry. As shown in Fig. 2.19, fluorescence images showed a notable decrease in green fluorescence of HCV NS3 in sectioned tissue treated with DOX/siRNA/NGO-PAA complex compared to those treated with NGO-PAA, free siRNA, free DOX, and PBS only, suggesting the successful suppression of HCV NS3 expression via RNAi in mouse xenograft model. NGO-PAA did not lead decrease of tumor volume including any deleterious effect, supporting the highly biocompatible materials in accordance with improved stability as we mentioned. Moreover, histological study with infiltrated and stained tumor section showed highly pleomorphic nuclei without any certain toxicological necrosis in major organs (i.e., liver, spleen) from the mice treated with DOX/siRNA/NGO-PAA compared to PBS (Fig. 2.20)

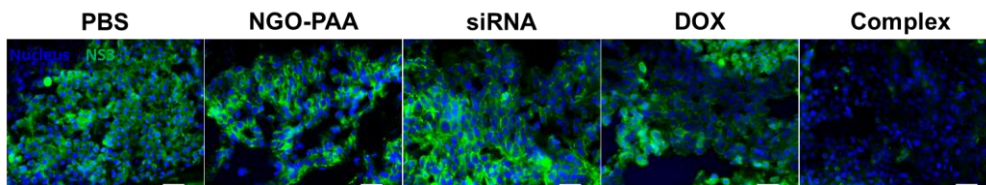


Figure 2.19. Immunostaining for HCV NS3 proteins in the xenograft treated with NGO-PAA, siRNA, DOX, DOX/siRNA/NGO-PAA (Complex), and PBS at 6 weeks post Huh7-rep implanting Blue: Nucleus, Green: HCV NS3. Scale bar is 100 μ m.

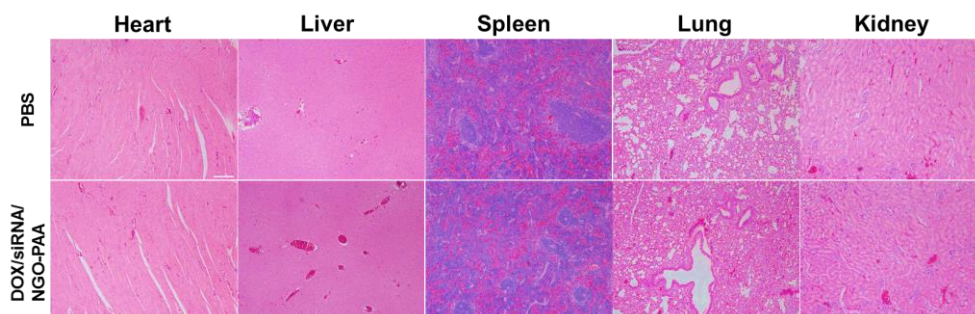


Figure 2.20. Hematoxylin and eosin (H&E) stained images of major organs excised from the mouse after treatment of PBS and DOX/siRNA/NGO-PAA complex. No notable systemic toxicity from major organs in case of DOX/siRNA/NGO-PAA was observed compared to those of PBS as a control at 16 days post treatment.

Collectively, the present NGO–PAA mediated DOX and siRNA co-delivery system demonstrated high anti-tumor efficiency through the enhanced nuclear penetration of DOX through NGO–PAA mediated intracellular accumulation and combinational RNAi-based HCV gene silencing more than 10-fold lower effect dose of DOX compare to conventional dose in vivo.^{96–98}.

2.2.4. Conclusion

In summary, we developed a novel theranostic platform for enhancing antibiotic drug accumulation in the nucleus of cancer cells and synergistic therapeutic system via combinational release and function of drugs and gene in the cells. In this study, we successfully demonstrated improved therapeutic efficacy with the low dose of the antibiotic drug than conventional dose through the NGO-PAA mediated intracellular accumulation and combinational down-regulation of target HCV NS3 gene via RNAi activity. The present NGO-PAA was prepared with the simple synthetic process, and it possessed excellent biocompatibility, multi-drug loading capability as well as improved physiological stability and cell viability without the introduction of the stabilizing agent. Moreover, cost-effective and simple noninfectious in vivo mouse model system possessing HCV replication produced in a short time compared to those of infectious liver can be applied to support high-throughput screen mode of anti-HCV candidates as a drug or gene, thus more hit compounds can be rapidly assessed and produced in vivo. In our previous study,

we successfully discovered and validated several HCV helicase inhibitors from the 10,000 small molecule library using GO-based helicase assay in vitro.^{99,100} We expect that the NGO-PAA platform can be used to evaluate anti-HCV activities of inhibitors for the next generation HCV treatment. We believe that the present NGO-PAA could be a promising multimodal therapeutic platform due to multiple functionalities with the simple synthetic process in near future.

2.2.5. References

1. Appleyard, G. *Br. Med. Bull.* **1967**, 23, 114.
2. Diana, G. D.; Pancic, F. *Angew. Chem. Int. Ed.* **1976**, 15, 410.
3. Agarwal, R.; Kaye, S. B. *Nat. Rev. Cancer* **2003**, 3, 502.
4. Chabner, B. A.; Roberts, T. G. *Nat. Rev. Cancer* **2005**, 5, 65.
5. Chen, A. M.; Zhang, M.; Wei, D.; Stueber, D.; Taratula, O.; Minko, T.; He, H. *Small* **2009**, 5, 2673.
6. Meng, H.; Liong, M.; Xia, T.; Li, Z.; Ji, Z.; Zink, J. I.; Nel, A. E. *ACS Nano* **2010**, 4, 4539.
7. Wong, P. P.; Demircioglu, F.; Ghazaly, E.; Alrawashdeh, W.; Stratford, M. R.; Scudamore, C. L.; Cereser, B.; Crnogorac-Jurcevic, T.; McDonald, S.; Elia, G.; Hagemann, T.; Kocher, H. M.; Hodivala-Dilke, K. M. *Cancer Cell* **2015**, 27, 123.
8. Chen, X.; Qiu, Y. K.; Owh, C.; Loh, X. J.; Wu, Y. L. *Nanoscale* **2016**, 8, 18876.
9. Lake, R. A.; Robinson, B, W. *Nat. Rev. Cancer* **2005**, 5, 397.
10. Woodcock, J.; Griffin, J. P.; Behrman, R. E. *N. Engl. J. Med.* **2011**, 364, 985.
11. Hu, C. M.; Zhang, L. *Pharmacol.* **2012**, 83, 1104.
12. Shi, S.; Yao, W.; Xu, J.; Long, J.; Liu, C.; Yu, X. *Cancer Lett.* **2012**, 317, 127.
13. Fire, A.; Xu, S. Q.; Montgomery, M. K.; Kostas, S. A.; Driver, S. E.; Mello, C. C. *Nature* **1998**, 391, 806.
14. Hamilton, A. J.; Baulcombe, D. C. *Science* **1999**, 286, 950.

15. Elbashir, S. M.; Harborth, J.; Lendeckel, W.; Yalcin, A.; Weber, K.; Tuschl, T. *Nature* **2001**, 411, 494.
16. Nykanen, A.; Haley, B.; Zamore, P. D. *Cell* **2001**, 107, 309.
17. Martinez, J.; Patkaniowska, A.; Urlaub, H.; Luhrmann, R.; Tuschl, T. *Cell* **2002**, 110, 563.
18. Dorsett, T.; Tuschl, T. *Nat. Rev. Drug Discov.* **2004**, 3, 318.
19. Bumcrot, D.; Manoharan, M.; Koteliansky, V.; Sah, D. W. *Nat. Chem. Biol.* **2006**, 2, 711.
20. Jeffers, L. *J. Natl. Med. Assoc.* **2000**, 92, 369.
21. Brody, H. *Nature* **2011**, 474, S1.
22. Kohli, A.; Shaffer, A.; Sherman, A.; Kottlilil, S. *JAMA.* **2014**, 312, 631.
23. Webster, D. P.; Klenerman, P.; Dusheiko, G. M. *Lancet* **2015**, 385, 1124.
24. Moradpour, D.; Grakoui, A.; Manns, M. P. *J. Hepatol.* **2016**, 65, S143.
25. De Francesco, R.; Migliaccio, G. *Nature* **2005**, 436, 953.
26. Meiyanto, E.; Hermawan, A.; Anindyajati. *Asian Pac. J. Cancer Prev.* **2012**, 13, 427.
27. Lawitz, E.; Mangia, A.; Wyles, D.; Rodriguez-Torres, M.; Hassanein, T.; Gordon, S. C.; Schultz, M.; Davis, M. N.; Kayali, Z.; Reddy, K. R.; Jacobson, I. M.; Kowdley, K. V.; Nyberg, L.; Subramanian, G. M.; Hyland, R. H.; Arterburn, S.; Jiang, D.; McNally, J.; Brainard, D.; Symonds, W. T.; McHutchison, J. G.; Sheikh, A. M.; Younossi, Z.; Gane, E. J. *N. Engl. J. Med.* **2013**, 368, 1878.

28. Kieffer, T. L.; George, S. *Curr. Opin. Virol.* **2014**, 8, 16.
29. Aslam, M. S.; Naveed, S.; Ahmed, A.; Abbas, Z.; Gull, I.; Athar, M. A. *J. Cancer Therapy* **2014**, 5, 817.
30. Pungpapong, S.; Aqel, B.; Leise, M.; Werner, K. T.; Murphy, J. L.; Henry, T. M.; Ryland, K.; Chervenak, A. E.; Watt, K. D.; Vargas, H. E.; Keaveny, A. P. *Hepatology* **2015**, 61, 1880.
31. Zavitsanos, X.; Hatzakis, A.; Kaklamani, E.; Tzonou, A.; Toupadaki, N.; Broeksma, C.; Chrispeels, J.; Troonen, H.; Hadziyannis, S.; Hsieh, C. C.; Alter, H.; Trichopoulos, D. *Cancer Res.* **1992**, 52, 5364.
32. Di Bisceglie, A. M. *Hepatology* **1997**, 26, 34S.
33. Butt, S.; Idrees, M.; Rehman, I. U.; Ali, L.; Hussain, A.; Ali, M.; Ahmed, N.; Saleem, S.; Fayyaz, M. *Genet. Vaccines Ther.* **2011**, 9, 12.
34. Selimovic, D.; El-Khattouti, A.; Ghozlan, H.; Haikel, Y.; Abdelkader, O.; Hassan, M. *World J. Hepatol.* **2012**, 4, 342.
35. Goossens, N.; Hoshida, Y. *Clin. Mol. Hepatol.* **2015**, 21, 105.
36. Liu, Z.; Robinson, J. T.; Sun, X.; Dai, H. *J. Am. Soc. Chem.* **2008**, 130, 10876.
37. Loh, K. P.; Bao, Q.; Eda, G.; Chhowalla, M. *Nat. Chem.* **2010**, 2, 1015.
38. Wang, Y.; Li, Z.; Wang, J.; Li, J.; Lin, Y. *Trends Biotechnol.* **2011**, 29, 205.
39. Shen, He.; Zhang, L.; Liu, M.; Zhang, Z. *Theranostics* **2012**, 2, 283.

40. Morales–Narváez, E.; Merkoçi, A. *Adv. Mater.* **2012**, *24*, 3298.
41. Liu, Y.; Dong, X.; Chen, P. *Chem. Soc. Rev.* **2012**, *41*, 2283.
42. Chung, C.; Kim, Y. K.; Shin, D.; Ryoo, S. R.; Hong, B. H.; Min, D. H. *Acc. Chem. Res.* **2013**, *46*, 2211.
43. Feng, L.; Wu, L.; Qu, X. *Adv. Mater.* **2013**, *25*, 168.
44. Bitounis, D.; Ali–Boucetta, H.; Hong, B. H.; Min, D. H.; Kostarelos, K. *Adv. Mater.* **2013**, *25*, 2258.
45. Krishna, K. V.; Ménard–Moyon, C.; Verma, S.; Bianco, A. *Nanomedicine* **2013**, *8*, 1669.
46. Kim, S.; Ryoo, S. R.; Na, H. K.; Kim, Y. K.; Choi, B. S.; Lee, Y.; Kim, D. E.; Min, D. H. *Chem. Commun.* **2013**, *49*, 8241.
47. Dong, H.; Dong, C.; Ren, T.; Li, Y.; Shi, D. *J. Biomed. Nanotechnol.* **2014**, *10*, 2086.
48. Yang, K.; Feng, L.; Liu, Z. *Expert Opin. Drug Deliv.* **2015**, *12*, 601.
49. Choi, H. Y.; Lee, T. J.; Yang, G. M.; Oh, J.; Won, J.; Han, J.; Jeong, G. J.; Kim, J.; Kim, J. H.; Kim, B. S.; Cho, S. G. *J. Control. Release* **2016**, *235*, 222.
50. Lee, J. S.; Kim, S.; Na, H. K.; Min, D. H. *Adv. Healthc. Mater.* **2016**, *5*, 2386.
51. Shim, G.; Kim, M. G.; Park, J. Y.; Oh, Y. K. *Adv. Drug. Deliv. Rev.* **2016**, *105*(Pt B), 205.
52. Lee, J.; Kim, J.; Kim, S.; Min, D. H. *Adv. Drug. Deliv. Rev.* **2016**, *105*(Pt B), 275.
53. Alba, M.; Formentín, P.; Ferré–Borrull, J.; Pallarès, J.; Marsa, L. F. *Nanoscale Res. Lett.* **2014**, *9*, 411.

54. Hummers, W. S. Jr.; Offeman, R. E. *J. Am. Chem. Soc.* **1958**, 80, 1339.
55. Park, S.; Dikin, D. A.; Nguyen, S. T.; Ruoff, R. S. *J. Phys. Chem. C* **2009**, 113, 15801.
56. Yang, H.; Shan, C.; Li, F.; Han, D.; Zhang, Q.; Niu, L.; *Chem. Commun.* **2009**, 3880.
57. Lai, L.; Chen, L.; Zhan, D.; Sun, L.; Liu, J.; Lim, S. H.; Poh, C. K.; Shen, Z.; Lin, J. *Carbon* **2011**, 49, 3250.
58. Yu, P.; Wen, X. M.; Toh, Y. R.; Tang, J. *J. Phys. Chem. C* **2012**, 116, 25552.
59. Kim, Y. K.; Min, D. H. *Langmuir* **2012**, 28, 4453.
60. Meylan, E.; Curran, J.; Hofmann, K.; Moradpour, D.; Binder, M.; Bartenschlager, R.; Tschopp, J. *Nature* **2005**, 437, 1167.
61. Sakamoto, N.; Tanabe, Y.; Yokota, T.; Satoh, K.; Sekine-Osajima, Y.; Nakagawa, M.; Itsui, Y.; Tasaka, M.; Sakurai, Y.; Cheng-Hsin, C.; Yano, M.; Ohkoshi, S.; Aoyagi, Y.; Maekawa, S.; Enomoto, N.; Ko-hara, M.; Watanabe, M. *J. Gastroenterol Hepatol.* **2008**, 23, 1437.
62. Halfon, P.; Locarnini, S. *J. Hepatol.* **2011**, 55, 192.
63. Na, H. K.; Kim, M. H.; Park, K.; Ryoo, S. R.; Lee, K. E.; Jeon, H.; Ryoo, R.; Hyeon, C.; Min, D. H. *Small* **2012**, 8, 1752.
64. Kik, K.; Wasowska-Lukawska, M.; Oszczapowicz, I.; Szmigiero, L. *Anticancer Res.* **2009**, 29, 1429.
65. Thorn, C. F.; Oshiro, C.; Marsh, S.; Hernandez-Boussard, T.; McLeod, H.; Klein, T. E.; Altman, R. B. *Pharmacogenet*

- Genomics* **2011**, 21, 440.
66. Yang, X.; Zhang, X.; Liu, Z.; Ma, Y.; Huang, Y.; Chen, Y. *J. Phys. Chem. C* **2008**, 112, 17554.
67. Zhou, T.; Zhou, X.; Xing, D. *Biomaterials* **2014**, 35, 4185.
68. Wu, S.; Zhao, X.; Li, Y.; Du, Q.; Sun, J.; Wang, Y.; Wang, X.; Xia, Y.; Wang, Z.; Xia, L. *Materials* **2013**, 6, 2026.
69. Chung, J. W.; Lee, K. A.; Neikirk, C.; Nelson, C. M.; Priestley, R. D. *Small* **2012**, 8, 1693.
70. Wei, G.; Yan, M.; Dong, R.; Wang, D.; Zhou, X.; Chen, J.; Hao, J. *Chemistry* **2012**, 18, 14708.
71. Lee, Y. K.; Choi, J.; Wang, W.; Lee, S.; Nam, T. H.; Choi, W. S.; Kim, C. J.; Lee, J. K.; Kim, S. H.; Kang, S. S.; Khang, D. *ACS Nano* **2013**, 7, 8484.
72. Dembereldorj, U.; Kim, M.; Kim, S.; Ganbold, E. O.; Lee, S. Y.; Joo, S. W. *J. Mater. Chem.* **2012**, 22, 23845.
73. Jang, H.; Min, D. H. *ACS Nano* **2015**, 9, 2696.
74. Wang, Y.; Wang, K.; Zhao, J.; Liu, X.; Bu, J.; Yan, X.; Huang, R. Wang Y1, Wang K, Zhao J, Liu X, Bu J, Yan X, Huang R. *J. Am. Soc. Chem.* **2013**, 135, 4799.
75. Minati, L.; Antonini, V.; Serra, M. D.; Speranza, G.; Enrichi, F. Riello, P. *Microporous and Mesoporous Materials* **2013**, 180, 86.
76. Lohmann, V.; Korner, F.; Koch, J.; Herian, U.; Theilmann, L.; Bartenschlager, R. *Science* **1999**, 285, 110.
77. Chu, Z.; Zhang, S.; Zhang, B.; Zhang, C.; Fang, C. Y.; Rehor, I.; Cigler, P.; Chang, H. C.; Lin, G.; Liu, R.; Li, Q. *Sci. Rep.* **2014**, 4, 4495.

78. Teimouri, M.; Nia, A. H.; Abnous, K.; Eshghi, H.; Ramezani, M. *Plasmid* **2016**, 84–85, 51.
79. Kiew, S. F.; Kiew, L. V.; Lee, H. B.; Imae, T.; Chung, L. Y. *J. Control. Release* **2016**, 226, 217.
80. Lv, H. T.; Zhang, S. B.; Wang, B.; Cui, S. H.; Yan, J. *J. Control. Release* **2006**, 114, 100.
81. Hu, C.; Peng, Q.; Chen, F. J.; Zhong, Z. L.; Zhuo, R. X. *Bioconjugate Chem.* **2010**, 21, 836.
82. Nunes, A.; Amsharov, N.; Guo, C.; Van den Bossche, J.; Santhosh, P.; Karachalios, T. K.; Nitodas, S. F.; Burghard, M.; Kostarelos, K.; Al-Jamal, K. T. *Small* **2010**, 6, 2281.
83. Mu, Q.; Su, G.; Li, L.; Gilbertson, B. O.; Yu, L. H.; Zhang, Q.; Sun, Y. P.; Yan, B. *ACS Appl. Mater. Interfaces* **2012**, 4, 2259.
84. Zhou, B.; Huang, Y.; Yang, F.; Zheng, W.; Chen, T. *Chem. Asian J.* **2016**, 11, 1008.
85. Wang, C.; Wu, C.; Zhou, X.; Han, T.; Xin, X.; Wu, J.; Zhang, J.; Guo, S. *Sci. Rep.* **2013**, 3, 2852.
86. Wu, C.; Wang, C.; Han, T.; Zhou, X.; Guo, S.; Zhang, J. *Adv. Healthc. Mater* **2013**, 2, 1613.
87. Wang, D.; Zhu, L.; Chen, J. F.; Dai, L. *Nanoscale* **2015**, 7, 9894.
88. Qin, Y.; Zhou, Z. W.; Pan, S. T.; He, Z. X.; Zhang, X.; Qiu, J. X.; Duan, W.; Yang, T.; Zhou, S. F. *Toxicology* **2015**, 327, 62.
89. Dong, Y. Q.; Wang, R. X.; Li, H.; Shao, J. W.; Chi, Y. W.; Lin, X. M.; Chen, G. N. *Carbon* **2012**, 50, 2810.

90. Kim, H.; Namgung, R.; Singha, K.; Oh, I. K.; Kim, W. J. *Bioconjug. Chem.* **2011**, *22*, 2558.
91. Zhang, L.; Lu, Z.; Zhao, Q.; Huang, J.; Shen, H.; Zhang, Z. *Small* **2011**, *7*, 460.
92. Moon, J. S.; Lee, S. H.; Han, S. H.; Kim, E. J.; Cho, H.; Lee, W.; Kim, M. K.; Kim, T. E.; Park, H. J.; Rhee, J. K.; Kim, S. J.; Cho, S. W.; Han, S. H.; Oh, J. W. *Nanomedicine* **2016**, *12*, 1489.
93. Zhu, Q.; Oei, Y.; Mendel, D. B.; Garrett, E. N.; Patawaran, M. B.; Hollenbach, P. W.; Aukerman, S. L.; Weiner, A. J. *Agents Chemother.* **2006**, *50*, 3260.
94. Zhu, Q.; Weiner, A. J. *Methods Mol. Biol.* **2009**, *511*, 323.
95. Xue, X.; Zhao, Y.; Dai, L.; Zhang, X.; Hao, X.; Zhang, C.; Huo, S.; Liu, J.; Liu, C.; Kumar, A.; Chen, W. Q.; Zou, G.; Liang, X. J. *Adv. Mater.* **2014**, *26*, 712.
96. Zhang, X.; Yang, C.; Zhou, J.; Huo, M. *Small* **2016**, *12*, 3578.
97. Sun, J. B.; Duan, J. H.; Dai, S. L.; Ren, J.; Zhang, Y. D.; Tian, J. S.; Li, Y. *Cancer Lett.* **2007**, *258*, 109.
98. Abu, A. K.; Graeser, R.; Fichtner, I.; Kratz, F. *Cancer Chemother. Pharmacol.* **2009**, *64*, 413.
99. Jang, H.; Kim, Y. K.; Kwon, H. M.; Yeo, W. S.; Kim, D. E.; Min, D. H. *Angew. Chem. Int. Ed.* **2010**, *49*, 5703.
100. Jang, H.; Ryoo, S. R.; Kim, Y. K.; Yoon, S.; Kim, H.; Han, S. W.; Choi, B. S.; Kim, D. E.; Min, D. H. *Angew. Chem. Int. Ed.* **2013**, *52*, 2340.

Chapter 3. *Therapeutic application of carbon nanodot*

3.1. Highly biocompatible carbon nanodots for simultaneous bioimaging and targeted photodynamic therapy in vitro and in vivo

3.1.1. Introduction

Biological labels that allow cellular imaging are receiving increasing attention in fluorescence microscopy, laser technology, and nanotechnology.¹ These labels are useful for tracking intracellular transport and biochemical phenomena in disease diagnosis and therapy.^{2,3} Although fluorescent organic dyes and genetically engineered proteins are still widely employed as promising luminescent biological labels, semiconducting nanoparticles (quantum dots) have garnered considerable attention because of their superior physical and chemical properties such as high photoluminescence and stability, together with tunable photophysical properties.⁴⁻⁶ Despite these notable advantages, the implementation of quantum dots to a broader clinical setting is still limited

because of their intrinsic toxicity and the potential environmental concerns associated with the heavy metals present in the quantum dots.^{7,8}

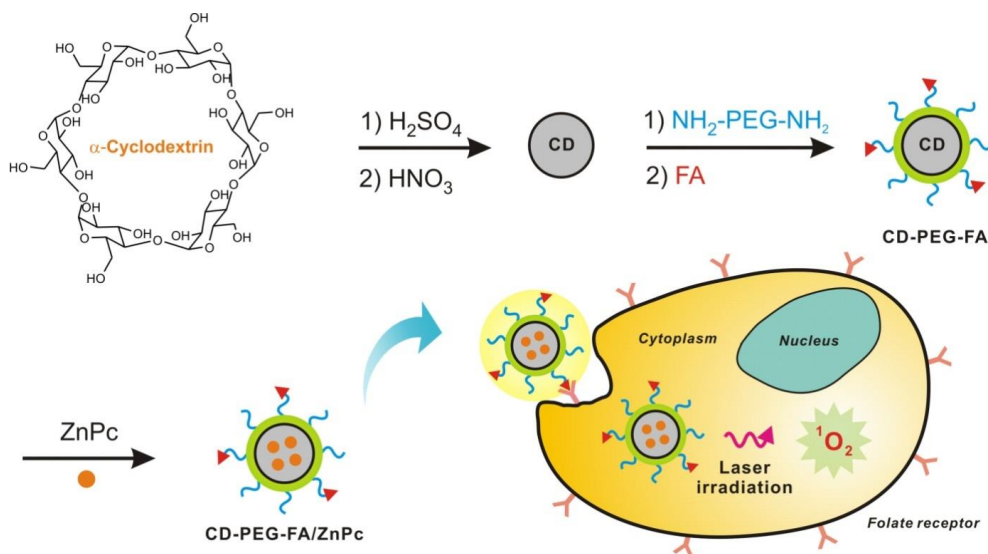
Longstanding interest in the search of benign alternatives has triggered the recent development of carbon nanoparticles (also known as C-dots, CDs) as a new class of biolabels by virtue of their biocompatibility, low toxicity, simple preparation and high stability while retaining the advantageous photophysical features of quantum dots.⁹⁻¹¹ CDs are generally composed of a mixed phase of sp^2 - and sp^3 -hybridized carbon nanostructures in the form of conjugated carbon clusters functionalized with oxygen-bearing functional groups.¹² Aside the strong fluorescence of CDs, their unique chemical structure allows the integration of active therapeutic molecules into the sp^2 carbon frame, and their surface functional groups enable further conjugation with other molecules such as biological affinity ligands. These unique characteristics make CDs ideal for simultaneous diagnosis and therapeutics (theranostics), which lead to advances in personalized medicine.¹³⁻¹⁵

Photodynamic therapy has been widely practiced as a promising non-invasive therapeutic modality for the treatment of cancer.¹⁶ In photodynamic therapy, photosensitizers (PSs) are irradiated by a specific wavelength of light, which triggers the generation of reactive oxygen species from intracellular oxygen that consequently induce cell death and necrosis of proximal tissues.^{17, 18} However, the limited solubility and poor selectivity of PSs often pose challenges, which inevitably require a carrier system to increase their aqueous solubility and enhance cellular internalization.^{19, 20} A number of approaches have been proposed to incorporate PSs into carriers such as liposomes, polymeric nanoparticles, gold nanoparticles, carbon nanotubes, and graphenes.²¹⁻²⁷ In addition, in order to increase the local concentration of PSs in cancer cells and avoid side effects, a common strategy is a direct conjugation of carriers with targeting ligands, such as monoclonal antibodies, proteins, peptides, steroids and folic acid.²⁸⁻³⁰ Although many of these carriers provide an effective means to increase the solubility and selectivity in aqueous media, it is still a challenging

endeavor to combine in vivo therapeutic, imaging, and targeting capabilities into a single carrier.

In this work, we report a novel design of highly biocompatible, fluorescent, folic acid (FA) functionalized CD as a carrier for zinc phthalocyanine (ZnPc) PS to achieve simultaneous biological imaging and targeted photodynamic therapy (Scheme 3.1). The biocompatible and tumor-targeting FA conjugated CD is designed to selectively accumulate in tumors and to activate ZnPc upon irradiation, which enhances the selectivity and the therapeutic efficacy of photodynamic therapy both in vitro and in vivo. Specifically, the CD is synthesized via the thermal decomposition of α -cyclodextrin as a sugar-derived molecular precursor. The surface of CD is subsequently passivated with poly(ethylene glycol) diamine (PEG) to enhance its fluorescence as well as to increase the biocompatibility.³¹ Surface-passivating ligands are known to play a pivotal role in increasing the fluorescence efficiency by decreasing the effective hole-trapping after generation of the exciton pair on the surface of CDs.³² The PEG-passivated CD (CD-PEG) is further modified with FA to

afford CD-PEG-FA for the targeted delivery to FA-positive cancer. Owing to its high affinity for cancerous cells and stability, FA is an ideal ligand for the folate receptors that are overexpressed in various types of human cancer cells.³³ In addition, as a second-generation PS, ZnPc possesses good cytotoxic efficiency.³⁴



Scheme 3.1. Schematic illustration of the preparation of carbon nanodots (CD) from α -cyclodextrin and targeted photodynamic therapy with folic acid functionalized carbon nanodots loaded with zinc phthalocyanine (CD-PEG-FA/ZnPc).

3.1.2. Materials and methods

Materials. α -Cyclodextrin, poly(ethylene glycol) diamine ($M_w = 1,500$ g/mol), folic acid, and zinc phthalocyanine (ZnPc) were purchased from Sigma-Aldrich. H_2SO_4 , HNO_3 , and K_2CO_3 were purchased from Daejung Chemical (Korea). Cell counting kit-8 (CCK-8) was purchased from Dojindo Laboratories (Japan). Live/dead® viability/cytotoxicity kit and singlet oxygen sensor green (SOSG) reagent were purchased from Molecular Probes (USA). 10X PBS phosphate buffered saline (PBS), Dulbecco's Modified Eagle's Medium (DMEM), and fetal bovine serum (FBS) were purchased from WELGENE (Korea).

Preparation of CDs. CDs were synthesized by dehydrating carbohydrates using concentrated sulfuric acid. In this case, 2.00 g of α -cyclodextrin was slowly added to 8 ml of H_2SO_4 , to which 5 ml of water was added to dissolve the α -cyclodextrin. The black solution was stirred vigorously for 1 h and then diluted with 40 ml of water. The solution was then centrifuged at 4,000 rpm for 10 min, and the supernatant was discarded. The precipitate was washed twice with distilled

water, re-suspended in 5 ml of water and 6 ml of HNO₃ (22.5 mM), and sonicated for 1 h. The resulting solution was refluxed under nitrogen for 12 h at 120 °C and then neutralized with K₂CO₃. After excess K₂CO₃ was removed, the CDs were subjected to extensive dialysis (SpectraPore MWCO 1,000) for 1 day to remove excess salts.

Surface passivation of CDs. To passivate the CDs, the solutions were diluted one to ten parts with distilled water and refluxed for 72 h at 120 °C with poly(ethylene glycol) diamine (PEG, 150 mM). After the reflux, each of the samples was subjected to extensive dialysis against water for 2 days. To prepare the FA-conjugated CD-PEG, FA (10 mM) and 1-ethyl-3-(3-dimethylaminopropyl)carbodiimide (EDC, 10 mM) were mixed in 1.0 mL of distilled water saturated with NaHCO₃, followed by incubation with CD-PEG (1.0 mg/ml) at room temperature for 18 h. The amount of conjugated FA in CD-PEG-FA, as estimated by measuring the UV/Vis absorbance, was 5.8 mg/ml-CD-PEG-FA. Then, the mixture was subjected to extensive dialysis against distilled water for purification for 2 days. For ZnPc loading to CD-PEG-FA, an

ethanolic solution of ZnPc (2.0 mg) was subjected to solvent evaporation prior to mixing with CD-PEG-FA (1.0 mg/ml). Then, the mixture was sonicated for 1 h on an ice bath and filtered through polyvinylidene difluoride (PVDF) syringe filters (0.2 μ m). The loading capacity of ZnPc to CD-PEG-FA, calculated from the standard curve of the UV-vis absorbance of ZnPc, was about 60 μ g of ZnPc per milligram of CD-PEG-FA.

Characterization. UV/vis spectrophotometer (UV-2550, Shimadzu) was used to record the absorbance for concentration control and comparison. Absorbance curves were compared to ascertain the similarity in concentration, after which the samples were adjusted for comparison. Fluorescence data were obtained by using a fluorometer (Agilent). Three-dimensional fluorescence spectrum of the CDs was obtained with an FP-8300 spectrofluorometer (JASCO). Transmission electron microscopy (TEM, JEM-2100, JEOL) and atomic force microscopy (AFM, Dimension 3100, Veeco) analyses were performed to investigate the size and morphology of the CDs. To confirm the functional groups

after passivation, XPS (K-alpha, Thermo Fisher) and FT-IR (Agilent) analyses were performed.

Photoluminescence lifetime measurement. The exciton lifetime was determined by the time-correlated single photon counting (TCSPC) technique. A computer-controlled diode laser with 375 nm wavelength, 54 ps pulse width, and 40 MHz repetition rate was used as an excitation source. The PL emission was spectrally resolved by using some collection optics and a monochromator (PicoQuant). The TCSPC module (PicoHarp 300E, PicoQuant) with a MCP-PMT (R3809U-5x series, Hamamatsu) was used for ultrafast detection. The total instrument response function (IRF) for PL decay was less than 30 ps, and the temporal time resolution was less than 10 ps. Deconvolution of the actual fluorescence decay and IRF was performed by using a fitting software (FlouFit, PicoQuant) to deduce the time constant associated with each exponential decay.

Fluorescence quenching test. To estimate the ZnPc loading to CD-PEG-FA, the fluorescence emission spectra of ZnPc (0.4 μ M) were obtained at an excitation wavelength of 650 nm with

or without CD-PEG-FA (1.0 mg/ml) by using a fluorometer (BioTek, USA).

Cell culture. HeLa cell lines were grown in DMEM containing 4.5 g/L D-glucose containing 10% FBS, 1% penicillin, and streptomycin, under an atmosphere of 5% CO₂ and at 37 °C.

Cellular toxicity test. To investigate the cytotoxicity of the CDs, we carried out the CCK-8 cell viability assay. HeLa cells (1×10^4 cells/well) were seeded in a 96-well plate for 24 h, and CDs were treated with the HeLa cells at varying concentrations (0-450 µg/mL) in serum-containing media. After 12 h incubation, the cells were carefully washed with 1X PBS; then, CCK-8 assay solution with serum-free media was added, incubation was carried out for 1 h, and the absorbance at 450 and 670 nm was measured by using a microplate reader (Molecular Devices, Inc., USA). To investigate the quantitative cell viability related to the photodynamic effect of CD-PEG-FA/ZnPc, HeLa cells (1×10^4 cells/well) were plated in a 96-well plate, incubated for 24 h, and incubated with various concentrations of CD-PEG-FA/ZnPc. After 12 h incubation, each well was irradiated with a 660-nm LED laser

(Mikwang Electronics, 30 mW/cm²) for 10 min, and then, the medium was replaced with a serum-containing medium. After further incubation for 12 h, the CCK-8 cell viability assay was performed as described above. All experiments were carried out in triplicate.

Cellular imaging. HeLa cells (1.2×10^5 cells/well) were seeded in a 4-well glass plate. After 24 h incubation, CDs derivatives were added to each well in a serum-free medium for 12 h. To confirm the effect of folate receptor-mediated cell uptake, free FA was excessively treated for 2 h prior to treating FA-conjugated CD derivatives. After 12 h incubation, the cells were carefully rinsed with 1X PBS, and the medium was replaced with a serum-containing medium. Cell images were obtained using a Ti inverted fluorescence microscope with a 10X (1.4 numerical aperture) objective (Olympus, Japan) and a Deltavision high-resolution microscope (GE Healthcare, Korea). To investigate the photodynamic effect, CD-PEG-FA/ZnPc (50 μ g/ml) with a serum-free medium was treated with HeLa cells (1.2×10^5 cells/well), which had been preincubated in a 12-well plate for 24 h. After the

medium exchange to a serum-containing medium, the cells were irradiated with a 660-nm fiber-coupled laser (LaserLab, Korea, 30 mW/cm²) for 10 min. After further 4 h incubation, each well was treated with Live/Dead assay reagent, based on the manufacturer's protocol. Then, fluorescence images of the cells were obtained by using a Ti inverted fluorescence microscope with a 10X objective.

Singlet oxygen detection. The SOSG reagent is highly selective to singlet oxygen (SO), and it emits strong green fluorescence in the presence of SO at 530 nm ($\lambda_{\text{ex}} = 504$ nm). SOSG (2.5 μM) dissolved in 2% methanol was added to ZnPc (3.8 μM) and CD-PEG-FA/ZnPc (1.0 mg/ml), and then, the generation of SO was induced by irradiation using a 660-nm LED (30 mW/cm²). After time-dependent irradiation, green fluorescence emission from the samples was observed at 530 nm by using a fluorometer (BioTek, USA).

In vivo targeting and biodistribution study. Male BALB/c-nude mice (6 weeks old) were purchased from Japan SLC, Inc. (Shizuoka, Japan). All animal experiments were carried out in compliance with the Institutional Animal Care and Use

Committees (IACUC) of Seoul National University. Tumor-bearing mice were prepared by subcutaneously injecting a suspension of the Hela cells (6×10^6 cells) in sterilized 1X PBS ($n = 4$). When the tumor size reached $\sim 70 \text{ mm}^3$, CD-PEG-FA/ZnPc, CD-PEG/ZnPc, and CD-PEG-FA in 1X PBS solution (0.5 mg ZnPc/kg) were injected into the tail veins of the tumor-bearing mice. As a control, one group of mice was treated with the same volume of 1X PBS. Fluorescent signals from the mice were obtained by using an optical molecular imaging system, Optix MX3 (GE Healthcare, Korea), at various time points. To examine the biodistribution of the injected ZnPc, major organs (heart, lung, liver, etc.) were collected into a petri-dish after 12 h injection and imaged.

In vivo photodynamic therapy. Tumor-bearing mice were first prepared in four groups ($n = 4$). When the tumor size reached $\sim 70 \text{ mm}^3$, the mice were treated with CD-PEG-FA/ZnPc, CD-PEG/ZnPc, and CD-PEG-FA in 1X PBS (0.5 mg ZnPc/kg) by intravenous injection. As a control, a group of mice was treated with the same volume of saline. The mice were segregated into 6 groups: (1) saline; (2) CD-PEG-FA

without irradiation; (3) CD-PEG/ZnPc without irradiation; (4) CD-PEG/ZnPc with irradiation; (5) CD-PEG-FA/ZnPc without irradiation; (6) CD-PEG-FA/ZnPc with irradiation. For the irradiated groups, 660-nm laser (0.3 W/cm^2 , 20 min) was used after 12 h of injection. The photodynamic therapeutic effects were investigated by monitoring the change in tumor volumes and body weight in each group every day up to 10 days. The tumor volumes were calculated by using the equation of $\text{length} \times (\text{width})^2 \times 1/2$, where the length and width are the longest and shortest diameters (mm) of the tumor, respectively. The relative tumor volumes were calculated relative to the initial volumes.

Statistical Analysis. All data shown mean corrected values \pm SD of at least three independent experiments. Significant differences were determined based on the Student's t-test where differences were considered significant ($p < 0.05$). Statistical analyses were performed with the GraphPad Software.

3.1.3. Results and Discussion

The suspension of as-prepared CD was highly stable in aqueous solution, with a zeta-potential of -39.8 ± 0.45 mV. The negative surface charge clearly indicated the presence of surface functional groups such as carboxylic acid and alcohol groups, imparting sufficient colloidal stability to the CDs. As shown in Fig. 3.1a, the broad UV/vis absorption of the as-prepared CD and surface-passivated CD-PEG and CD-PEG-FA at approximately 230 nm represents the typical absorption of an aromatic system, reminiscent of an sp^2 -carbon network.³⁵ In addition, the successful functionalization of FA onto the CD surface was clearly evident from the peak at 283 nm.³⁶ The zeta-potentials of CD-PEG and CD-PEG-FA were determined to be -12.4 ± 0.75 and -8.24 ± 1.96 mV (pH 7.3), respectively, suggesting the loss of the carboxylic acid groups upon surface passivation. Moreover, CD-PEG and CD-PEG-FA displayed bright blue emission under UV irradiation (inset in Fig. 3.1a). For reference, the quantum yield (QY) of as-prepared CDs using quinine sulfate was measured to be 2.1%. After surface passivation, however, the QYs increased

significantly to 7.8% for CD-PEG and 10.9% for CD-PEG-FA (Fig. 3.2). Furthermore, the exciton lifetime was determined by the time-correlated single photon counting (TCSPC) technique, yielding 1.55, 4.13, and 5.52 ns for CD, CD-PEG, and CD-PEG-FA, respectively. This trend matches well with the QY of respective CD derivatives (Fig. 3.3). The fluorescence emission maxima were located at 450 nm for both CD-PEG and CD-PEG-FA ($\lambda_{\text{ex}} = 360$ nm), and the broad emission peak maxima were strongly dependent on the excitation wavelength, similar to typical CDs reported (Fig. 3.1b and Fig. 3.4).^{37, 38}

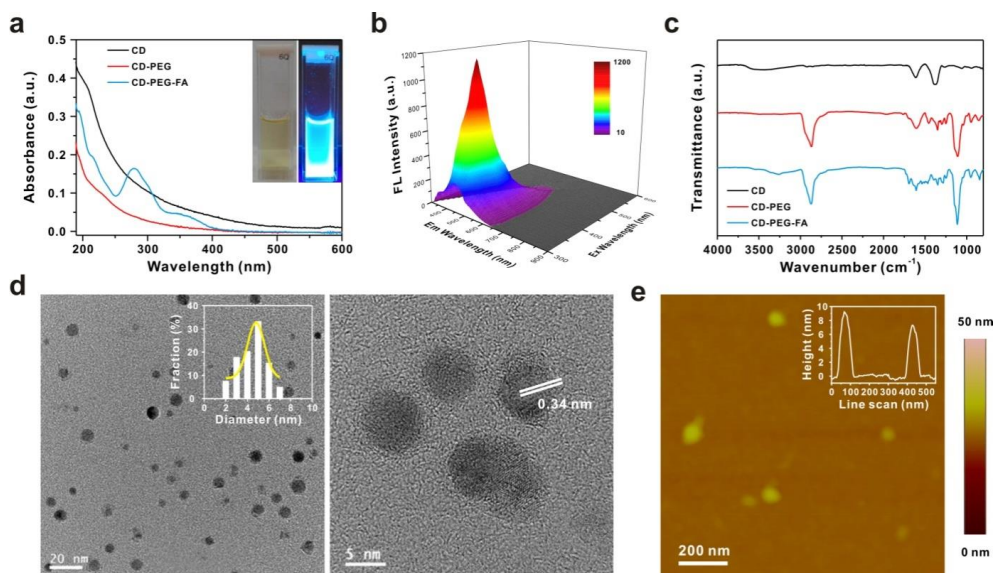


Figure 3.1. a) UV-vis absorbance spectra of CD, CD-PEG, and CD-PEG-FA. Inset shows the CD-PEG-FA suspension (left) under room light and (right) UV illumination at 365 nm. b) Three-dimensional fluorescence spectra of CD-PEG-FA under varying excitation wavelengths from 300 to 600 nm with 10-nm increments. c) FT-IR spectra of CD, CD-PEG, and CD-PEG-FA. d) TEM images of CD-PEG-FA with a corresponding size distribution histogram. e) Representative height-mode AFM topography image of CD-PEG-FA with a line scan profile in the inset.

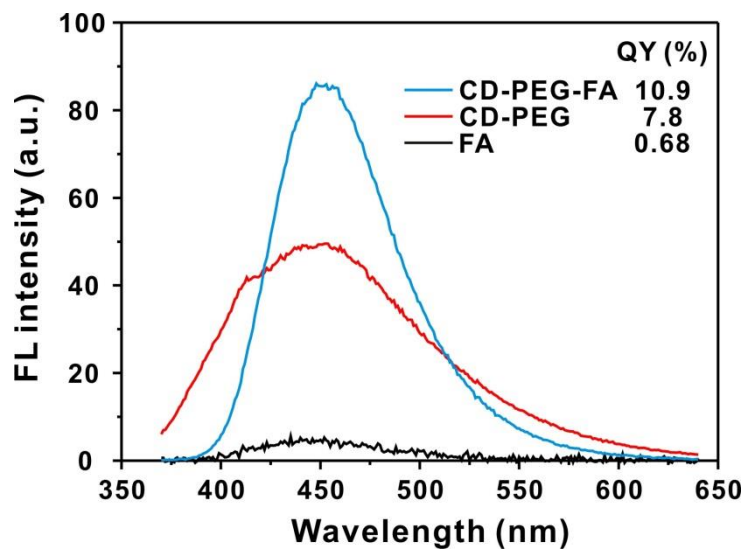


Figure 3.2. Fluorescence spectra of free FA, CD-PEG, and CD-PEG-FA. The QY increase after the FA conjugation is resulted from the successful surface passivation of CD with a small molecule like FA.

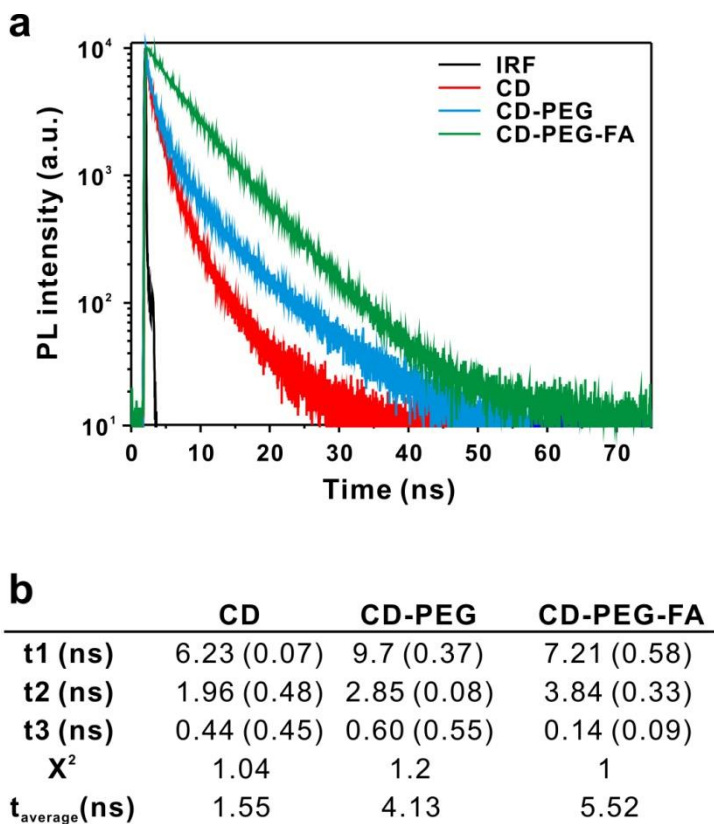


Figure 3.3. a) Time-resolved PL signal measured by time-correlated single photon counting (TCSPC) and b) exciton lifetime of CD, CD-PEG and CD-PEG-FA.

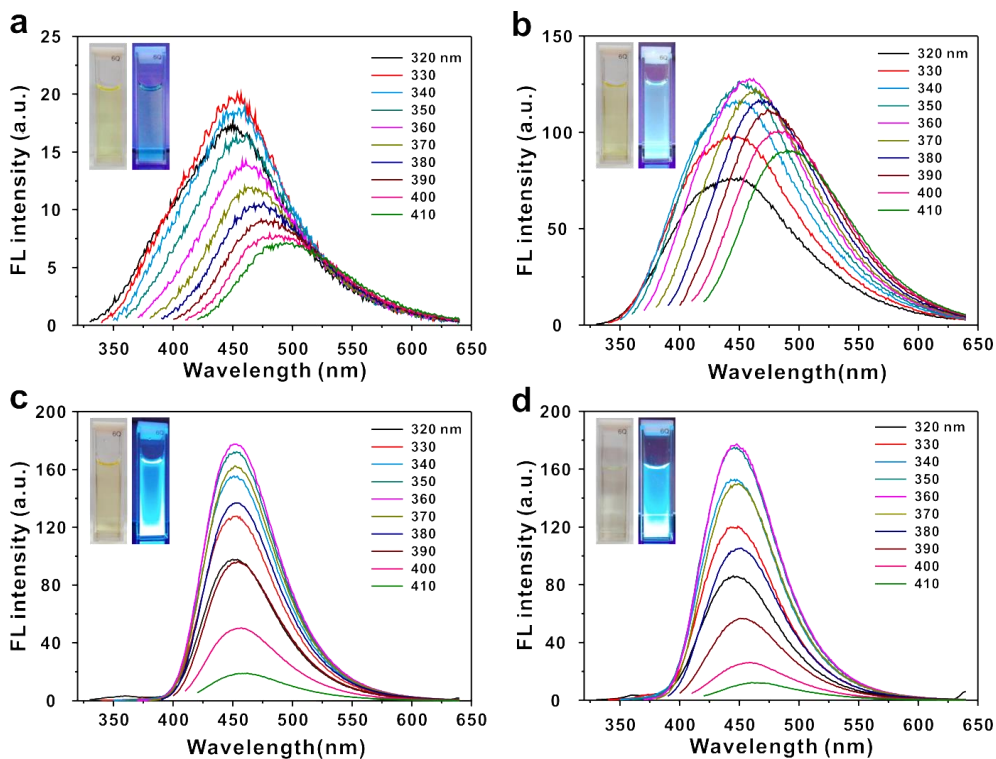


Figure 3.4. Photoluminescence spectra of a) CD, b) CD-PEG, c) CD-PEG-FA, and d) CD-PEG-FA/ZnPc. Inset images represent the optical images of the respective CDs under (left) ambient light and (right) UV light at 365 nm.

FT-IR spectroscopy revealed changes in the chemical functional groups on the CDs upon surface passivation. The as-prepared CDs showed peaks at 1,068 (C-O stretching), 1,608 (C=C stretching), 2,848 and 2,925 cm^{-1} (C-H stretching), and a broad peak at 3457 cm^{-1} that corresponded to carboxylic acid and hydroxyl groups (Fig 3.1c). Upon surface passivation, the presence of new bands at 1,594 (N-H in-plane) and 1,340 cm^{-1} (C-N stretching) confirmed the successful formation of amide groups by chemical conjugation of the surface carboxylic acid groups of the CDs with the amine-terminated PEG. Furthermore, the PEG surface passivation significantly increased the peak due to the C-O groups at 1,102 cm^{-1} . After passivation with FA, CD-PEG-FA exhibited characteristic peaks at 1,481, 1,605, and 1,697 cm^{-1} which corresponded to FA.³⁹ In accordance with the above results, high-resolution X-ray photoelectron spectroscopy (XPS) measurements further confirmed the composition of the respective CDs and the successful surface passivation (Fig. 3.5).

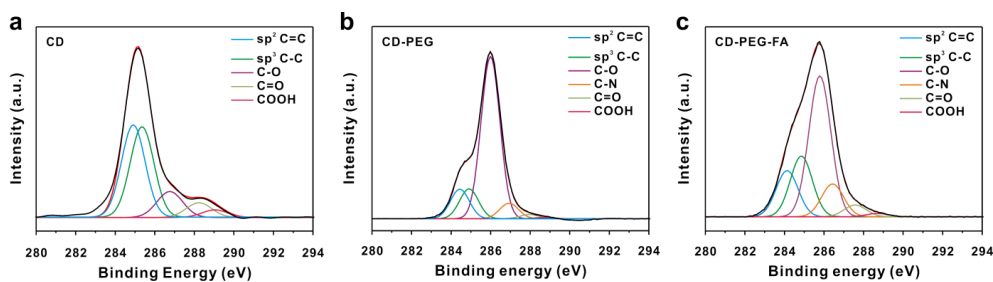


Figure 3.5. Deconvoluted high-resolution XPS C 1s peak of a) CD, b) CD-PEG, and c) CD-PEG-FA. CD has sp^3 carbon (284.94 eV), sp^2 carbon (285.40 eV), C-O groups (286.8 eV), C=O groups (288.2 eV) and COOH groups (289.08 eV), indicating that CDs are rich in hydroxyl, carbonyl and carboxylic acid groups on the surfaces. After passivation with amine-terminated PEG, the intensity of C-O peak is increased at 286.28 eV due to C-O groups in PEG. Further, the amount of carbonyl group is decreased from 6.06% to 0.50% with a concomitant appearance of the new peak of C-N group is observed at 287.43 eV, which indicates carbonyl group in CD and amine group in PEG is successfully reacted to amide groups. In addition, the intensities of C-N, C=O and COOH groups are increased in CD-PEG-FA, which also confirms the formation of more amide groups between the free amine-terminated PEG and FA after passivation with FA.

The size and morphology of the CDs were observed by transmission electron microscopy (TEM) and atomic force microscopy (AFM). The TEM images showed a spherical morphology of the CDs, with an average diameter of 4.5 ± 0.2 nm for CD-PEG-FA (Fig. 3.1d). The interlayer spacing of 0.34 nm, observed using high-resolution TEM, corresponded to that of graphitic carbon, representing the graphitic nature of the CDs. The AFM line scans indicated that the diameters of CD, CD-PEG and CD-PEG-FA were approximately 3.5, 4.4, and 4.9 nm, respectively, consistent with the stepwise surface functionalization with PEG and FA of the CDs (Fig. 3.1e and Fig. 3.6)

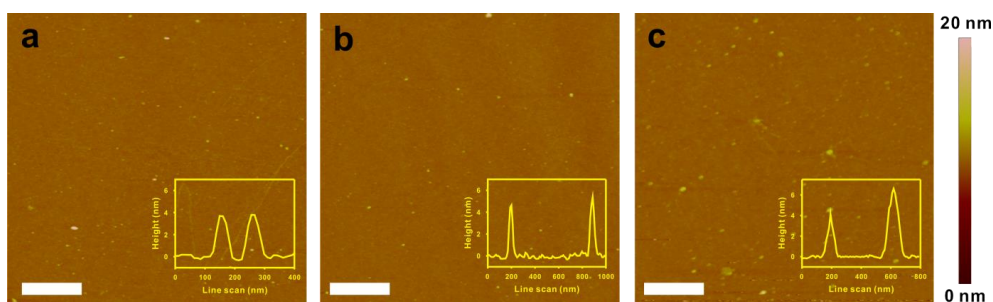


Figure 3.6. Height-mode AFM images of a) CD, b) CD-PEG and c) CD-PEG-FA with corresponding line scan profiles. The scale bar is 1 μm .

After characterization of the chemically functionalized CDs, ZnPc was loaded onto CD-PEG-FA by $\pi - \pi$ stacking interactions. The CD-PEG-FA carrying ZnPc (CD-PEG-FA/ZnPc) exhibited red-shifted absorption peaks at 607 and 689 nm, which originated from ZnPc and strongly quenched the fluorescence of ZnPc, suggesting the successful loading of ZnPc (Fig. 3.7).^{25,40-43} The characteristic fluorescence spectrum and QY of CD-PEG-FA did not alter upon loading with ZnPc (6 wt% of ZnPc/CD-PEG-FA, Fig. 3.4). AFM and dynamic light scattering (DLS) analysis showed no aggregation of CD-PEG-FA/ZnPc, suggesting the uniform loading of ZnPc onto the surface of CD-PEG-FA carrier by $\pi - \pi$ stacking interactions (Fig. 3.8)

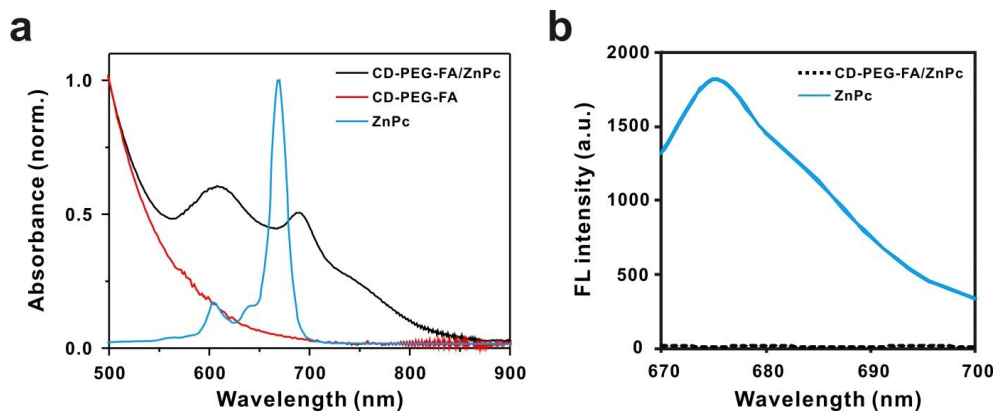


Figure 3.7. a) UV-vis absorbance spectra of (red) CD-PEG-FA, (black) CD-PEG-FA/ZnPc and (blue) free ZnPc. b) Fluorescence spectra of (solid line) free ZnPc, (dotted line) CD-PEG-FA/ZnPc with an excitation wavelength of 650 nm.

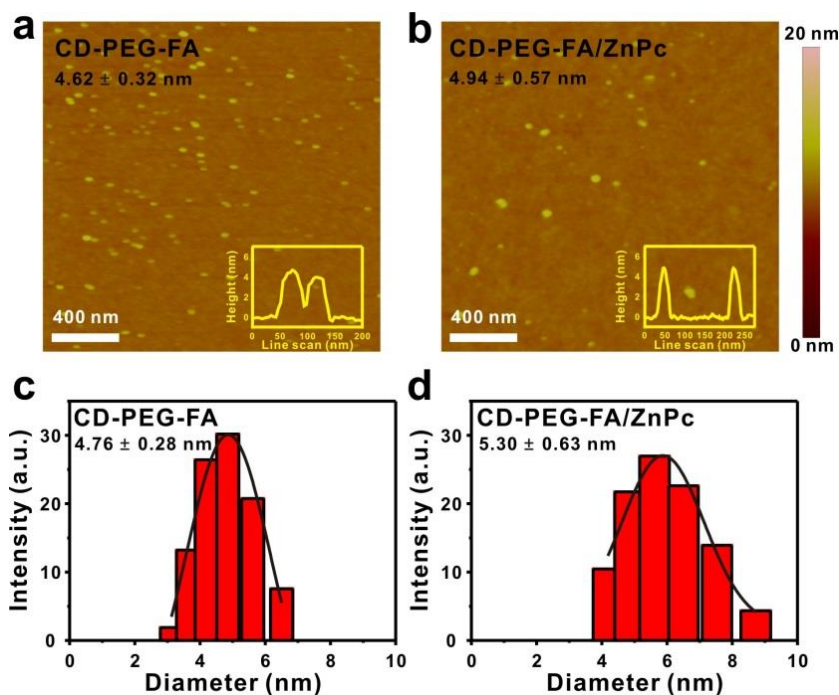


Figure 3.8. a, b) AFM and c, d) Dynamic light scattering (DLS) of a, c) CD-PEG-FA and b, d) CD-PEG-FA/ZnPc.

To investigate the efficacy of the CD-PEG-FA/ZnPc in targeted delivery and photodynamic therapy, we employed human cervical cancer HeLa cells, which are known to overexpress the folate receptor- α .⁴⁴ Initially, a conventional CCK-8 based cell viability assay suggested the superior biocompatibility of CD and its derivatives toward the HeLa cells under the present working concentration ranges of the

respective CD derivatives (5 – 450 $\mu\text{g/mL}$), as reported in other work (Fig. 3.9 and 3.10).⁴⁵ As shown in Figure 3.11 and Fig. 3.12, the targeting of CD-PEG, CD-PEG-FA, and CD-PEG-FA/ZnPc was evaluated after incubation with the HeLa cells for 12 h, by monitoring the blue and red fluorescence of CD ($\lambda_{\text{ex}}/\lambda_{\text{em}} = 358/461 \text{ nm}$) and ZnPc ($\lambda_{\text{ex}}/\lambda_{\text{em}} = 647/665 \text{ nm}$), respectively, to probe the internalization of CD and ZnPc under a fluorescence microscope. As expected, the cells incubated with CD-PEG-FA displayed intense CD fluorescence in the cytoplasm, whereas CD-PEG exhibited no sign of internalization into the HeLa cells, even when treated with an identical concentration of CD-PEG-FA. In accord with CD-PEG-FA, CD-PEG-FA/ZnPc was also internalized in the HeLa cells, with prominent fluorescence signals of both the blue (CD) and red (ZnPc) channels, indicating the successful intracellular delivery of ZnPc by the CD carrier. To clarify the targeting role of FA, a competition assay was performed with free FA. The folate receptors on the HeLa cells were first saturated with free FA, followed by the introduction of CD-PEG-FA/ZnPc, which clearly

demonstrated no cellular internalization (Fig. 3.11d). The targeting affinity and efficacy based on the FA and folate receptor was further evaluated using folate receptor overexpressed (FR+) and folate receptor deficient (FR-) cell lines. After incubated with CD-PEG/ZnPc and CD-PEG-FA/ZnPc, FR+ MDA-MB-231 cells were monitored by fluorescence microscope, and FR- A549 cells were used as a negative control. Fig. 3.13 showed that the fluorescent CD and ZnPc were localized with intracellular cytoplasm, indicating that CD-PEG-FA/ZnPc was effectively internalized into the cells through the close rapport between FA and FR. However, no significant fluorescence was observed in FR- A549 cells and even CD-PEG/ZnPc treated MDA-MB-231 cells.

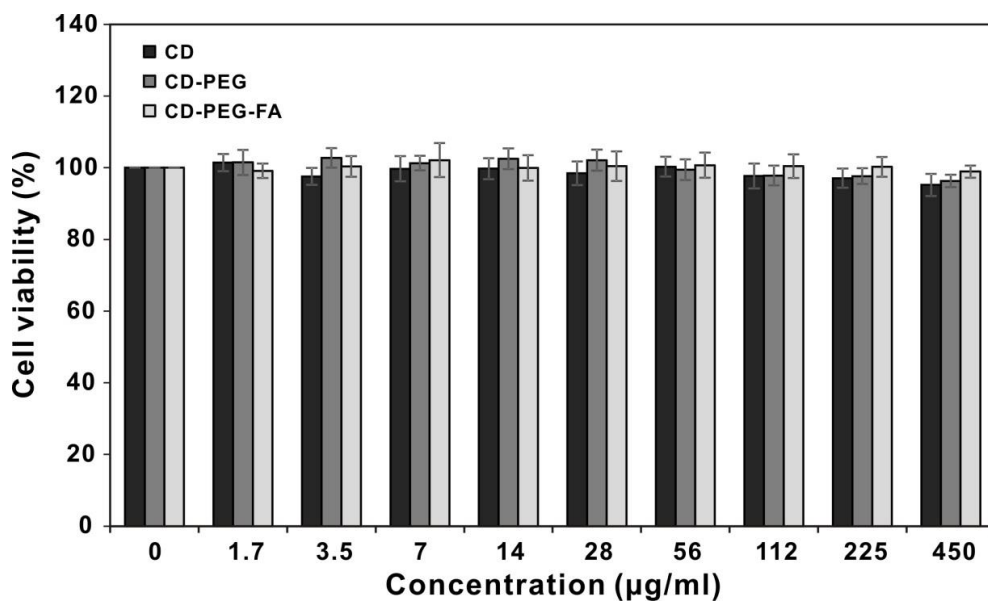


Figure 3.9. CCK-8 based cell viability assays with HeLa cells with different concentration of CD, CD-PEG and CD-PEG-FA.

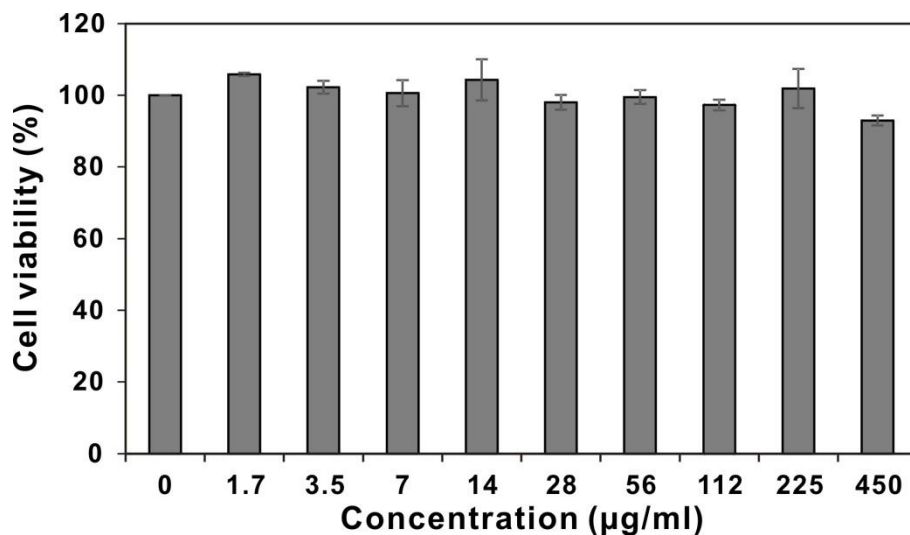


Figure 3.10. CCK-8 based cell viability assays with HeLa cells with different concentration of CD-PEG-FA/ZnPc.

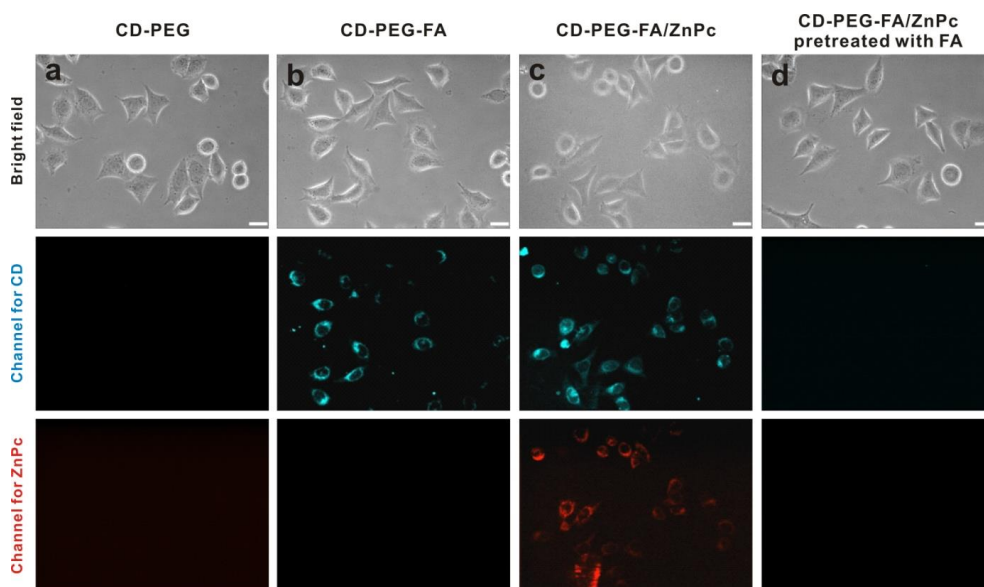


Figure 3.11. a–d) Bright–field and fluorescence images of HeLa cells treated with CD derivatives (50 mg/ml) for 12 h. a) CD–PEG, b) CD–PEG–FA, c) CD–PEG–FA/ZnPc and d) CD–PEG–FA/ZnPc pretreated with folic acid. Fluorescence signals of (blue) CDs and (red) ZnPc were observed at 461 nm ($\lambda_{ex} = 358$ nm) and 665 nm ($\lambda_{ex} = 647$ nm), respectively. Scale bar is 20 nm.

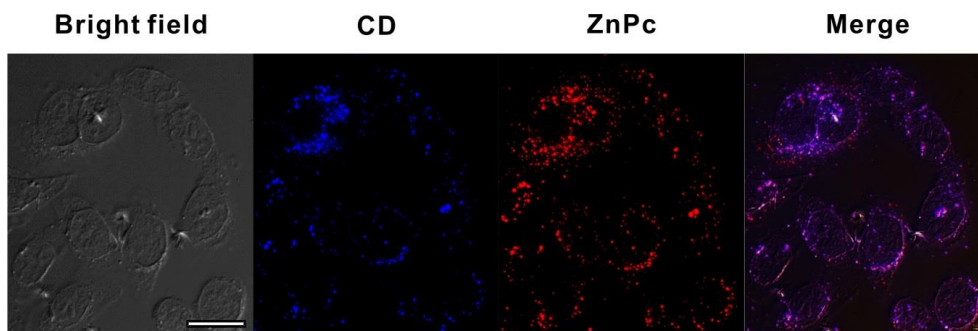


Figure 3.12. Bright field and fluorescence images of HeLa cells treated with CD-PEG-FA/ZnPc (50 $\mu\text{g}/\text{ml}$) for 12 h. Fluorescence signals of (blue) CDs and (red) ZnPc were observed by using Deltavision high-resolution microscopy. Scale bar is 20 μm .

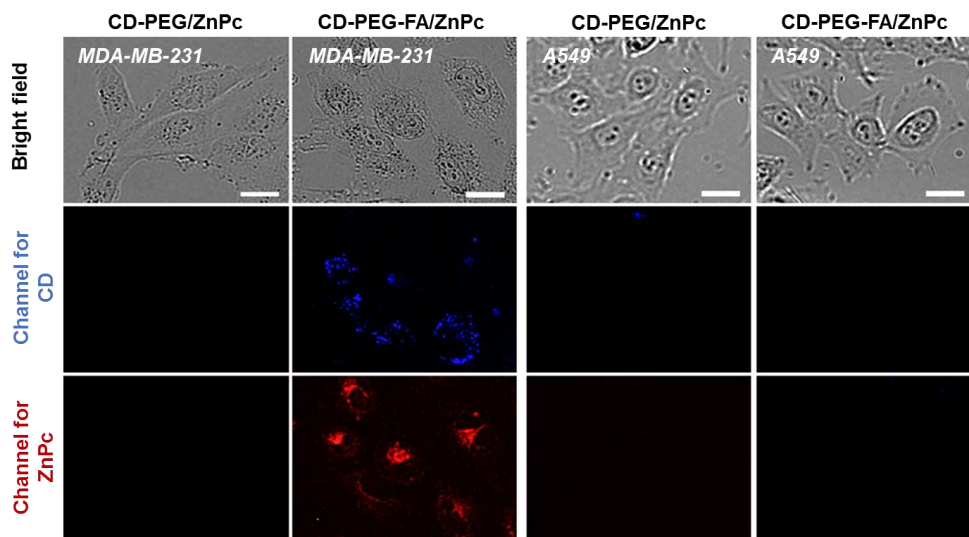


Figure 3.13. Fluorescence of CD-PEG/ZnPc was measured in folate receptor (FR) overexpressed cell (MDA-MB-231 cells) and FR deficient cell (A549 cells) by In-cell analyzer 2000 after 12 h incubation. No significant fluorescence of CD and ZnPc were observed in A549 cells and CD-PEG/ZnPc treated MDA-MB-231 cells. Scale bar is 20 μm .

Taken together, these results corroborate that the folate receptors overexpressed on the surface of the HeLa cells facilitate the recognition of the CD-PEG-FA and induce the preferential uptake of CD-PEG-FA by receptor-mediated endocytosis.^{44, 46, 47} Since the passive targeting of the PS is inadequate for in vivo photodynamic treatment through systemic administration, the modification of active targeting ligands to the surface of the CD is critical to increase the local concentration of the PS in tumors, and thus helps in avoiding side effects and maximizes the therapeutic efficacy.

Next, we performed a photodynamic therapy on the HeLa cells with the CD derivatives. (Fig. 3.14) The cells were exposed to the CD derivatives for 12 h followed by laser irradiation (660 nm, 30 mW/cm²) for 10 min. Significant cell death was observed in CD-PEG-FA/ZnPc, whereas other samples treated with CD-PEG, CD-PEG-FA and FA-pretreated CD-PEG-FA/ZnPc did not exhibit measurable photodynamic activity (Fig. 3.14a-d and Fig. 3.15). In addition, the generation of the active singlet oxygen species via photoinduced energy transfer from ZnPc was quantified by

using the singlet oxygen sensor green (SOSG) reagent;^{48, 49} the green fluorescence ($\lambda_{em} = 525 \text{ nm}$) is known to increase when SOSG reacts with singlet oxygen generated from the PS, which can be used for quantification of singlet oxygen generation.^{50, 51} Fig. 3.14e shows the fluorescence intensity as a function of irradiation time; the intensity gradually increases upon irradiation with an LED (30 mW/cm^2). While the control ZnPc without SOSG did not exhibit any fluorescence changes, ZnPc and CD-PEG-FA/ZnPc mixed with SOSG showed an increase in the fluorescence intensity upon irradiation. It is of note that SOSG alone showed increasing fluorescence intensity upon irradiation, since SOSG itself can act as a PS and thus generate singlet oxygen species.⁵² Because of intermolecular energy transfer between ZnPc and CD, the CD-PEG-FA/ZnPc did not effectively generate singlet oxygen relative to free ZnPc with SOSG. However, singlet oxygen generation was considerably accelerated upon the addition of cell lysate (Fig. 3.14e, $t = 25 \text{ min}$), indicating the release of ZnPc from CD via the competitive displacement of ZnPc by interaction with the biomolecules in cell lysate, thus

enhancing the therapeutic efficiency of photodynamic therapy.

Quantitative CCK-8 cell viability assays, used to investigate the effects of concentration and laser irradiation, were carried out using the HeLa cells incubated for 12 h (Fig. 3.14f). For example, the cell viabilities of free ZnPc, CD-PEG-FA/ZnPc without irradiation, and CD-PEG-FA/ZnPc with irradiation were determined to be 60.9%, 94.2%, and 8.2%, respectively, at a concentration of 100 $\mu\text{g/mL}$. The result clearly confirms that the generation of singlet oxygen, and thus, effective photodynamic action necessitates both suitable concentrations of the PS and appropriate light irradiation. Moreover, the significant difference in the viability between the irradiated CD-PEG-FA/ZnPc and free ZnPc is consistent with the preferential internalization of CD-PEG-FA/ZnPc into the HeLa cells, which results in considerably improved therapeutic efficacy of photodynamic action.

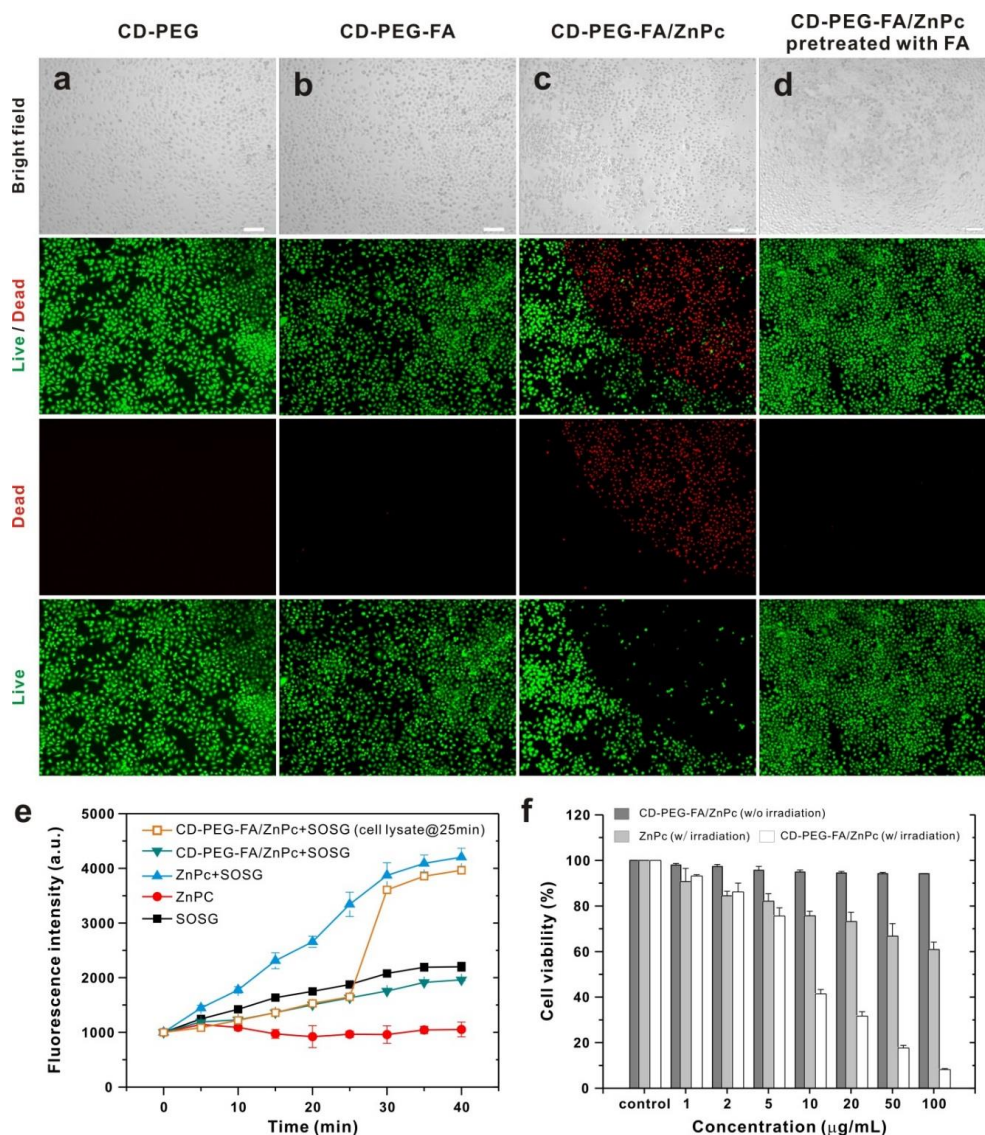


Figure 3.14. a–d) (top panel) Bright–field and fluorescence images of HeLa cells treated with CD derivatives ($50 \mu\text{g/ml}$) for 12 h, followed by irradiation for 10 min with a 660 nm laser (30 mW/cm^2), and (bottom panels) live and dead cells colored green and red, respectively, by live/dead assay. a) CD–PEG, b) CD–PEG–FA, c) CD–PEG–FA/ZnPc, and d) CD–PEG–FA/ZnPc with pretreatment of excess free FA.

Scale bar is 100 μ m. e, f) Quantitative evaluation of photodynamic effect. e) Singlet oxygen detection test using a singlet oxygen sensor green (SOSG) reagent. Time-dependent fluorescent intensity ($\lambda_{ex}/\lambda_{em} = 504/530$ nm) with irradiation by using a 660 nm laser (30 mW/cm²). Concentrations of ZnPc and SOSG used are 3.8 and 2.5 μ M, respectively. Note that the addition of cell lysate (1 mL) in CD-PEG-FA/ZnPc did not change the effective concentrations of ZnPc and SOSG. f) Cell viability assay depending on the concentration of ZnPc loaded CD-PEG-FA and ZnPc with and without irradiation for 10 min. All experiments were carried out in triplicate; the error bars represent the standard deviation.

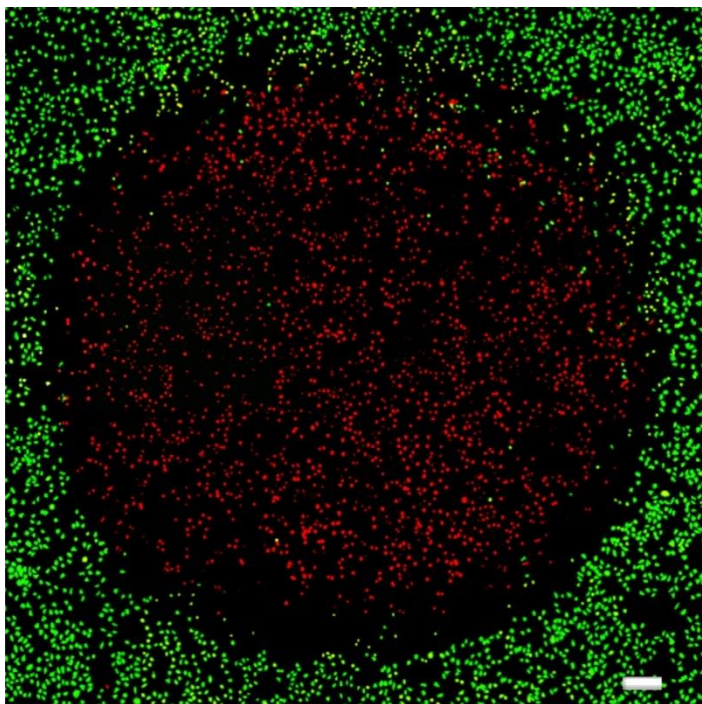


Figure 3.15. Fluorescence image of HeLa cells which were treated with CD-PEG-FA/ZnPc (50 $\mu\text{g}/\text{ml}$) for 12 h followed by irradiation with a 660-nm laser (30 mW/cm^2) for 10 min. Live and dead cells were colored green and red, respectively by live/dead assay. Scale bar is 100 μm .

Encouraged by the high PDT efficacy in vitro, we next investigated the PDT efficacy of the CD-mediated PS delivery system in animal models. Tumor-bearing mice were first prepared by subcutaneously injecting a suspension of the

HeLa cells (6×10^6 cells) in sterilized 1X PBS solution into BALB/c nude mice (6 weeks old). To monitor the biodistribution of the CD derivatives in vivo, the fluorescence images from the whole body were obtained at designated time points after the various CD derivatives were injected into tail veins. As shown in Fig. 3.16a and 3.16b, the mice treated with CD-PEG-FA/ZnPc showed strong fluorescence signals corresponding to ZnPc in tumors, with gradual increase in the fluorescence intensity over time, in contrast to the mice treated with CD-PEG/ZnPc or CD-PEG-FA. Biodistribution of the CD derivatives was further examined by imaging major organs that were excised after sacrificing the mice administered with the CD derivatives. Fluorescence images of the major organs in Fig. 3.16c showed that the fluorescence corresponding ZnPc were intense in liver and spleen rather than tumor in case of the mouse injected with CD-PEG/ZnPc, suggesting that most of the CDs omitting targeting ligand FA leaked out by circulation and prominently accumulated in reticuloendothelial system of the liver and spleen.^{53,54} These results showed that conjugation of FA to CD played an

important role in greatly improving the active tumor–targeting capability of the ZnPc delivery vehicle to folate receptor–overexpressing tumors.

Finally, to investigate the therapeutic efficacy *in vivo*, changes in tumor volumes were monitored for 10 days after CD–PEG–FA, CD–PEG/ZnPc, and CD–PEG–FA/ZnPc (0.5 mg of ZnPc/kg of mouse) were intravenously injected to mice whose tumor volumes were $\sim 70 \text{ mm}^3$. The same volume of saline was treated as a control, and the relative tumor volumes were determined by comparing its volumes at different time points to the initial volumes (Fig. 3.16d and 3.16e). After irradiation with a 660–nm laser (0.3 W/cm^2 , 20 min), the mice treated with CD–PEG–FA/ZnPc showed remarkable suppression of tumor growth as compared to the control mice for 8 days. However, the mice treated with CD–PEG/ZnPc and CD–PEG–FA, with or without laser irradiation, showed no notable difference in tumor size compared to the controls. This result was in agreement with the *in vitro* data, indicating that a combination of targeted delivery of ZnPc and light irradiation can effectively induce cancer cell death *in vivo*.

Collectively, the *in vivo* study suggested that the present tumor-targeted CD-based PDT therapeutic agent delivery system can effectively induce the accumulation of the PS-loaded CDs in tumors, thus leading to enhanced therapeutic efficacy with a relatively small quantity of ZnPc.

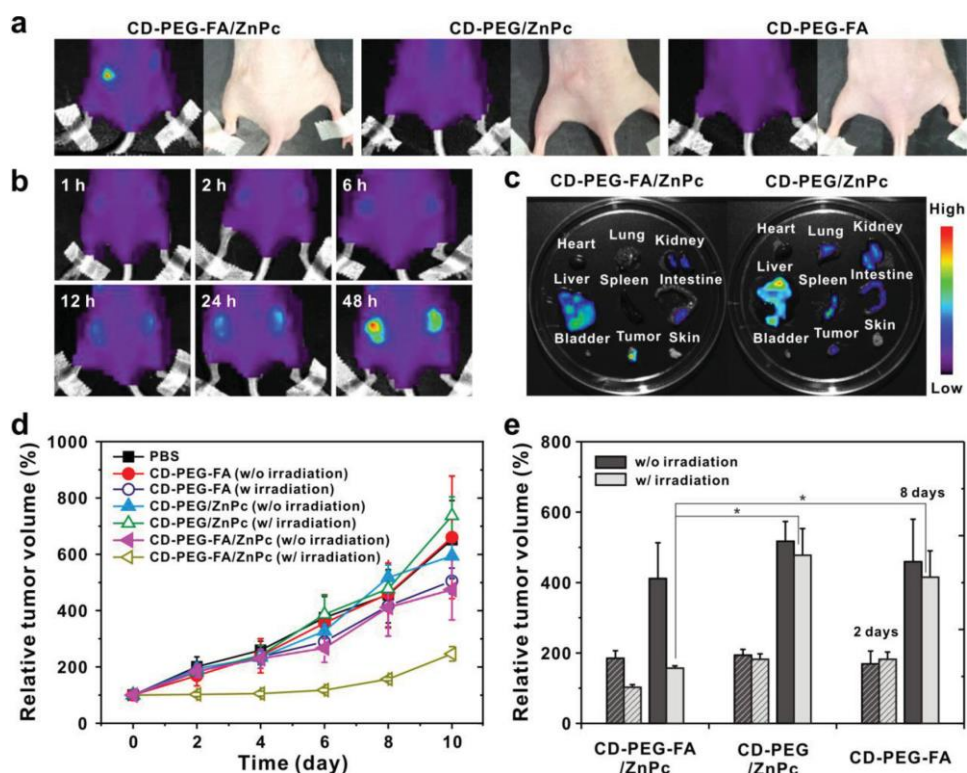


Figure 3.16. a) Fluorescence of ZnPc (excited at 660 nm) in tumor was imaged after 12 h injection of CD-PEG-FA/ZnPc, CD-PEG/ZnPc, and CD-PEG-FA (0.5 mg of ZnPc/kg mouse). b) CD-PEG-FA/ZnPc suspensions were injected into tail

veins of tumor-bearing mice and the fluorescent signals were obtained at various time points (1, 2, 6, 12, 24, and 48 h). c) Ex vivo fluorescence images of major organs of mice. The fluorescent signals corresponding to ZnPc (excited at 660 nm) from major organs, tumor, and skin were obtained after 12 h of i.v. injection of CD-PEG-FA/ZnPc and CD-PEG/ZnPc into tumor-bearing mice. FA-conjugated CD delivered and released ZnPc to tumor effectively, in contrast with the CD lacking FA. d,e) Relative tumor volumes measured over time after the tumor-bearing mice were treated with various CD derivatives. Tumor-bearing mice were separated into 6 groups: (i) PBS control; (ii) CD-PEG-FA without irradiation; (iii) CD-PEG-FA with irradiation; (iv) CD-PEG/ZnPc without irradiation; (v) CD-PEG/ZnPc with irradiation; (vi) CD-PEG-FA/ZnPc without irradiation; (vii) CD-PEG-FA/ZnPc with irradiation (n=4 for each group). Irradiation was performed using a 660-nm laser at 0.3 W/cm^2 . Tumor volumes were measured over 10 days. It is notable that no significant increase in tumor volume was observed for 8 days in mice treated with CD-PEG-FA/ZnPc with irradiation. P-values were calculated by Student's t-test: * for $p < 0.05$, n=4.

3.1.4. Conclusion

In summary, we developed a novel theranostic platform based on FA-conjugated CD loaded with ZnPc in the present study. We have successfully demonstrated the targeted delivery of a PS via FA-mediated endocytosis of biocompatible CD-PEG-FA/ZnPc and therapeutic photodynamic efficacy by singlet oxygen generation from the internalized ZnPc upon light irradiation in vitro and in vivo. We anticipate that the present CD-based targeted delivery of the PS would offer a convenient and effective platform for enhanced photodynamic therapy to treat cancers in the near future because of its excellent biocompatibility, bioimaging and targeting capability, and therapeutic efficacy.

3.1.5. References

1. Weissleder, R. *Nat. Rev. Cancer* **2002**, 2, 11.
2. Willmann, J. K.; van Bruggen, N.; Dinkelborg, L. M.; Gambhir, S. S. *Nat. Rev. Drug Discovery* **2008**, 7, 591.
3. Barreto, J. A.; O'Malley, W.; Kubeil, M.; Graham, B.; Stephan, H.; Spiccia, L. *Adv. Mater.* **2011**, 23, H18.
4. Alivisatos, A. P. *Science* **1996**, 271, 933.
5. Michalet, X.; Pinaud, F. F.; Bentolila, L. A.; Tsay, J. M.; Doose, S.; Li, J. J.; Sundaresan, G.; Wu, A. M.; Gambhir, S. S.; Weiss, S. *Science* **2005**, 307, 538.
6. Medintz, I. L.; Uyeda, H. T.; Goldman, E. R.; Mattoussi, H. *Nat. Mater.* **2005**, 4, 435.
7. Derfus, A. M.; Chan, W. C. W.; Bhatia, S. N. *Nano Lett.* **2004**, 4, 11.
8. Hardman, R. *Environ. Health Perspect.* **2006**, 114, 165.
9. Yang, S. T.; Cao, L.; Luo, P. G. J.; Lu, F. S.; Wang, X.; Wang, H. F.; Mezziani, M. J.; Liu, Y. F.; Qi, G.; Sun, Y. P. *J. Am. Chem. Soc.* **2009**, 131, 11308.
10. Baker, S. N.; Baker, G. A. *Angew. Chem. Int. Ed.* **2010**, 49, 6726.
11. Li, H. T.; Kang, Z. H.; Liu, Y.; Lee, S. T.; *J. Mater. Chem.* **2012**, 22, 24230.
12. Ray, S. C.; Saha, A.; Jana, N. R.; Sarkar, R.; *J. Phys. Chem. C* **2009**, 113, 18546.
13. Huang, P.; Lin, J.; Wang, X. S.; Wang, Z.; Zhang, C. L.; He, M.; Wang, K.; Chen, F.; Li, Z. M.; Shen, G. X.; Cui, D. X.;

- Chen, X. Y. *Adv. Mater.* **2012**, 24, 5104.
14. Tang, J.; Kong, B.; Wu, H.; Xu, M.; Wang, Y. C.; Wang, Y. L.; Zhao, D. Y.; Zheng, G. F. *Adv. Mater.* **2013**, 25, 6569.
 15. Wang, Q. L.; Huang, X. X.; Long, Y. J.; Wang, X. L.; Zhang, H. J.; Zhu, R.; Liang, L. P.; Teng, P.; Zheng, H. Z. *Carbon* **2013**, 59, 192.
 16. Dolmans, D. E. J. G. J.; Fukumura, D.; Jain, R. K. *Nat. Rev. Cancer* **2003**, 3, 380.
 17. Henderson, B. W.; Dougherty, T. J. *Photochem. Photobiol.* **1992**, 55, 145.
 18. Lovell, J. F.; Liu, T. W. B.; Chen, J.; Zheng, G.; *Chem. Rev.* **2010**, 110, 2839.
 19. Konan, Y. N.; Gurny, R.; Allemann, E.; *J. Photochem. Photobiol. B* **2002**, 66, 89.
 20. Bechet, D.; Couleaud, P.; Frochet, C.; Viriot, M. L.; Guillemin, F.; Barberi-Heyob, M. *Trends Biotechnol.* **2008**, 26, 612.
 21. Derycke, A. S. L.; de Witte, P. A. M. *Adv. Drug Delivery Rev.* **2004**, 56, 17.
 22. Son, K. J.; Yoon, H. J.; Kim, J. H.; Jang, W. D.; Lee, Y.; Koh, W. G. *Angew. Chem. Int. Ed.* **2011**, 50, 11968.
 23. Kuo, W. S.; Chang, C. N.; Chang, Y. T.; Yang, M. H.; Chien, Y. H.; Chen, S. J.; Yeh, C. S. *Angew. Chem. Int. Ed.* **2010**, 49, 2711.
 24. Obaid, G.; Chambrier, I.; Cook, M. J.; Russell, D. A. *Angew. Chem. Int. Ed.* **2012**, 51, 6158.
 25. Tian, B.; Wang, C.; Zhang, S.; Feng, L. Z.; Liu, Z. *ACS*

- Nano* **2011**, 5, 7000.
26. Li, F.; Park, S.; Ling, D.; Park, W.; Han, J. Y.; Na, K.; Char, K. *J. Mater. Chem. B* **2013**, 1, 1678.
27. Zhu, Z.; Tang, Z. W.; Phillips, J. A.; Yang, R. H.; Wang, H.; Tan, W. H. *J. Am. Chem. Soc.* **2008**, 130, 10856.
28. Sharman, W. M.; van Lier, J. E.; Allen, C. M. *Adv. Drug Delivery Rev.* **2004**, 56, 53.
29. Verma, S.; Watt, G. M.; Mal, Z.; Hasan, T. *Photochem. Photobiol.* **2007**, 83, 996
30. Schmitt, F.; Juillerat–Jeanneret, L. *Anti–Cancer Agents Med. Chem.* **2012**, 12, 500.
31. Choi, H.; Ko, S. J.; Choi, Y.; Joo, P.; Kim, T.; Lee, B. R.; Jung, J. W.; Choi, H. J.; Cha, M.; Jeong, J. R.; Hwang, I. W.; Song, M. H.; Kim, B. S.; Kim, J. Y. *Nat. Photonics* **2013**, 7, 732.
32. Sun, Y. P.; Zhou, B.; Lin, Y.; Wang, W.; Fernando, K. A. S.; Pathak, P.; Mezziani, M. J.; Harruff, B. A.; Wang, X.; Wang, H. F.; Luo, P. J. G.; Yang, H.; Kose, M. E.; Chen, B. L. Veca, L. M.; Xie, S. Y. *J. Am. Chem. Soc.* **2006**, 128, 7756.
33. Leamon, C. P.; Low, P. S. *Drug Disc. Today* **2001**, 6, 44.
34. Owens, J. W.; Smith, R.; Robinson, R.; Robins, M. *Inorg. Chim. Acta* **1998**, 279, 226.
35. Tang, L. B.; Ji, R. B.; Cao, X. K.; Lin, J. Y.; Jiang, H. X.; Li, X. M.; Teng, K. S.; Luk, C. M.; Zeng, S. J.; Hao, J. H.; Lau, S. P. *ACS Nano* **2012**, 6, 5102.
36. Song, Y. C.; Shi, W.; Chen, W.; Li, X. H.; Ma, H. M.; *J. Mater. Chem.* **2012**, 22, 12568.

37. Qu, S. N.; Wang, X. Y.; Lu, Q. P.; Liu, X. Y.; Wang, L. J. *Angew. Chem. Int. Ed.* **2012**, 51, 12215.
38. Zhu, S. J.; Meng, Q. N.; Wang, L.; Zhang, J. H.; Song, Y. B.; Jin, H.; Zhang, K.; Sun, H. C.; Wang, H. Y.; Yang, B. *Angew. Chem. Int. Ed.* **2013**, 52, 3953.
39. Huang, H.; Yuan, Q.; Shah, J. S.; Misra, R. D. K. *Adv. Drug Delivery Rev.* **2011**, 63, 1332.
40. Zhang, M.; Murakami, T.; Ajima, K.; Tsuchida, K.; Sandanayaka, A. S. D.; Ito, O.; Iijima, S.; Yudasaka, M. *Proc. Natl. Acad. Sci. U. S. A.* **2008**, 105, 14773.
41. Sun, X. M.; Liu, Z.; Welsher, K.; Robinson, J. T.; Goodwin, A.; Zaric, S.; Dai, H. J. *Nano Res.* **2008**, 1, 203.
42. Liu, Z.; Robinson, J. T.; Sun, X. M.; Dai, H. J. *J. Am. Chem. Soc.* **2008**, 130, 10876.
43. Karousis, N.; Ortiz, J.; Ohkubo, K.; Hasobe, T.; Fukuzumi, S.; Sastre-Santos, A.; Tagmatarchis, N.; *J. Phys. Chem. C* **2012**, 116, 20564.
44. Wang, L. S.; Wu, L. C.; Lu, S. Y.; Chang, L. L.; Teng, I. T.; Yang, C. M.; Ho, J. A. A. *ACS Nano* **2010**, 4, 4371.
45. Tao, H. Q.; Yang, K.; Ma, Z.; Wan, J. M.; Zhang, Y. J.; Kang, Z. H.; Liu, Z. *Small* **2012**, 8, 281.
46. Leamon, C. P.; Reddy, J. A. *Adv. Drug Delivery Rev.* **2004**, 56, 1127.
47. Dohmen, C.; Frohlich, T.; Lachelt, U.; Rohl, I.; Vornlocher, H. P.; Hadwiger, P.; Wagner, E. *Mol. Ther. Nucleic Acids* **2012**, 1, e7.
48. Bonnett, R. *Chem. Soc. Rev.* **1995**, 24, 19.

49. MacDonald, I. J.; Dougherty, T. J.; *J. Porphyrins Phthalocyanines* **2001**, 5, 105.
50. Flors, C.; Fryer, M. J.; Waring, J.; Reeder, B.; Bechtold, U.; Mullineaux, P. M.; Nonell, S.; Wilson, M. T.; Baker, N. R. *J. Exp. Bot.* **2006**, 57, 1725.
51. Gollmer, A.; Arnbjerg, J.; Blaikie, F. H.; Pedersen, B. W.; Breitenbach, T.; Daasbjerg, K.; Glasius, M.; Ogilby, P. R. *Photochem. Photobiol.* **2011**, 87, 671.
52. Ragas, X.; Jimenez-Banzo, A.; Sanchez-Garcia, D.; Batllori, X.; Nonell, S. *Chem. Commun.* **2009**, 0, 2920.
53. Lammers, T.; Peschke, P.; Kuehnlein, R.; Subr, V.; Ulbrich, K.; Huber, P.; Hennink, W.; Storm, G. *Neoplasia* **2006**, 8, 788.
54. Moon, H. K.; Lee, S. H.; Choi, H. C. *ACS Nano* **2009**, 3, 3707.

3.2. Highly efficient gene silencing and bioimaging based on fluorescent carbon dot in vitro and in vivo

3.2.1. Introduction

RNA interference (RNAi) is a biological process discovered by A. Fire and C. C. Mello in 1998 where mRNA is sequence specifically cleaved and degraded by siRNA, resulting in target gene silencing.¹⁻³ RNAi pathway is accomplished by cellular machinery which requires the RNA-induced silencing complex (RISC) for target RNA degradation.⁴⁻⁷ Due to its convenience of transient target gene knockdown by using short RNAs of which sequence can be designed based on target mRNA sequence, RNAi has been widely used for both basic biological research and biomedical application.⁸ For therapeutic applications, siRNAs can be readily designed to silence target genes responsible for certain diseases, suggesting huge potential as a way of treating traditionally untargetable diseases.^{9,10} However, its gene silencing efficacy for disease treatment is limited by nuclease mediated siRNA degradation and low intracellular uptake of siRNA and

therefore, efficient siRNA delivery system is urgently needed.^{11,12}

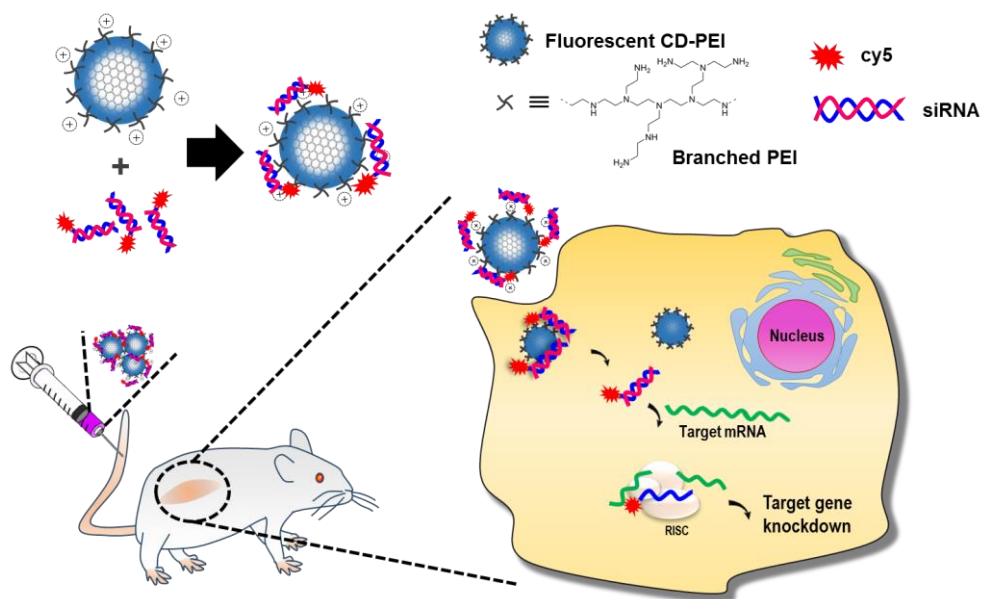
To develop therapeutic siRNA delivery system, various nanoparticles (NPs) including gold, magnetic, quantum dot, and silica NPs were employed in addition to cationic polymers and liposomes.¹³⁻²² In general, cationic polymers have shown relatively high cytotoxicity.²³ Many NP based siRNA delivery systems require chemically modified siRNAs and/or conjugation of siRNAs onto NP surface with subsequent purification of the siRNA conjugated NPs.^{9,10} These approaches possess limitations including time-consuming multi-step processes, high cost, and labor-intensiveness. Therefore, development of biocompatible, efficient, easy to prepare siRNA delivery system is an urgent issue for practical and clinical applications of siRNA mediated gene silencing.

Recently, carbon NP (also known as carbon dot, CD), a new class of carbon based nanomaterial, has received significant attention due to its low cytotoxicity, simple preparation, high chemical stability and unique optical properties like semiconducting quantum dots.²⁴⁻³¹ On top of

the intense fluorescence of CDs, their surface functional groups enhance aqueous solubility and provide flexibility in chemical modifications of the surface such as conjugation of targeting ligands. Taking advantages of their excellent optical and chemical properties, CDs have been employed in a number of biological applications, including plasmid DNA/drug delivery, bioimaging, biosensing, and photo-induced therapy.³²⁻⁴⁰ Although the CD derivatives provides high potentials for therapeutic application, a challenge still remains for in vivo therapeutic system, which requires targeting capability with biological imaging ability to enhance tumor-specific treatment following systemic administration.

Herein, we synthesized highly fluorescent poly(ethylene imine) (PEI)-passivated CD (CD-PEI) as a novel carrier for siRNA delivery to simultaneously achieve bioimaging and knockdown of target gene. CD-PEI was synthesized via one-step household microwave pyrolysis using citric acid and PEI. In this synthetic scheme, the PEI used as a passivation agent plays multiple roles—enhancing fluorescence of CD, siRNA loading capacity and cellular uptake.⁴¹ Prior to cellular

treatment, siRNA/CD-PEI complex was first prepared through electrostatic interaction between siRNA and CD-PEI by simply mixing two components in buffered solutions. We showed that the siRNAs complexed with CD-PEI were protected from RNase mediated degradation, implying longer chemical stability compared to naked siRNA in vivo. The siRNA/CD-PEI complex was successfully employed for the sequence specific knockdown of target gene expression in vitro and in vivo as well as for convenient monitoring of the cellular uptake of the therapeutic complex with systemic introduction in real time (Scheme 3.2).



Scheme 3.2. Strategy of CD-PEI mediated siRNA delivery and bioimaging. Complex of CD-PEI and siRNA is formed by electrostatic interaction between CD-PEI and siRNA. After cellular uptake of the siRNA/CD-PEI complex, siRNA is released from CD-PEI and the target gene knockdown is achieved by siRNA-RISC complex. Fluorescence of CD-PEI itself enabled fluorescent image based monitoring of cellular uptake of siRNA/CD-PEI complex and intracellular localization of CD-PEI in living cells.

3.2.2. Materials and methods

Materials. Citric acid and branched poly(ethylene imine) (PEI, $M_w = 10,000$) was purchased from Sigma–Aldrich and Polyscience.Inc, respectively. 10x Phosphate buffered saline (PBS), Dulbecco’s modified eagle’s medium (DMEM), and fetal bovine serum (FBS) were purchased from WELGENE, Korea. SYBR® Gold nucleic acid gel stain was purchased from Life Technologies, USA. Cell counting kit–8 (CCK–8) was purchased from Dojindo Laboratories (Japan). RNase was purchased from New England Biolabs, USA. All siRNA was purchased from Bioneer, Korea.

Synthesis of PEI–passivated CD (CD–PEI). To synthesize CD–PEI, 250 mg of PEI (25 mmol) was first dissolved in 5 mL water, and 500 mg of citric acid (2.6 mmol) was added. The transparent mixed solution was placed into a microwave oven and heated for 2 min. After the solution cooled down to room temperature, the obtained white–yellow solid was dissolved in 5 mL of water and dialyzed using SpectraPore (MWCO 12,000) for 2 days to remove excess salts, unreacted citric acid and free PEI.

Characterizations. UV/vis spectrophotometer (UV-1800, Shimadzu, Japan) was used to measure absorbance of the CD-PEI derivatives solution. Fluorescence data was obtained by a fluorometer (Agilent, USA). Three-dimensional fluorescence spectrum of CD-PEI derivatives was obtained with spectrofluorometer FP-8300 (JASCO, USA). Transmission electron microscopy (TEM, JEM-2100, JEOL, and Japan) and atomic force microscopy (AFM, Dimension 3100, Veeco, USA) were performed to observe the size and morphology of CD-PEI. X-ray diffraction (XRD) measurements were carried out with a high-power X-ray diffractometer (Rigaku Co., D/MAZX 2500V/PC, Japan) from 10° to 50°. XPS (K-alpha, Thermo Fisher, USA) and FT-IR (Agilent, USA) were used for the characterization of functional groups. An element analyzer (Thermo Scientific, USA) was used to obtain weight percentages of carbon, hydrogen, nitrogen, and oxygen of CD-PEI.

Photoluminescence lifetime measurement. The exciton lifetime was determined by the time-correlated single photon counting (TCSPC) technique. The computer controlled diode

laser with 375 nm wavelength, 54 ps pulse width and 40 MHz repetition rate were used as an excitation source. The PL emission was spectrally resolved by using collection optics and a monochromator (PicoQuant, Germany). The TCSPC module (PicoHarp 300E, PicoQuant, Germany) with a MCP-PMT (R3809U-5x series, Hamamatsu, Japan) was used for ultrafast detection. The total instrument response function (IRF) for PL decay was less than 30 ps, and the temporal time resolution was less than 10 ps. The deconvolution of actual fluorescence decay and IRF was performed by using a fitting software (FlouFit, PicoQuant, and Germany) to deduce the time constant associated with each exponential decay.

Measurement of quantum yield (QY). The quantum yield is calculated using the slope of the line determined from the plot of the absorbance against the integrated fluorescence intensities as a comparative method. The QY (Q) can be calculated using the following equation (1):

$$Q = Q_R \left(\left(\frac{m}{m_R} \right) \left(\frac{n^2}{n_R^2} \right) \right)$$

Where m is the slope of the line obtained from the plot of the integrated fluorescence intensity versus absorbance. n

is the refractive index of solvent and the subscript R refers to the reference fluorophore of known quantum yield.

Loading capacity test and heparin polyanion competition assay.

Polyacrylamide gel electrophoresis (PAGE) analysis was performed to measure the loading capacity and heparin polyanion competition assay of siRNA/CD-PEI complex. The siRNAs at various concentrations (20–150 pmol) were incubated with 1 μg of CD-PEI in 20 μL PBS. After 1 h incubation, the gel was stained with SYBR gold staining reagent. For heparin polyanion competition assay, heparin (0–50 μg) were added to the siRNA/CD-PEI mixtures prior to gel electrophoresis to induce release of siRNA from CD-PEI.

RNase protection assay. PAGE analysis was carried out to estimate protection of siRNA against RNase mediated degradation in the presence of CD-PEI complex. RNase (25 μg) was first incubated with siRNA and siRNA/CD-PEI complex in 20 μL PBS for 1 h and gel electrophoresis and SYBR gold staining were performed.

Loading capacity test and heparin polyanion competition assay.

We prepared GFP-HeLa and MDA-MB-231 cells (1×10^4

cells/well) in a 96-well plate for 24 h, followed by incubation with various concentrations of CD-PEI or PEI with serum-containing media. After 12 h incubation, the cells were carefully washed with 1x PBS and then, CCK-8 assay solution with serum-free media were added and incubated for 1 h followed by measuring absorbance at 450 nm and 670 nm using a microplate reader (Molecular Devices, Inc., USA).

Cellular uptake study. The siRNA/CD-PEI complex prepared by using Cy5-siGFP and siVEGF (50 nM) was treated to GFP-HeLa and MDA-MB-231 cells in serum-free media in a 4-well glass plate for 12 h (final volume; 500 μ L). Then, cell media was replaced to serum-containing fresh media and cell images were obtained using a Ti inverted fluorescence microscope (Olympus, Japan) with 20x objective lens. For time-lapse fluorescence tracking of Cy5-siGFP and CD-PEI, GFP-HeLa cells were incubated with Cy5-siGFP/CD-PEI complex in serum-free media for 12 h in a 96-well plate (μ Clear® microplate, Greiner, Austria) (final volume; 50 μ L). The fluorescent signal in the cells was observed after changing media to serum-containing fresh media by using a

DeltaVision Elite and an IN Cell Analyzer2000 (GE Healthcare, USA) at various time points.

Flow cytometry. GFP-HeLa cells were treated with siGFP/CD-PEI complex in serum-free media for 12 h (final volume; 500 μ L, [siRNA] = 50 nM). Then, cell media was changed to serum-containing fresh media and incubated for 2 h. After washing with 1x PBS, the cells were collected after treatment of trypsin-EDTA for 3 min and then 10% FBS was added to the collected cells, followed by centrifugation (1,200 rpm, 3 min). The cells were finally washed with 1x PBS and the fluorescence of the cells was measured by a flow cytometer, FACS Canto (Beckton Dickinson, USA).

Semi-quantitative RT-PCR. MDA-MB-231 cells were seeded in a 12-well plate (1.2×10^5 cells/well). After 24 h incubation, the cells at 70~80% confluency were treated with siVEGF with Lipofectamine for 4 h, and siVEGF with PEI and with CD-PEI for 12 h in serum-free media (final volume; 500 μ L). Then, the cells were further incubated up to 48 h with serum-containing fresh media prior to functional evaluation.

To assess the immunostimulatory activities, CD-PEI and

siRNA/CD-PEI were treated to GFP-HeLa cells for 12 h, followed by washing and changing with fresh media. To boost the immune response as a control, poly I:C was treated for 6 h with lipofectamine.

For the semi-quantitative RT-PCR, total RNA was collected using Trizol reagent (Invitrogen, USA) and analyzed to measure the quantity and quality of the extracted RNA based on absorbance at 260 nm (A_{260}) and RNA/protein ratio (A_{260}/A_{280}) by using a UV-Vis spectrophotometer (Nanodrop Take3 or fluorometer (BioTek, USA)). Then, cDNA was synthesized from 800 ng of total RNA from MDA-MB-231 cells for VEGF gene downregulation and 700 ng of total RNA from GFP-HeLa cells for immune response through reverse transcription by using Superscript II reverse transcriptase (Invitrogen, USA) based on the manufacturer's protocol, followed by amplification by using a thermal cycler (BioRad, USA) and following primer pairs:

(1) VEGF forward primer: 5'-AGG AGG GCA GAA TCA TCA CG -3'

(2) VEGF reverse primer: 5'-CAA GGC CCA CAG GGA TTT

TCT-3'

(3) GAPDH forward primer: 5'-TTG TTG CCA TCA ATG
ACC CCT TCA TTG ACC-3'

(4) GAPDH reverse primer: 5'-CTT CCC GTT CTC AGC
CTT GAC GGT G-3'

(5) TLR3 forward primer: 5'-AGC CAC CTG AAG TTG ACT
CAG G-3'

(6) TLR3 reverse primer: 5'-CAG TCA AAT TCG TGC AGA
AGG C-3'

(7) INF- β forward primer: 5'-ACC AAC AAG TGT CTC CTC
CA-3'

(8) INF- β reverse primer: 5'-GAG GTA ACC TGT AAG
TCT GT-3'

(9) β -actin forward primer: 5'-GCT CGT CGT CGA CAA
CGG CTC-3'

(10) β -actin reverse primer: 5'-CAA ACA TGA TCT GGG
TCA TCT TCT-3'

The PCR reaction for VEGF was performed as follows: 2 min
at 94 °C, (20 s at 94 °C, 30 s at 60 °C, 30 s at 72 °C) \times 30
cycles. And the PCR reaction for GAPDH, used as

housekeeping gene, was performed as follows: 5 min at 94 °C, (30 s at 94 °C, 30 s at 60 °C, 30 s at 72 °C) × 26 cycles. The PCR reaction condition for TLR3 and INF- β was following: 5 min at 94 °C, (30 s at 94 °C, 30 s at 55 °C, 45 s at 72 °C) × 30 cycles. And the PCR reaction condition for β -actin was following: 5 min at 94 °C, (30 s at 94 °C, 30 s at 58 °C, 30 s at 72 °C) × 35 cycles. The products of PCR were analyzed by 1.2% TAE (Tris-acetate-EDTA) agarose gel retardation assay and the bands were confirmed by a Gel Doc (ATTO, Korea). Relative band intensities were quantified by using Image J software and VEGF gene expression level was normalized relative to GAPDH expression level.

In vivo study. All animal experiments were carried out in compliance with the Institutional Animal Care and Use Committees (IACUC) of Seoul National University. Balb/c male nude mice (5-weeks old) were purchased from ORIENT (Korea). Tumor-bearing xenograft mice were prepared by subcutaneous injection of GFP-HeLa cells (2×10^5 cells in 100 μ L of 1x PBS) to Balb/c male nude mice (6-weeks old). To monitor the change of fluorescence in tumors, we prepared

siGFP (1 nmol) with PEI and CD-PEI, and 1x PBS as a control in final volume of 100 μ L, then the suspensions were injected once every other day directly into tumors after tumor volume reached ~ 70 mm³, n=3. Fluorescence signals of GFP and Cy5 were monitored at designated time points (0, 2, and 4 days) by using optical molecular imaging system Optix MX3 (GE Healthcare Life Sciences, USA) at 490 and 650 nm excitation wavelength. The tumors were excised from the sacrificed mouse and the fluorescence of GFP and Cy5 were visualized by using optical molecular imaging system. To monitor the biodistribution of particles, FITC labelled CD-PEI in total volume of 100 μ L were introduced to tumor-bearing xenograft mice by intravenously (IV) injection (n=3). The green fluorescence arises from of CD-PEI in whole body and that of excised organs and tumors were obtained after injection of 24 h by using optical molecular imaging system Optix MX3 at 490 nm excitation wavelength. To investigate anti-tumor efficacy, we prepared siVEGF (1 nmol) with CD-PEI and CD-PEI, and 1x PBS as a control in final volume of 50 μ L, then the suspensions were injected intravenously at 0,

5, and 10 days after tumor volume of MDA-MB-231 implanted xenograft mice reached $\sim 60 \text{ mm}^3$, $n=4$. The changes of volume in tumors and body weight were monitored in each group over 14 days. The tumor volumes were calculated by using the equation of $\text{length} \times (\text{width})^2 \times 1/2$, where the length and width are the longest and shortest diameters (mm) of the tumor, respectively. The relative tumor volumes were calculated relative to the initial volumes.

Statistical analysis. P-value refers to statistical significance at least three independent experiment were determined based on the Student's t-test by using GraphPad Software.

3.2.3. Results and Discussion

CD-PEI was synthesized by dehydrating citric acid and PEI through microwave-assisted pyrolysis method. UV-Vis spectrum of CD-PEI in Fig. 3.17a showed two UV/Vis absorption peaks at 243 and 354 nm wavelength, corresponding to typical absorption of an aromatic moiety having sp^2 carbon network and the $n \rightarrow \pi^*$ transition of carbonyl groups, respectively.⁴² CD-PEI displayed a bright blue color under UV irradiation ($\lambda_{ex}=360$ nm) with an emission maximum at 450 nm (inset in Fig. 3.17a). The fluorescence emission spectra of CD-PEI showed an excitation wavelength dependency, similar to the previously reported CDs (Fig. 3.17b and Fig. 3.18a). The quantum yield (QY) of CD-PEI was measured as 18.8% by using quinine sulfate as a reference. The relatively high QY of CD-PEI might be due to surface passivation by PEI which could reduce the non-radiative recombination of localized electron-hole pairs through nucleophilic reaction between alkylamines of PEI and carboxylic/epoxy groups of CDs.⁴³ The exciton lifetime of CD-PEI was determined as 5.51 ns by the time-

correlated single photon counting (TCSPC) technique (Fig. 3.18b). The CD-PEI was highly stable in aqueous solution with a zeta-potential of +21.7 (\pm 0.43) mV at pH 7.4. The amount of conjugated PEI in CD-PEI was determined by measuring the UV/Vis absorbance of cuprammonium complex of CD-PEI at 630 nm, which yielded 29.8 wt% of PEI in CD-PEI.⁴⁴

FT-IR spectroscopy was next performed to characterize the functional groups on CD-PEI. The CD-PEI showed a broad peak at 3,394 cm^{-1} corresponding to O-H and N-H groups and peaks related to amide bond at 1,700 cm^{-1} (C=O stretching), 1,576 cm^{-1} (N-H in-plane), 1,389 cm^{-1} (C-N stretching) (Fig. 3.17c). X-ray photoelectron spectroscopy (XPS) revealed that CD-PEI contained carbon (C 1s, 284 eV), nitrogen (N 1s, 400 eV) and oxygen (O 1s, 532 eV). Deconvoluted high-resolution XPS spectrum of the CD-PEI (C 1s) showed peaks corresponding to C=C (284.1 eV), C-O (285.9 eV), C-N (286.9 eV), C=O (288.6 eV), COOH (290.1 eV) bonds (Fig. 3.17d). Elemental analysis revealed the composition of CD-PEI as C 49.73%, H 7.56%, N 11.37%, and

O 31.26%. Transmission electron microscopy (TEM) showed the diameter of CD-PEI ranging from 3 to 7 nm, with an average diameter of 5.1 ± 1.2 nm. The interlayer spacing of 0.21 nm agreed well with (100) facet of graphite (Fig. 3.17e and Fig. 3.18c).⁴⁵ The atomic force microscopy (AFM) line scans showed 5.8 nm of the topographic height of CD-PEI that matched well with observation from TEM analysis (Fig. 3.17f). The XRD pattern of CD-PEI in Fig. 3.18d displayed a broad peak centered at 0.42 nm.

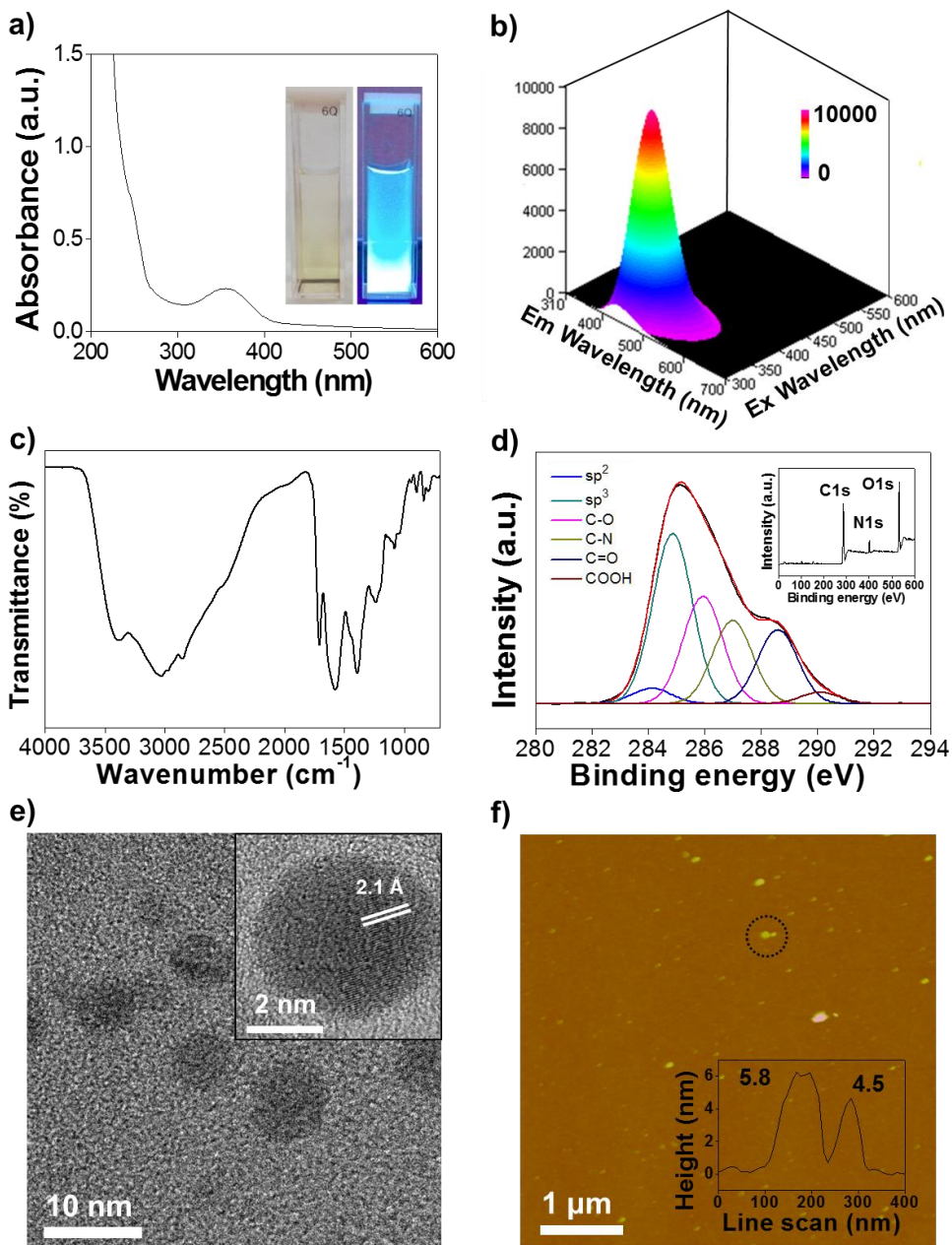


Figure 3.17. Characterization of CD-PEI. a) UV-vis absorption spectrum of CD-PEI. Inset shows a photo of the CD-PEI suspension (left) under ambient room light and (right) UV illumination at 360 nm. b) Three-dimensional fluorescence spectra of CD-PEI under varying excitation

wavelength from 300 to 800 nm with 10 nm increments. c) FT-IR spectrum of CD-PEI. d) Deconvoluted high-resolution XPS C 1s peak of CD-PEI with the survey XPS spectra of CD-PEI in the inset. e) TEM image of CD-PEI. Inset shows a representative image of single CD-PEI with lattice spacing of 0.21 nm. f) An AFM topography image of CD-PEI obtained under constant height contact scanning mode is shown with a line scan profile in the inset.

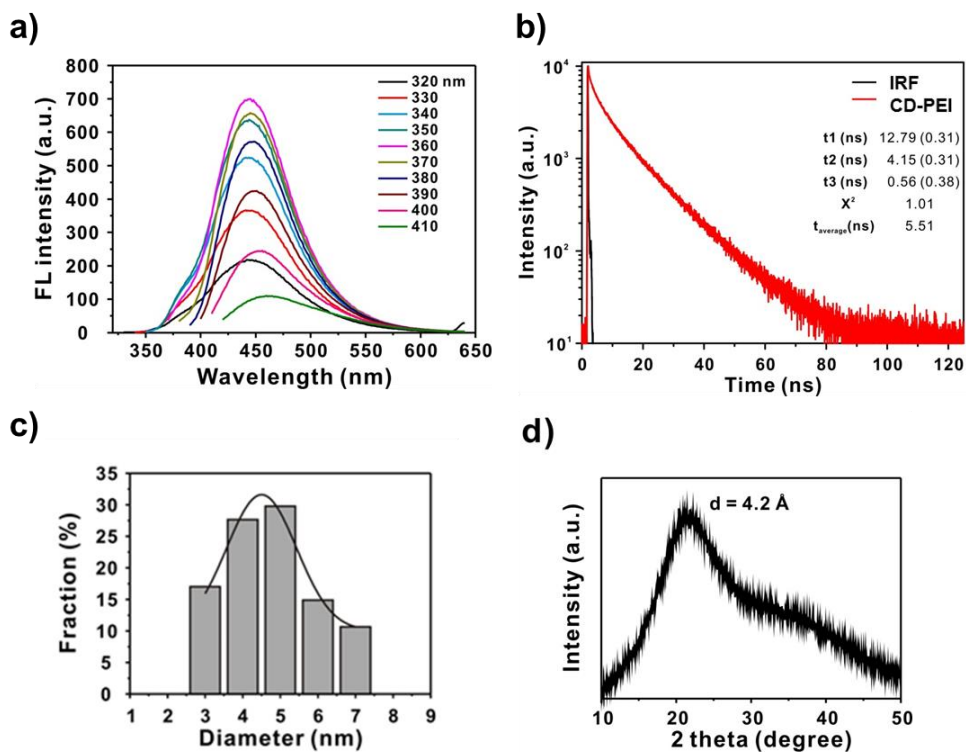


Figure 3.18. a) Photoluminescence spectra of CD-PEI. The excitation wavelength ranged from 320 to 410 nm with 10 nm increments as indicated. b) Time-resolved PL signal measured by time-correlated single photon counting (TCSPC) and exciton life time of CD-PEI. c) The size distribution histogram of CD-PEI d) XRD pattern of CD-PEI.

Prior to evaluation of gene knockdown efficiency, we measured siRNA loading capacity of CD-PEI. We first let the siRNA/CD-PEI complex formed by mixing CD-PEI and siRNA at various concentrations in phosphate buffered solution (1x PBS, pH 7.4) for 30 min at room temperature, and assessed the formation of siRNA/CD-PEI complex by polyacrylamide gel electrophoresis (PAGE) analysis. As described above, siRNA/CD-PEI complex was formed by electrostatic interaction between positive charges on the surface of PEI-passivated CD and negative charges on phosphate backbone of siRNA and the formed siRNA/CD-PEI complex was not expected to migrate towards positive end in PAGE due to increased size and reduced negative charge. The siRNA loading capacity of CD-PEI was estimated that 1 μg of CD-PEI was sufficient for loading of 100 pmol of siRNA and 50 pmol of Cy5-siRNA (Cy5 dye labelled siRNA) according to PAGE analysis (Fig. 3.19a and Fig. 3.20a)

Next, zeta-potential was measured to estimate the surface charge of the complex because the surface charges of the siRNA/CD-PEI complex could affect the cellular uptake

process and transfection efficiency.³³ After complexation of 1 μ g CD-PEI with 50 pmol siRNA and 50 pmol Cy5-siRNA, zeta-potential of CD-PEI was changed from +21.7 (\pm 0.4) to +3.4 (\pm 0.7) and +5.3 (\pm 0.4) mV at pH 7.4, respectively. Decrease in zeta-potential after siRNA treatment to CD-PEI suggested the successful complexation of siRNA to CD-PEI and the resulting positive zeta-potential of siRNA/CD-PEI complex implied the possibility of favorable interaction with the negatively charged cell surface to promote its cellular uptake. DLS analysis also showed the increase of size distribution after complexation in buffered condition (Fig. 3.20c). Taken together, zeta-potential, PAGE analysis, and DLS data suggested the successful formation of the siRNA/CD-PEI complex.

To achieve successful siRNA delivery and efficient target gene knockdown, siRNA should be released from the CD-PEI in cell cytoplasm to induce RNAi and degrade target mRNA. Heparin has been utilized in medical area as an anticoagulant as well as a reagent to release anionic oligonucleotide from cationic NPs functioning as a polyanionic polymer in vitro.¹⁸

Therefore, we carried out the heparin competition assay to investigate the release of siRNA from the CD-PEI upon addition of heparin. Fig. 3.19b showed that band intensities corresponding to the released siRNA increased dose-dependently with treatment of heparin up to 50 μg whereas the band was not observed in the absence of heparin, suggesting conditional release of siRNA from CD-PEI.

We next performed the in vitro ribonuclease (RNase) protection assay to investigate whether siRNA in the siRNA/CD-PEI complex maintains its chemical structure in the presence of RNase under physiological environment. For efficient gene silencing, it is necessary to maintain the chemical stability of siRNA in the siRNA/CD-PEI complex under biological environment until the complex reaches to target site.⁶ Aqueous solutions of free siRNA and siRNA/CD-PEI complex were prepared, and incubated with RNase (25 μg) in 20 μL PBS solution for 1 h at 37 $^{\circ}\text{C}$. PAGE analysis was then performed after post-incubation with heparin (50 μg) for 10 min. As shown in Fig. 3.19c and Fig. 2.20b, intense siRNA band was observed even after treatment of RNase, suggesting

protection of siRNA from RNase mediated degradation in the presence of CD-PEI. In contrast, free siRNA was completely degraded by RNase under same experimental condition. The complexation between siRNA and PEI at the surface of CD provided protection for siRNA against nuclease degradation, which might give little chance for interaction between RNase and siRNA/CD-PEI complex through steric hindrance effect and low electrostatic interaction. This result was in good agreement with previous studies of PEI-passivated or complexed NPs⁴⁶ and indicates that CD-PEI may serve as an efficient siRNA delivery carrier because it effectively condenses with siRNA and protects the adsorbed siRNA from enzymatic cleavage mediated by RNase.

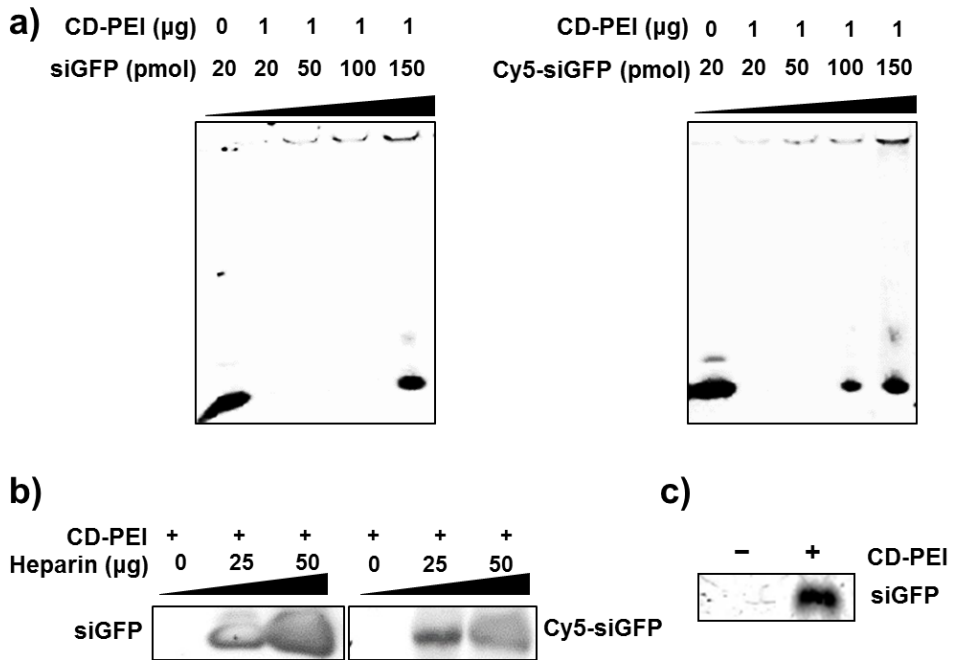


Figure 3.19. PAGE analysis to investigate siRNA loading to CD-PEI. a) Mixed solutions of CD-PEI with siGFP and Cy5-siGFP at various concentrations were prepared and loaded for PAGE. Gel image suggested that maximum siRNA loading could be achieved using ~ 150 and ~ 100 pmol of siGFP and Cy5-siGFP, respectively, towards $1 \mu\text{g}$ of CD-PEI. b) PAGE analysis was performed after heparin was added to mixtures of CD-PEI/siRNA. Polyanion competition assay revealed that the loaded siRNA to CD-PEI could be released from CD-PEI upon treatment of polyanionic heparin. c) Gel image showed that RNase-mediated siRNA degradation was inhibited in the presence of CD-PEI. In contrast, free siRNA without CD-PEI was completely degraded upon addition of RNase.

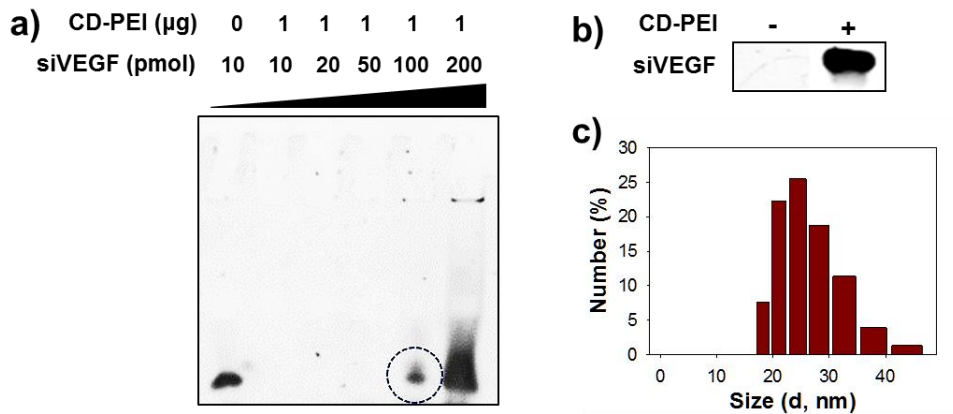


Figure 3.20. PAGE analysis was carried out to measure a) loading capacity of siVEGF to CD-PEI and b) RNase protection assay. Similar to siGFP, siVEGF was also protected from RNase mediated degradation in the presence of CD-PEI. c) DLS analysis for size distribution of siRNA/CD-PEI complex in pH 7.0 buffered condition.

To be practically useful siRNA delivery vehicle, low cytotoxicity is an essential prerequisite. Therefore, we measured viability of mammalian cells, HeLa and MDA-MB-231 cells, after treatment of CD-PEI with various concentrations for 12 h by using CCK-8 cell viability assay kit. It is well known that PEI exhibits cytotoxicity induced from cell membrane damage by highly positive charges of PEI. Therefore, wide applications of PEI itself to gene delivery have been restricted especially in biomedical applications which deal with in vivo applications.^{47,48} In contrast to PEI itself, CD-PEI showed notably lower cytotoxicity (Fig. 3.21). More than 90% of cells were viable under all concentration ranges of CD-PEI we treated. We used maximum concentration of CD-PEI of 50 µg/ml throughout the present study, which ensures more than 90% of cell viability. We assume that CD-PEI reduces the toxicity of PEI because the density of amine groups presenting positive charges of PEI decreased during the passivation process of CD while maintaining its net positive charge.^{49,50} In addition, reduced degree of freedom of flexible PEI polymer in CD-PEI may

decrease number of positively charged functional groups of PEI that can interact with cell surface, resulting in lower cytotoxicity.

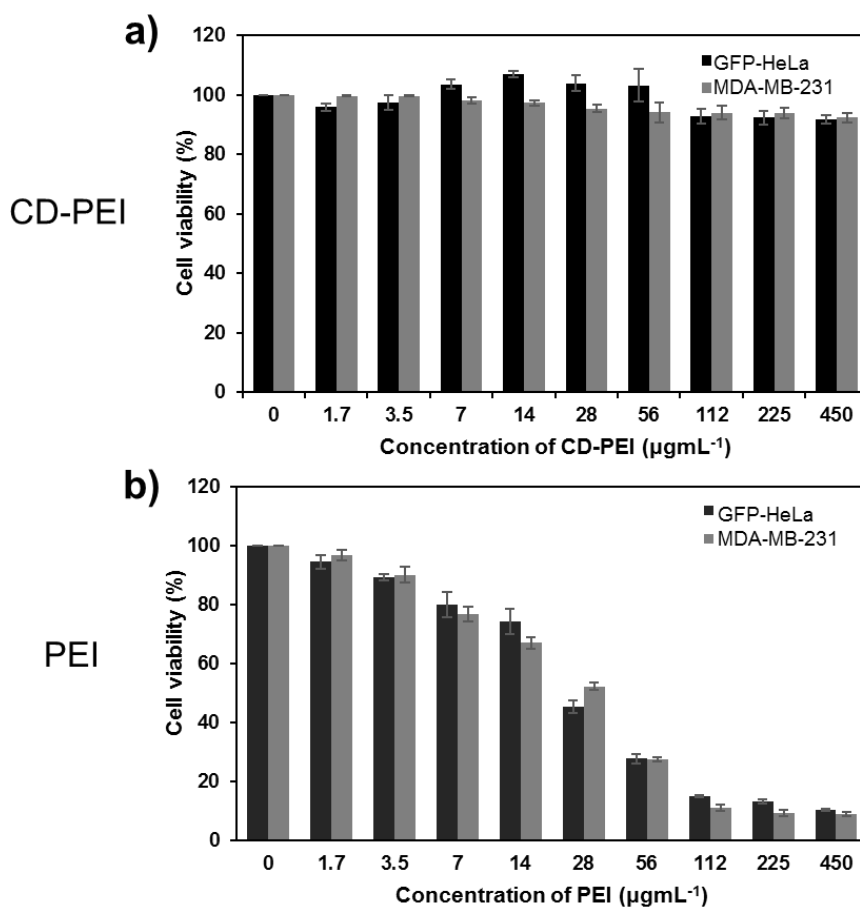


Figure 3.21. Viability of GFP-HeLa and MDA-MB-231 cells were measured after treatment of a) CD-PEI and b) free PEI at different concentrations for 12 h by CCK-8 assay.

In accordance with previous researches that proved the endocytosis of PEI NPs and PEI-complexed NPs, the fluorescent CD-PEI is expected to enable cellular imaging of the endocytosed siRNA/CD-PEI complex in cytoplasm and monitoring of the dissociation of the siRNA from the delivery vehicle if dye-labelled siRNA is employed. After we confirmed that the major optical characteristics of CD-PEI remained unaffected after formation of Cy5-siRNA/CD-PEI (Fig. 3.22) and untraceable intracellular localization of Cy5-siRNA by treating it alone to cells, we investigated the cellular uptake and the intracellular localization of the siRNA/CD-PEI complex inside cell cytoplasm. We used Cy5-conjugated siRNA targeting GFP (Cy5-siGFP) and HeLa cells constitutively expressing green fluorescent protein (GFP) (GFP-HeLa). After treatment of siGFP/CD-PEI complex to GFP-HeLa cells for 12 h, the Cy5-siGFP/CD-PEI complex was visualized in GFP-HeLa cells by monitoring the blue and red fluorescence originated from CD-PEI (= 370/443 nm) and Cy5-siGFP ($\lambda_{\text{ex}}/\lambda_{\text{em}} = 650/670$ nm), respectively. Cell images in Fig. 3.23a and Fig. 3.24 showed fluorescence

corresponding to Cy5-siGFP (red) and CD-PEI (blue) in cytoplasm. We observed that the inherent green fluorescence ($\lambda_{\text{ex}}/\lambda_{\text{em}} = 495/521 \text{ nm}$) from GFP-HeLa cells significantly decreased, indicating that GFP expression was downregulated by siGFP targeting GFP mRNA. Bio-TEM image of the GFP-HeLa cells treated with siGFP/CD-PEI also exhibited the endocytosed CD-PEI around perinuclear region in cell cytoplasm with a little increase in size (Fig. 3.23b).^{51,52} It is well known that the aggregation of the PEI-complexed NPs and PEI-oligonucleotide was reduced under low pH condition because of electrostatic repulsive interaction between complex.^{53,54} In the present study, CD-PEI exhibited smaller overall size at low pH. (Fig. 3.25). Even though the size of the complex seemed to be slightly increased at pH 7.0 buffered solution by aggregation, we think that the proton-sponge effect accelerated the stable dispersion through decrease of aggregation at pH 5.0 of buffered solution (Fig. 3.25)

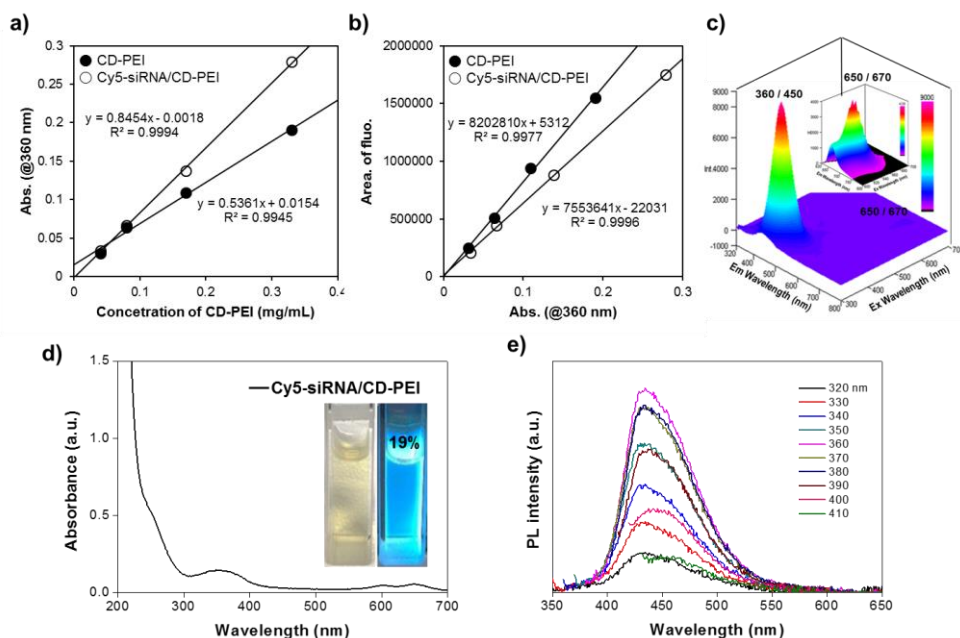


Figure 3.22. a,b) The Quantum yield of CD-PEI (18.8%) and Cy5-siRNA/CD-PEI (19.5%) were measured at 360 nm excitation wavelength. a) Absorbance corresponding to CD-PEI concentration with and without Cy5-siRNA. b) Area of fluorescence versus absorbance value for measuring the quantum yield of CD-PEI. c) Three-dimensional fluorescence spectra of Cy5-siRNA/CD-PEI under varying excitation wavelength from 300 to 700 nm with 10-nm increments. Inset spectra is fluorescence spectra of Cy5-siRNA/CD-PEI under varying excitation wavelength from 600 to 700 nm with 10-nm increments. d) Absorption spectrum of Cy5-siRNA/CD-PEI. Inset image show the PL of CD-PEI with UV light. e) Photoluminescence spectra of Cy5-siRNA/CD-PEI. The excitation wavelength ranged from 320 to 410 nm with 10 nm increments as indicated.

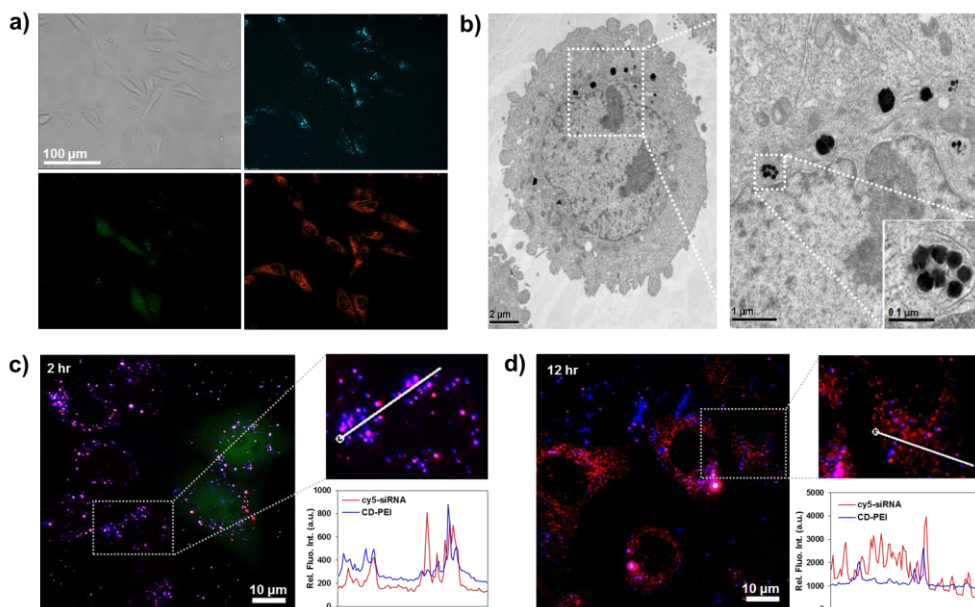


Figure 3.23. a) Fluorescent images of GFP–HeLa cells treated with Cy5–siGFP/CD–PEI (blue: CD–PEI, green: GFP, and red: Cy5–siGFP). b) TEM images of GFP–HeLa cells treated with CD–PEI showed the presence of the internalized CD–PEI in cytoplasm. c), d) Fluorescence signals of Cy5–siGFP and CD–PEI in the cytoplasm of GFP–HeLa cells treated with Cy5–siGFP/CD–PEI. Fluorescence intensities were measured along with line scan profile in living cells. After 12 h incubation of the GFP–HeLa cells treated with siGFP/CD–PEI, fluorescence corresponding to Cy5–siGFP was hardly co-localized with blue fluorescence corresponding to CD–PEI d) whereas Cy5–siGFP fluorescence was mostly overlapped with CD–PEI fluorescence at 2 h post–incubation c), implying that Cy5–siGFP become released from its delivery carrier, CD–PEI, overtime in cytoplasm.

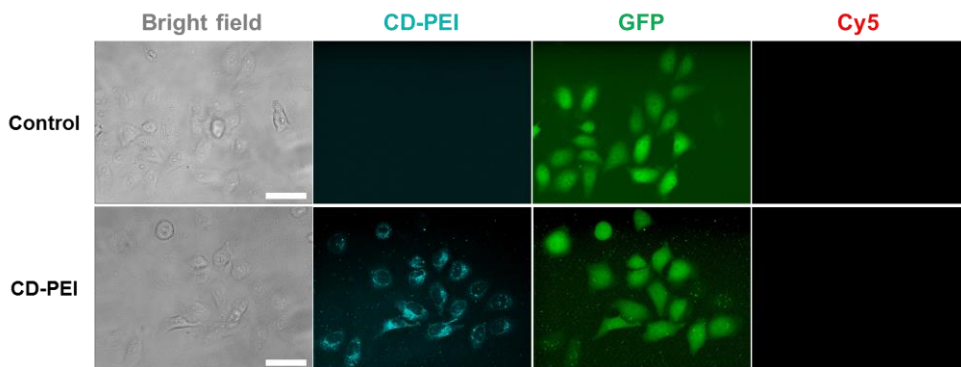


Figure 3.24. Fluorescent images of GFP-HeLa cells treated with CD-PEI (blue: CD-PEI, green: GFP, and red: Cy5-siGFP).

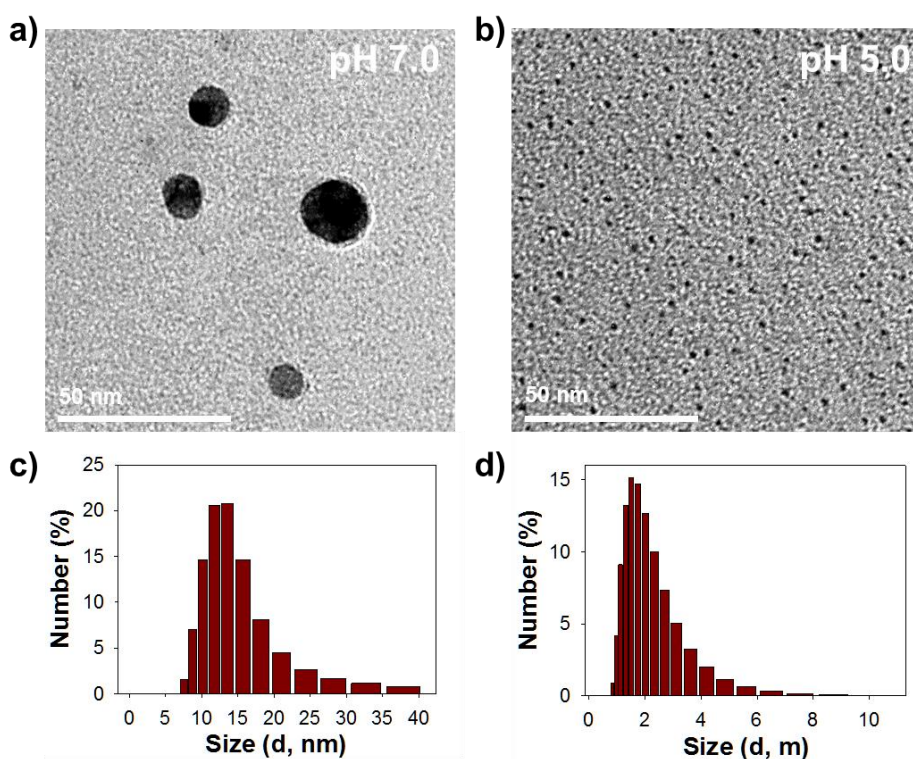


Figure 3.25. TEM image and DLS data of CD-PEI in buffered solution a), c) pH 7.0 and b), d) pH 5.0.

To more precisely investigate release kinetics of siRNA from CD-PEI complex corresponding to the time-dependent distribution of the CD-PEI and Cy5-siGFP inside cell cytoplasm, the fluorescence signals were observed in living cells at various time points after the Cy5-siGFP/CD-PEI complex treatment (Fig. 3.23c,d and Fig. 3.26). After 2 h of incubation, pinkish purple fluorescence was observed in cell cytoplasm, of which color was derived from merging of blue and red fluorescence, indicating that Cy5-siGFP/CD-PEI complex remained intact without notable siRNA release after cellular uptake at this early time point. However, during further incubation, blue and red fluorescence signal was separated from each other in cytoplasm, suggesting the release of Cy5-siGFP from CD-PEI in cell cytoplasm over time.⁵⁵ Taken together, the time dependent bioimaging based on the highly fluorescent CD was successfully demonstrated in live cells without notable cytotoxicity.

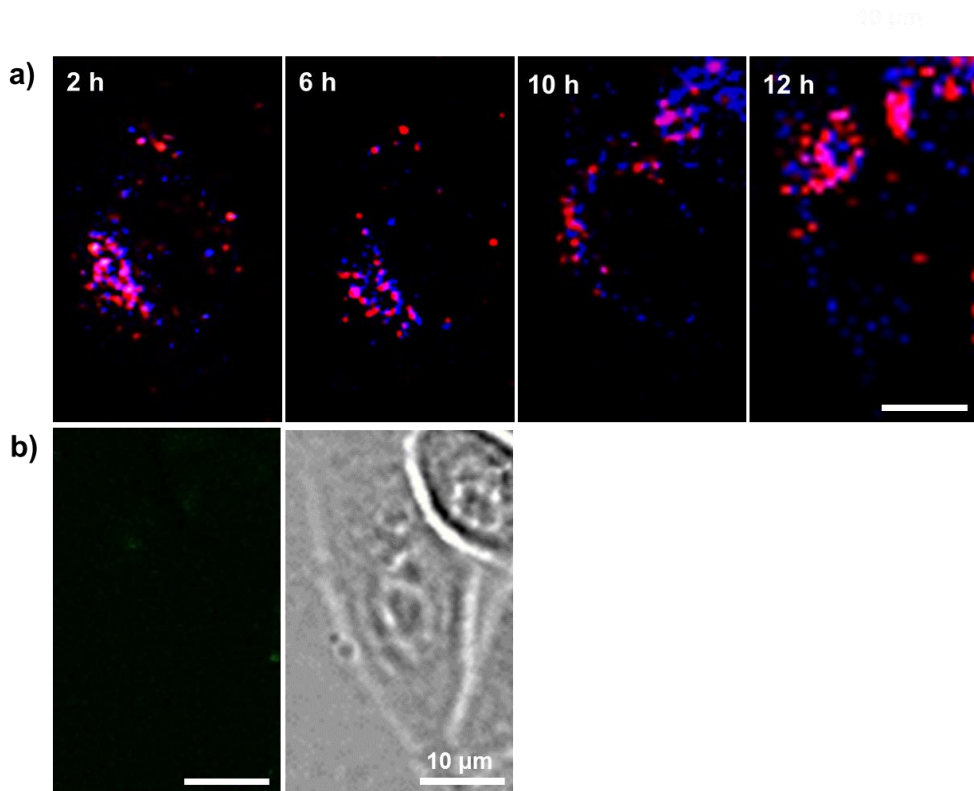


Figure 3.26. Fluorescent images of GFP-HeLa cells treated with Cy5-siRNA/CD-PEI complex were obtained at different time points after incubation. a) Each fluorescence signal of Cy5-siRNA and CD-PEI was gradually separated from each other over time (0 – 12 h) in cytoplasm. (blue: CD-PEI, red: Cy5-siRNA) b) Left image was obtained under GFP fluorescence channel and right image is the corresponding bright field image. Images in b) show the almost completely down-regulated GFP expression due to the siRNA-mediated target gene suppression.

Next, we quantitatively evaluated the knockdown of GFP expression induced by siGFP/CDPEI in GFP–HeLa cells. GFP–expressing HeLa cells were first treated with 50 nM of siGFP/CD–PEI in a 12–well plate for 12 h. Lipofectamine (Lipo) and PEI were used as controls. At 48 h of post–transfection, cell media was removed and replaced with fresh serum–containing media. Then, relative GFP expression levels were estimated by observing fluorescent images of the cells using a fluorescence microscope and flow cytometry. Images in Fig. 3.27a and Fig. 3.28 showed notable decrease in green fluorescence in GFP–HeLa cells treated with siGFP/Lipo and siGFP/CD–PEI compared to the HeLa cells treated with PEI, Lipo, and CD–PEI only. Fig. 3.27b showed the flow cytometry histograms to show cell populations versus green fluorescence intensity. To more precisely analyze the data, we divided the histograms into two regions—M1 and M2, respectively indicating low and high green fluorescence intensities of GFP compared to untreated cells (control), and mean fluorescence in each region was calculated and presented in a bar–graph in Fig. 3.27c. It is

notable that the cells treated with siGFP/CD-PEI showed most significant decrease in mean GFP fluorescence both in M1 and M2. Overall mean fluorescence of GFP based on both M1 and M2 also supported most efficient GFP knockdown in the cells treated with siGFP/CD-PEI (Fig. 3.27d). The mean green fluorescence significantly decreased in the cells treated with siGFP/CD-PEI down to 34.0% relative to untreated control, compared to those with siGFP/Lipo (59.7%) and siGFP/PEI (51.1%). It is notable that CD-PEI mediated siGFP delivery showed higher gene silencing than Lipo as well as higher cell viability (92.3%) compared to Lipo (77.3%) and PEI (75.3%) (data not shown). Lipo and PEI are well-known as popular non-viral gene transfection agent but they exhibit high cytotoxicity at effective concentrations and/or long time treatment. Collectively, the data suggest that CD-PEI is more efficient siRNA delivery vehicle with lower cytotoxicity compared to Lipo and PEI.

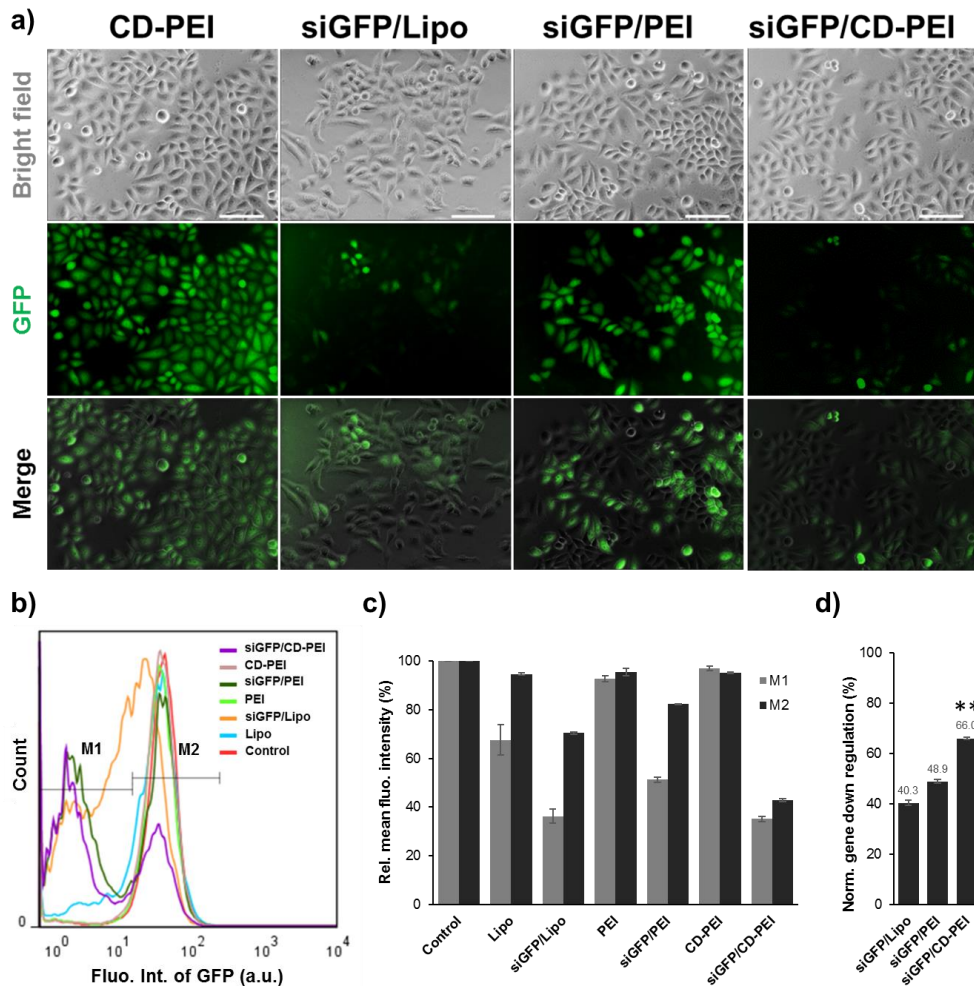


Figure 3.27. Down-regulation of GFP gene expression by using siGFP/CD-PEI complex. a) Fluorescence microscope images of GFP-HeLa cells treated with siGFP/CD-PEI were obtained at 12 h post-incubation. b) Mean fluorescence of GFP expression in the GFP-HeLa cells were quantitatively measured by flow cytometry. M1 and M2 indicate two populations of cells expressing GFP at different degree due to significant suppression of GFP expression (M1) and little or no down-regulation of GFP expression (M2). c) Relative GFP

fluorescence level and d) relative GFP gene down-regulation observed from flow cytometry measurement in b) were presented in bar graphs. Scale bar is 100 μm . P-values were calculated by Student's t-test: ** for $p < 0.01$, $n = 3$.

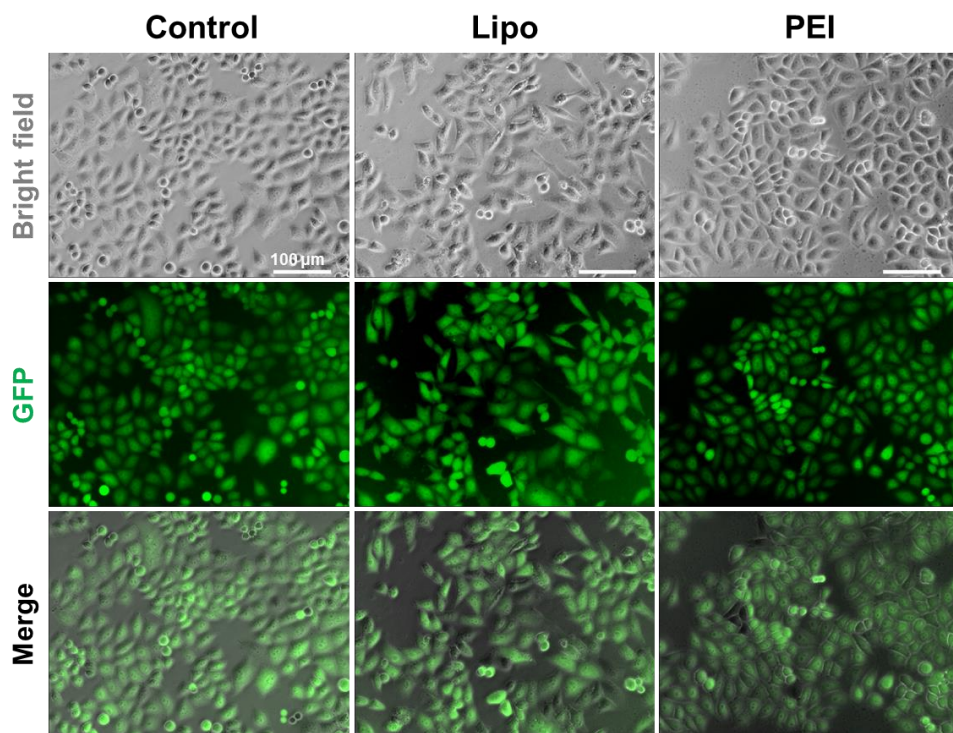


Figure 3.28. Images of control GFP-HeLa cells treated with Lipo only and PEI only. Without siGFP, only Lipo or PEI cannot silence GFP gene expression.

Next, we investigated down-regulation of vascular endothelial growth factor (VEGF) gene expression by using siRNA sequence designed to target VEGF (siVEGF). VEGF plays a pivotal role in tumor growth, inducing angiogenesis by activation of endothelial cells through binding to the VEGF receptor and subsequent signal cascade.^{56,57} Therefore, the inhibition of VEGF expression has been one of the important strategies in gene therapy for treating various cancers. We evaluated the knockdown of VEGF gene expression at mRNA level induced by siVEGF in complex with CD-PEI after monitoring the fluorescence from uptaken CD-PEI to the cells (Fig. 3.29). MDA-MB-231, breast cancer cell, was incubated with 50 nM of siVEGF/CD-PEI complex for 12 h. At 48 h of post-transfection, cell media was removed and replaced with fresh serum-containing media. Then, the VEGF gene expression level was estimated by semi-quantitative reverse transcription polymerase chain reaction (RT-PCR). Band intensities of VEGF gene in gel electrophoresis were normalized with respect to a housekeeping gene, glyceraldehyde 3-phosphate dehydrogenase (GAPDH). As

shown in Fig. 3.30, RT-PCR results showed similarly efficient gene silencing of the VEGF gene by siVEGF/CD-PEI complex down to 32.2% and by siVEGF/Lipo down to 32.9%. Under the same conditions omitting siVEGF, cell viability was slightly reduced to 94.6% after treatment of CD-PEI whereas the Lipo treatment induced notable decrease in the cell viability down to 70.0%. Collectively, these data indicated that CD-PEI could be an efficient siRNA delivery carrier for siVEGF to silence therapeutically relevant VEGF gene expression in addition to siGFP for knockdown of a model gene, GFP. The CD-PEI mediated siRNA delivery and knockdown of the target gene were successfully demonstrated in two different cancer cell lines—HeLa and MDA-MB-231.

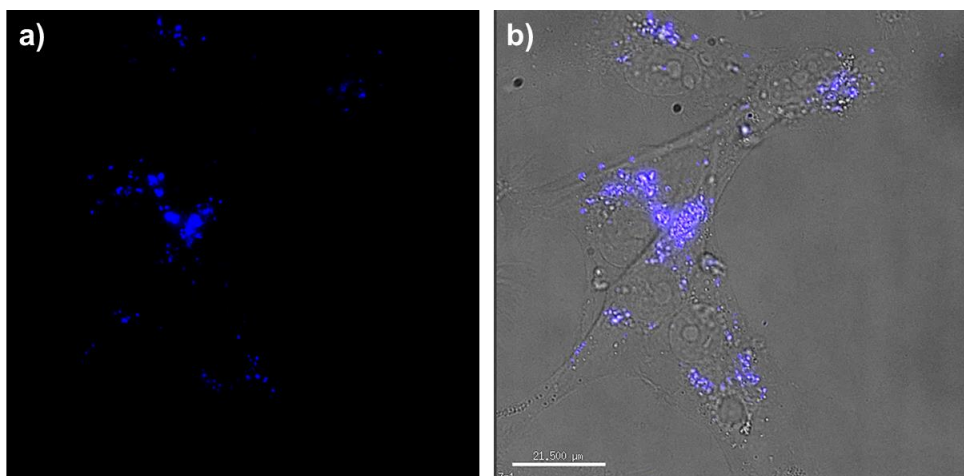


Figure 3.29. Fluorescence images of MDA-MB-231 cells treated with CD-PEI (50 µg/ml). a) Blue fluorescence of CD-PEI was observed in perinuclear region of MDA-MB-231 cells. b) Bright field image was merged with fluorescent image of CD-PEI in the cells.

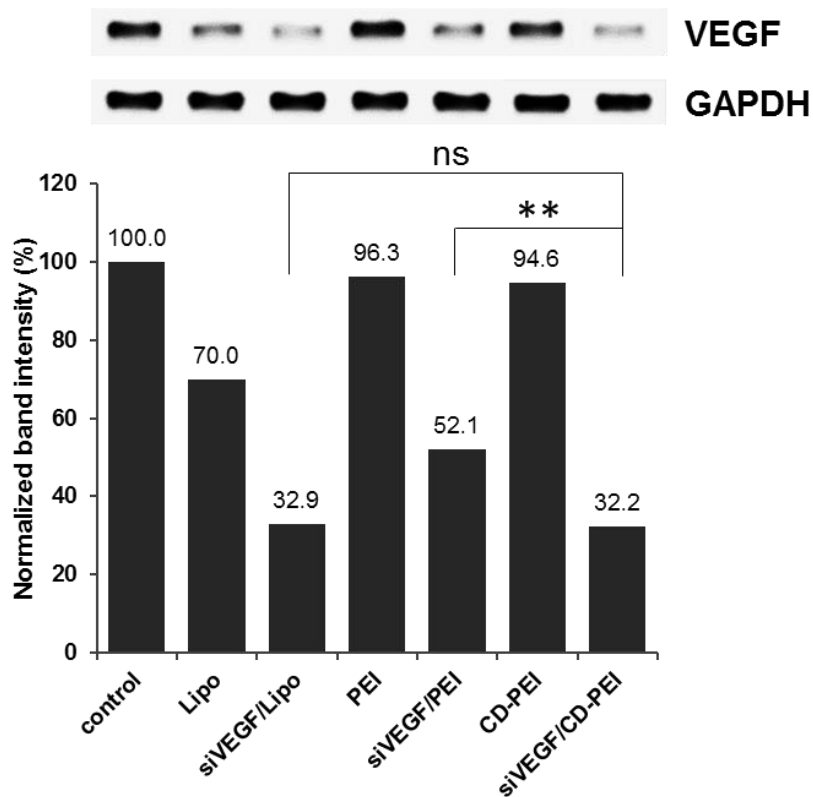


Figure 3.30. Expression level of VEGF and GAPDH of MDA-MB-231 cells. Gene expression levels were evaluated by semi-quantitative RT-PCR and gel electrophoresis. P-values were calculated by Student's t-test: ** for $p < 0.01$, $n = 3$.

With consideration for possibility of unexpected immune responses in gene delivery system, we investigated the immunostimulatory properties of CD-PEI and siRNA/CD-PEI complex. It is reported that Toll-like receptor 3 (TLR3) recognizes double-strand RNA (dsRNA) and induces type I interferon (IFN) by activating a variety of signal pathways including production of cytokine/chemokine and activation of NF- κ B and MAP kinases.⁵⁸⁻⁶⁰ Thus, investigating the masking ability of CD-PEI against potential immune response activatable by siRNA introduction is important. We prepared GFP-HeLa cells treated with CD-PEI, siRNA/CD-PEI, and poly I:C (P/C) as a control. The expression levels of TLR3 and IFN- β were measured by RT-PCR and gel electrophoresis. As shown in Fig. 3.31, induction of TLR3 and activation of INF- β were hardly observed in CD-PEI and siRNA/CD-PEI treated cells. Overall, the data suggests that CD-PEI can mask the immune responses activatable by siRNA without immunostimulatory property itself in vitro.

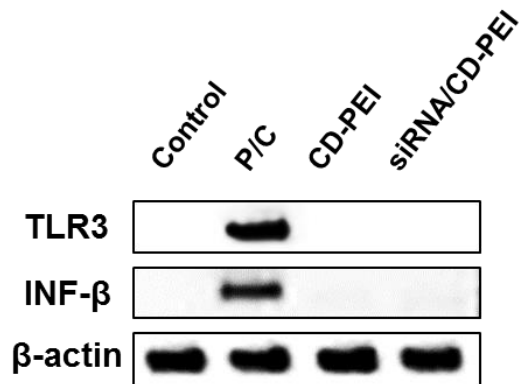


Figure 3.31. Band images for assessment of the immunostimulatory properties of CD-PEI in GFP-HeLa cells. No induced production of TLR3 and activation of INF-β was observed in CD-PEI and siRNA/CD-PEI treated cells. Poly I:C was treated as positive control (P/C).

Encouraged by successful demonstration in cultured cancer cell in vitro, we finally investigated the applicability of CD-PEI based siRNA delivery system in a mouse model. First, tumor-bearing xenograft mice were prepared by subcutaneous injection of GFP-HeLa cells and then, siGFP was intratumorally introduced in complexed with PEI or CD-PEI. Green fluorescence of GFP in tumor treated with siGFP/CD-PEI was significantly decreased compared to

tumor treated with siGFP/PEI, PEI, CD-PEI, and free siGFP (Fig. 3.32a). The decrease of green fluorescence signal was also observed in tumor treated with siGFP/CD-PEI excised from the sacrificed mouse. The red fluorescence from free Cy5-siGFP treated tumor was totally disappeared because of degradation and removal of Cy5-siGFP. However, the Cy5 fluorescence signal from the Cy5-siGFP/CD-PEI treated tumor was partially remained (Fig. 3.32b).

We next investigated the biodistribution of CD-PEI following systemic administration with consideration for further in vivo application. Fluorescence from CD-PEI was monitored in HeLa tumor-bearing xenograft mice by whole body imaging and then, major organs were excised from the mice. The fluorescence signals corresponding to CD-PEI were strongly observed in tumor and slightly visible in intestine, liver, and spleen, showing the correlation of distribution of nanoparticles⁶¹⁻⁶³ and tumor-specific accumulation (Fig. 3.33). It is well known that drug carriers in a size range from 10 to 100 nm are allowed to escape from the circulation owing to the inherent leakiness and the

enhanced permeability of the underdeveloped tumor vasculature.⁶⁴ Our siRNA delivery system took advantages of the enhanced permeability and retention (EPR) effect due to well-suited size distribution of the siRNA/CD-PEI complex (Fig 3.20c and Fig. 3.23b).

Finally, we investigated the anti-tumor capability of siRNA/CD-PEI complex against human cancer xenograft via intravenous (IV) injection of the siVEGF/CD-PEI complex. Each tumor was generated and grown up to 60 mm³ in volume, and then treated with CD-PEI, free siVEGF, siVEGF/CD-PEI, and 1x PBS by IV injection. The changes of tumor volume in each group were monitored for 14 days and the relative tumor volumes were measured comparing to the initial volumes. As shown in Fig. 3.32c, tumor growth in the siVEGF/CD-PEI treated group was significantly inhibited. However, the mice treated with CD-PEI only and free siVEGF showed no notable difference in tumor size compared to the control 1x PBS treated group, supporting that anti-tumor activity through RNAi in tumor was strongly enhanced by CD-PEI mediated siRNA delivery without any deleterious effect of CD-PEI

itself and protection effect of CD-PEI against degradation of siRNA. Statistically significant difference was shown from the tumors between siVEGF/CD-PEI treated group and other groups. Taken together, CD-PEI mediated functional siRNA delivery system was successfully demonstrated in vivo mouse model, showing the remarkable gene knockdown efficacy and siRNA protection from degradation in vivo.

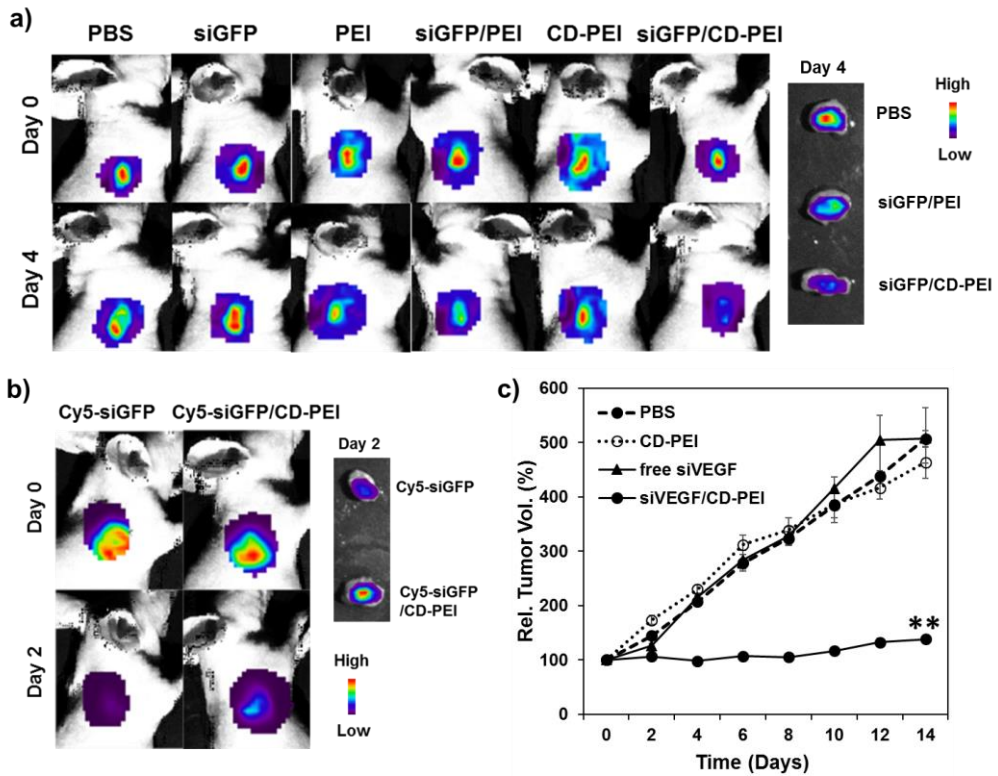


Figure 3.32 GFP knockdown and tumor growth inhibition in vivo. a) Green fluorescence was monitored from tumors in GFP-HeLa xenograft bearing mouse. Significant decrease of GFP fluorescence was observed in the siGFP/CD-PEI treated tumor compared to those treated with siGFP/PEI and free siGFP. b) Red fluorescence originated from cy5-siGFP was observed from tumors. The Cy5 fluorescence from free Cy5-siGFP treated tumor was totally disappeared because of degradation and removal of Cy5-siGFP whereas the corresponding signal from the Cy5-siGFP/CD-PEI treated tumor was notably high. c) Relative tumor volumes measured over 14 days after the MDA-MB-231 tumor-bearing mouse were treated with PBS, CD-PEI, free siVEGF, and

siVEGF/CD-PEI intravenously three times (0, 5, and 10 days). P-values were calculated by student's t-test, ** for $p < 0.01$, $n = 4$.

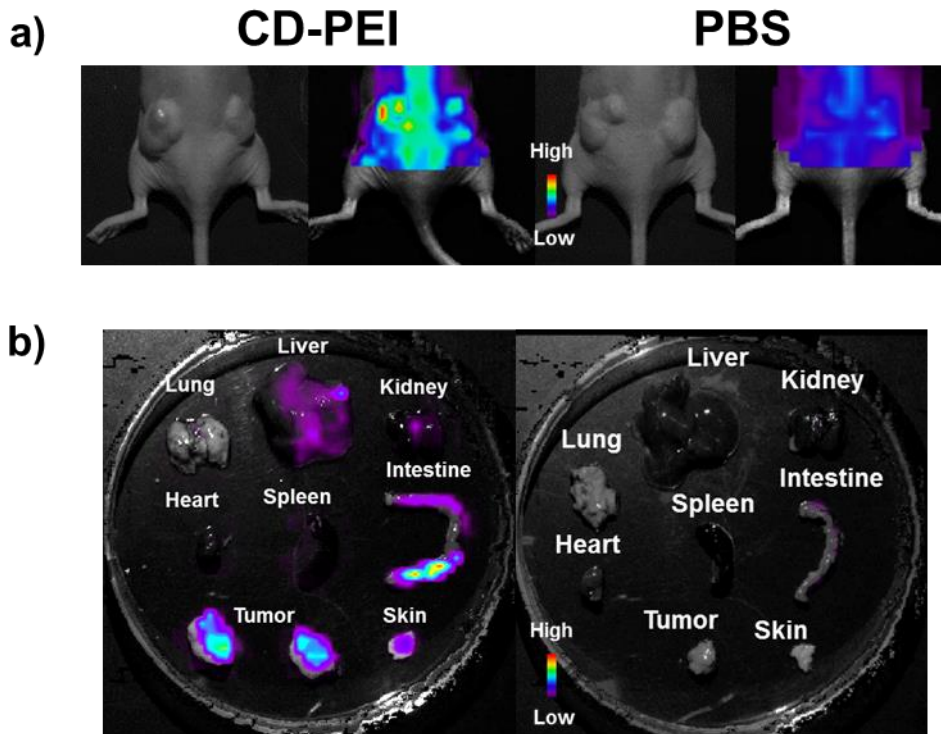


Figure 3.33. a) Bright field and fluorescence image ($\lambda_{\text{ex}} = 490$ nm) of HeLa tumor-bearing xenograft mice were obtained after 24 h of IV injection of CD-PEI (left) and PBS (right). b) Ex vivo fluorescence images of major organs of mice. The fluorescent signals corresponding to CD-PEI ($\lambda_{\text{ex}} = 490$ nm) from major organs, tumor, and skin were observed after 24 h of IV injection of CD-PEI (left). No fluorescence signals were observed in organs and tumor of PBS introduced mice (right).

3.2.4. Conclusion

In this study, we developed an efficient siRNA delivery system by using CD-PEI and demonstrated that the siRNA/CD-PEI complex was successfully harnessed to knockdown GFP and VEGF gene expression in vitro and in vivo. In addition, the intracellular distribution of CD-PEI with siRNA was monitored based on intense fluorescence of CD-PEI itself over time. The present CD-PEI based siRNA delivery system possesses many advantages for biomedical applications. First, the present CD-PEI based strategy is technically simple to prepare because CD-PEI is directly synthesized from a mixture of citric acid and PEI by using a household microwave and reaction time is only 2 min. Second, the CD-PEI simultaneously enabled both efficient target gene silencing by delivering siRNA into cells and convenient intracellular trafficking of gene delivery vehicle based on fluorescence of CD-PEI itself without requiring conjugation of fluorescent dyes to the nanoparticle. In the present study, PEI played multiple important roles as carbon source with citric acid for CD formation in addition to surface passivation agent

to enhance CD fluorescence and condensing layer for siRNA.

Although several approaches of drug delivery systems using CD NPs were reported, systemic introduction of the CD therapeutic complex in vivo for tumor-specific treatment has still remained as challenge to date. In this regard, the present work is first demonstration of CD based RNAi approach both in vitro and in vivo with high gene knockdown efficacy and bio-molecular imaging capability achieved by systemic intravenous administration. We expect that the present siRNA delivery platform can be useful addition to current siRNA delivery systems, enabling highly effective and modular gene silencing with simultaneous bioimaging capability. In addition, due to relatively low cytotoxicity and immunostimulatory property, the CD-PEI based siRNA delivery strategy can be readily applicable for gene therapy in the near future.

3.2.5. References

1. Hamilton, A. J.; Baulcombe, D. C. *Science* **1999**, 286, 950.
2. Elbashir, S. M.; Harborth, J.; Lendeckel, W.; Yalcin, A.; Weber, K.; Tuschl, T. *Nature* **2001**, 411, 494.
3. Fire, A.; Xu, S.; Montgomery, M. K.; Kostas, S. A.; Driver, S. E.; Mello, C. C. *Nature* **1997**, 391, 806.
4. Nykänen, A.; Haley, B.; Zamore, P. D. *Cell* **2001**, 107, 309.
5. Martinez, J.; Patkaniowska, A.; Urlaub, H.; Lührmann, R.; Tuschl, T. *Cell* **2002**, 110, 563.
6. Dorsett, T.; Tuschl, T. *Nat. Rev. Drug Discovery* **2004**, 3, 318.
7. Djiane, A.; Yogev, S.; Mlodzik, M. *Cell* **2005**, 121, 621.
8. Bumcrot, D.; Manoharan, M.; Koteliansky, V.; Sah, D. W. *Nat. Chem. Biol.* **2006**, 2, 711.
9. Soutschek, J.; Akinc, A.; Bramlage, B.; Charisse, K.; Constien, R.; Donoghue, M.; Elbashir, S.; Geick, A.; Hadwiger, P.; Harborth, J.; John, M.; Kesavan, V.; Lavine, G.; Pandey, R. K.; Racie, T.; Rajeev, K. G.; Röhl, I.; Toudjarska, I.; Wang, G.; Wuschko, S.; Bumcrot, D.; Koteliansky, V.; Limmer, S.; Manoharan, M.; Vornlocher, H. *Nature* **2004**, 432, 173.
10. Dykxhoorn, D. M.; Palliser, D.; Lieberman, J. *Gene Ther.* **2006**, 13, 541.
11. Dykxhoorn, D. M.; Lieberman, J. *Annu. Rev. Biomed. Eng.* **2006**, 8, 377.
12. Whitehead, K. A.; Langer, R.; Anderson, D. G. *Nat. Rev.*

- Drug Discovery*. **2009**, 8, 129.
13. Niikura, K.; Kobayashi, K.; Takeuchi, C.; Fujitani, N.; Takahara, S.; Ninomiya, T.; Hagiwara, K.; Mitomo, H.; Ito, Y.; Osada, Y.; Ijio, K. *ACS Appl. Mater. Interfaces*. **2014**, 6, 22146.
 14. Zheng, D.; Giljohann, D. A.; Chen, D. L.; Massich, M. D.; Wang, X. Q.; Jordanov, H.; Mirkin, C. A.; Paller, A. S. *Proc. Natl. Acad. Sci. USA*. **2012**, 109, 11975.
 15. Lee, J. H.; Lee, K.; Moon, S. H.; Lee, Y.; Park, T. G.; Cheon, J. *Angew. Chem. Int. Ed*. **2009**, 48, 4174.
 16. Derfus, A. M.; Chen, A. A.; Min, D. H.; Ruoslahti, E.; Bhatia, S. N. *Bioconjugate Chem*. **2007**, 18, 1391.
 17. Lee, H.; Kim, I. K.; Park, T. G. *Bioconjugate Chem*. **2010**, 21, 289.
 18. Na, H. K.; Kim, M. H.; Park, K.; Ryoo, S. R.; Lee, K. E.; Jeon, H.; Ryoo, R.; Hyeon, C.; Min, D. H. *Small* **2012**, 8, 1752.
 19. Urban–Klein, B.; Werth, S.; Abuharbeid, S.; Czubayko, F.; Aigner, A. *Gene Ther*. **2005**, 12, 461.
 20. Yano, J.; Hirabayashi, K.; Nakagawa, S.; Yamaguchi, T.; Nogawa, M.; Kashimori, I.; Naito, H.; Kitagawa, H.; Ishiyama, K.; Ohgi, T.; Irimura, T. *Clin. Cancer Res*. **2004**, 10, 7721.
 21. Sun, C. Y.; Shen, S.; Xu, C. F.; Li, H. J.; Liu, Y.; Cao, Z. T.; Yang, X. Z.; Xia, J. X.; Wang, J. *J. Am. Soc. Chem*. **2015**, 137, 15217.
 22. Ngamcherdtrakul, W.; Morry, J.; Gu, S.; Castro, D. J.;

- Goodyear, S. M.; Sangvanich, T.; Reda, M. M.; Lee, R.; Mihelic, S. A.; Beckman, B. L.; Hu, Z.; Gray, J. W.; Yantasee, W. *Adv. Funct. Mater.* **2015**, 25, 2646.
23. Lv, H.; Zhang, S.; Wang, B.; Cui, S.; Yan, J. *J. Control. Release* **2006**, 114, 100.
24. Yang, S. T.; Cao, L.; Luo, P. G.; Lu, F.; Wang, X.; Wang, H.; Mezziani, M. J.; Liu, Y.; Qi, G.; Sun, Y. P. *J. Am. Chem. Soc.* **2009**, 131, 11308
25. Baker, S. N.; Baker, G. A. *Angew. Chem. Int. Ed.* **2010**, 49, 6726.
26. Liu, C.; Zhang, P.; Tian, F.; Li, W.; Li, F.; Liu, W.; Zhang, T.; Liu, X.; Fan, Y.; Guo, X.; Zhou, L.; Lv, Y.; Lin, J. *J. Mater. Chem.* **2011**, 35, 13163.
27. Li, H.; Kang, Z.; Liu, Y.; Lee, S. T. *J. Mater. Chem.* **2012**, 22, 24230.
28. Zhai, X. Y.; Zhang, P.; Liu, C. J.; Bai, T.; Li, W.C.; Dai, L.M.; Liu, W.G. *Chem. Commun.* **2012**, 48, 7955.
29. Miao, P.; Han, K.; Tang, Y.; Wang, B.; Lin, T.; Cheng, W. *Nanoscale* **2015**, 7, 1586.
30. Zheng, X. T.; Ananthanarayanan, A.; Luo, K. Q.; Chen, P. *Small* **2015**, 11, 1620.
31. Zhang, T.; Liu, X.; Fan, Y.; Guo, X.; Zhou, L.; Lv, Y.; Lin, J. *Nanoscale* **2016**, 8, 15281.
32. Tang, J.; Kong, B.; Wu, H.; Xu, M.; Wang, Y.; Wang, Y.; Zhao, D.; Zheng, G. *Adv. Mater.* **2013**, 25, 6569.
33. Liu, C.; Zhang, P.; Zhai, X.; Tian, F.; Li, W.; Yang, J. *Biomaterials* **2012**, 33, 3604.

34. Hu, L.; Sun, Y.; Li, S.; Wang, X.; Hu, K.; Wang, L.; Liang, X.; Wu, Y. *Carbon* **2014**, 67, 508.
35. Cao, L.; Wang, X.; Meziani, M. J.; Lu, F.; Wang, H.; Luo, P. G.; Lin, Y.; Harruff, B. A.; Veca, L. M.; Murray, D.; Xie, S. Y.; Sun, Y. P. *J. Am. Chem. Soc.* **2007**, 129, 11318.
36. Zhu, S.; Meng, Q.; Wang, L.; Zhang, J.; Song, Y.; Jin, H.; Zhang, K.; Sun, H.; Wang, H.; Yang, B. *Angew. Chem. Int. Ed.* **2013**, 52, 3953.
37. Zhu, A.; Qu, Q.; Shao, X.; Kong, B.; Tian, Y. *Angew. Chem. Int. Ed.* **2012**, 51, 7185.
38. Huang, P.; Lin, J.; Wang, X.; Wang, Z.; Zhang, C.; He, M. *Adv. Mater.* **2012**, 24, 5104.
39. Hola, K.; Zhang, Y.; Wang, Y.; Giannelis, E. P.; Zboril, R.; Rogach, A. L. *Nanotoday* **2014**, 9, 590.
40. Chen, D.; Dougherty, C. A.; Zhu, K.; Hong, H. *J. Control. Release* **2015**, 210, 230.
41. Dong, Y.; Wang, R.; Li, H.; Shao, J.; Chi, Y.; Lin, X.; Chen, G. *Carbon* **2012**, 50, 2810.
42. Yu, P.; Wen, X.; Toh, Y.; Tang, J. *J. Phys. Chem. C* **2012**, 116, 25552.
43. Mei, Q.; Zhang, K.; Guan, G.; Liu, B.; Wang, S.; Zhang, Z. *Chem. Commun.* **2010**, 46, 7319.
44. Kim, H.; Kim, W. J. *Small* **2014**, 10, 117.
45. Dong, Y.; Pang, H.; Yang, H. B.; Guo, C.; Shao, J.; Chi, Y.; Li, C. M.; Yu, T. *Angew. Chem. Int. Ed.* **2013**, 52, 7800.
46. Singha, K.; Namgung, R.; Kim, W. J. *Nucleic Acid Ther.* **2011**, 21, 133.

47. Bieber, T.; Elsässer, H. P. *Biotechniques* **2001**, 30, 74.
48. Gosselin, M. A.; Guo, W.; Lee, R. J. *Bioconjugate Chem.* **2001**, 12, 989.
49. Hu, C.; Peng, Q.; Chen, F.; Zhong, Z.; Zhuo, R. *Bioconjugate Chem.* **2010**, 21, 836.
50. Nunes, A.; Amsharov, N.; Guo, C.; Van den Bossche, J.; Santhosh, P.; Karachalios, T. K.; Nitodas, S. F.; Burghard, M.; Kostarelos, K.; Al-Jamal, K. T. *Small* **2010**, 6, 2281.
51. Boussif, O.; Lezoualc'h, F.; Zanta, M. A.; Mergny, M. D.; Scherman, D.; Demeneix, B.; Behr, J. P. *Proc. Natl. Acad. Sci. USA.* **1995**, 92, 7297.
52. Fischer, D.; Bieber, T.; Li, Y.; Elsässer, H. P.; Kissel, T. *Pharm. Res.* **1999**, 16, 1273.
53. Sharma, V. K.; Thomas, M.; Klibanov, A. M. *Biotechnol. Bioeng.* **2005**, 90, 614.
54. Wang, X.; Zhou, L.; Ma, Y.; Gu, H. *Nano Res.* **2009**, 2, 365.
55. Chen, H. H.; Ho, Y. P.; Jiang, X.; Mao, H. Q.; Wang, T. H.; Leong, K. W. *Mol. Ther.* **2008**, 16, 324.
56. Ferrara, N. *Breast Cancer Res. Treat.* **1995**, 36, 127.
57. Takei, Y.; Kadomatsu, K.; Yuzawa, Y.; Matsuo, S.; Muramatsu, T. *Cancer Res.* **2004**, 64, 3365.
58. Alexopoulou, L.; Holt, A. C.; Medzhitov, R.; Flavell, R. A. *Nature* **2001**, 413, 732.
59. Matsumoto, M.; Seya, T. *Adv. Drug. Deliv. Rev.* **2008**, 60, 805.
60. Ryoo, S. R.; Jang, H.; Kim, K. S.; Lee, B.; Kim, K. B.; Kim, Y. K.; Yeo, W. S.; Lee, Y.; Kim, D. E.; Min, D. H.

Biomaterials **2012**, 33, 2754.

61. Lammers, T.; Peschke, P.; Kühnlein, R.; Subr, V.; Ulbrich, K.; Huber, P.; Hennink, W.; Storm, G. *Neoplasia* **2006**, 8, 788.
62. Moon, H. K.; Lee, S. H.; Choi, H. C. *ACS Nano* **2009**, 3, 3707.
63. Almeida, J. P.; Chen, A. L.; Foster, A.; Drezek, R. *Nanomedicine (Lond)*. **2011**, 6, 815.
64. Petros, R. A.; DeSimone, J. M. *Nat. Rev. Drug Discov.* **2010**, 9, 615.

Abstract in Korean (국문요약)

탄소나노물질을 활용한 바이러스성 질병 및 암 치료 시스템 개발

김성찬
자연과학대학 화학부
(생유기화학 전공)
서울대학교 대학원

많은 난치병들은 유전자 변형, 단백질의 기능장애, 바이러스 감염 등과 같은 분자수준의 원하지 않은 생명현상에서 기인한다. 나노메디신은 바이러스성 질병과 암을 분자수준에서 진단/치료하기 위해서 나노물질의 물리화학적 특성을 활용과 그 시스템적 접근방법을 연구한다.

본 연구에서는, 다양한 나노물질 중에서 특별한 물리화학적 특성을 가진 탄소나노물질에 관심을 갖고 바이러스성 질병과 암을 진단 및 치료 할 수 있는 시스템으로서의 그 잠재력을 연구하였다. 탄소나노물질은 구조에 기인한 매우 특별한 표면 성질과 sp^2/sp^3 혼성 탄소 구조에 따른 몇가지 특성을 지니며, 새로운 표면 개질 전략을 도입하여 생리활성물질과 간단하고 쉽게 상호작용을 갖도록 할 수 있다. 이러한 접근방법은 탄소나노물질과 생리활성물질사이에 물리적 또는 화학적 상호작용을 가능하게 하며, 이는 생물학적 환경에서의 탄소나노물질의 특성을 조절하고

또한 물질의 생체적합성을 개선시킨다. 본 연구에서는 탄소나노물질로서 산화그래핀과 탄소나노점의 두가지 물질을 활용하여 바이오이미징, 약물전달, 유전자전달, 광역동치료시스템을 통해 바이러스성 질병과 암을 진단 및 치료할 수 있는 시스템을 개발하였다.

먼저, 나노사이즈의 산화그래핀을 활용하여 표적하는 유전자를 감지하는 동시에 발현을 억제할 수 있는 DNAzyme 전달 시스템을 개발하였다. 특히 바이러스성 C형간염 발현에 영향을 주는 특정 표적유전자를 진단하고 동시에 mRNA 분자수준에서 절단하여 발현을 억제하는 것을 살아있는 세포에서 검증하였다.

두번째로, C형간염 모델 마우스에 대해 산화그래핀을 항암제/유전자 동시전달체로 활용하여 치료시스템으로서 시너지효과를 관찰하였다. 이러한 복합전달시스템을 통하여 항암제의 침투 효과 향상과 RNA 간섭효과를 동시에 이끌어내고, 결과적으로 기존의 $1/10$ 항암제 투여량으로 종양 성장을 성공적으로 억제하였다.

세번째로, 생체적합성이 높고 형광을 나타내며 엽산이 접합된 탄소나노점을 합성하고, 탄소나노점에 난용성 광감각제를 효과적으로 적재하여 정상세포가 아닌 암세포 특이적 바이오이미징 및 광역동치료시스템을 개발하였으며 마우스 종양동물모델에서 그 효과를 확인하였다.

마지막으로, siRNA를 효과적으로 담지하고, 오랫동안 분해로부터 보호하며 암세포에 효율적으로 전달할 수 있는 형광탄소나노점을 개발하였다. 빠르고 쉽고 간단한 방법을 통해 합성된 탄소나노점은 정전기적인력을 통해 siRNA를 효과적으로 적재하고, 마우스 종양동물모델에서 바이오이미징 및 RNAi 간접 효과를 성공적으로 이끌어 내었다.

이 시스템들은 이 후 탄소나노물질을 활용한 나노메디신 분야 기초연구에 중요한 자원이 되고, 장기적으로 나노기술을 활용한 중개연구로의 기술적 진보에 효과적인 기여할 수 있을 것으로 기대된다.

주요어: 탄소나노물질, 산화그래핀, 탄소나노점, 바이오이미징, 약물전달, 유전자전달, 광역동치료, 진단/치료시스템

학번: 2012-20267